Universidad de Antioquia
Instituto de Física
Facultad de Ciencias Exactas y Naturales

Gas Electron Multipliers muon detectors: a contribution to the detector characterization and GEM DAQ

Master's research work

Daniel Estrada Acevedo

Advisor: Ph.D. José Ruiz
Co-advisor: Ph.D. Johny Jaramillo

Medellín, 2023

Evaluators:

Ph.D. Carlos Ávila,
Universidad de los Andes, Bógota.

Ph.D. Fabian Castaño,
Universidad de Antioquia, Medellín.

Acknowledgements

I would like to express my heartfelt gratitude to my advisors, Ph.D. Johny Jaramillo and Ph.D. José Ruiz, for their guidance, support, and invaluable insights throughout the entire research process. Their expertise and encouragement have played a crucial role in shaping the direction and outcomes of this work.

I am also thankful to the GEM project group for their valuable input and constructive feedback during the development of my research internship. Their expertise and thoughtful suggestions have significantly contributed to every result, discussion, and overall quality of this research work.

I extend my appreciation to the University of Antioquia for providing the necessary resources and facilities that enabled the smooth execution of this project.

Furthermore, I am very grateful to my girlfriend, family, and friends for their unwavering support, understanding, and encouragement throughout this journey. Their belief in me has been a constant source of motivation.

Preface

During and after my bachelor's degree, I constantly questioned whether my decision to pursue a scientific career was the right one, especially considering the limited job prospects for physicists in my country. These doubts made it challenging for me to define my research path that truly captured my interest. Fortunately, there were individuals who appeared in my life during those moments, shedding light on new possibilities and offering me valuable opportunities. As a student, I strongly advise you to leverage the extensive experience of your professors. They have likely encountered similar dilemmas and can help guide you in finding your own path.

In my case, on two separate occasions, it was my professor who pulled me out of the depths of uncertainty and showed me that there is always something new to learn and explore. The first instance introduced me to the world of scientific instrumentation and electronics, a field that I, such a student from a traditional physics school, never thought such as possibility in my profession. From there, I discovered a newfound passion and curiosity for applied science, acquiring various computational and experimental skills along the way.

The second instance went even further, as my professor demonstrated that modern science is not just about an individual conducting experiments independently. Instead, I learned that the most powerful scientific advancements arise from the collective efforts of thousands of brilliant minds working together to pursue new knowledge. It is through this collaborative approach that numerous scientific, technological, and experimental methods are developed. This second occasion corresponded to the current stage of my life, those last two years of my Master's studies. It allowed me to transition from a comfortable position in the electronics laboratory to the chaotic world of the largest scientific collaboration of our time, CERN (European Organization for Nuclear Research).

For my Master's degree, I had the opportunity to undertake a research internship as part of a collaboration between the University of Antioquia and the CMS (Compact Muon Solenoid) experiment at CERN. This collaboration focuses on the GEM project, which aims to incorporate Gas Electron Multiplier (GEM) detectors into the CMS muon system.

Having limited knowledge in the field of particle physics, I initially encountered a significant challenge in grasping even the fundamental concepts, such as the nature of muons, the standard model, and particle accelerators. Overcoming this obstacle re-

quired an extensive process of reading and researching numerous references, authors, and materials to meet the requirements of the project. It felt like an imposing barrier to overcome, especially because I had never been interested in this physics field. This experience motivated me to write this manuscript.

My main objective with this research work, besides fulfilling the commitments of tasks and developments that were established progressively in the CMS-University of Antioquia agreement, was to create a resource that facilitates students' first contact with the GEM project. The aim was to make this document as self-contained as possible, covering from general topics to more specific ones. This initiative wants to simplify and streamline the onboarding of students into GEM projects. This way, students can contextualize themselves more quickly and efficiently, which will allow them to dedicate more time to the more significant and enriching challenges of the collaboration.

To achieve this, the manuscript is structured into four chapters. The first one provides a general introduction to experimental particle physics, including its history, with a specific focus on the CMS experiment as one of the general-purpose experiments at CERN's LHC (Large Hadron Collider). The second chapter delves into the physics behind gaseous detectors and how this technology is utilized to study ionizing particles such as muons. It presents the structure of the GEM detector to provide a comprehensive overview of the involved interaction processes. Moving on to the third part, the text explores the organization of the data acquisition system of GEM and how it is coupled with CMS, trying to provide insight into the complexities associated with implementing such a large-scale detection apparatus. The final section of the manuscript concludes by explaining the assembly and testing processes specific to the GEM detector, equipping readers with important foundations in quality control tasks to join the collaboration easily.

Throughout the text, for sure, my aim is also to highlight my contributions, as I have been involved in various tasks supporting the collaboration. Primarily, I have made significant contributions to software development, such as implementing the S-curves scan analysis routing for the GEM data analysis suite. Additionally, since I had the opportunity to participate directly in the assembly and tune-up processes to ensure that the GEM detector meets the highest performance standards, I will mention, for example, the contributions made to optimize the sixth quality control stage.

With nothing more to add, I hope that this book fulfills its intention, and you can consider it as a primary reference when embarking on your work in the GEM project.

Contents

Chapter 1

Overview on experimental particle physics, LHC, and CMS

Many of the scientific researches today are focused on the development of experiments that allow pushing to the limit modern theories such as the Standard Model. But, if your objective is to delve into the particle physics field, it will be necessary to have a brief trip through its history and conceptual fundamentals. That way, you will be able to have a better understanding of today's experiments and it should allow you to play a more purposeful role in their development.

This first chapter of the report provides a historical review of the most important events in the study of the building blocks of matter and their interactions. It also covers the general conception of particle collisions and detections and gives a more detailed overview of the CMS experiment. One of the general-purpose experiments installed in the Large Hadron Collider - LHC of CERN the main organization that coordinates today's most important high-energy experiments.

1.1 Historical overview

It is customary to trace the conception of the composition of particulate matter back to the era of the ancient Greeks and attribute it to Democritus and the atomists. However, in this context, we will consider that the corpuscular compositions of matter were not proven until the end of the 19th century and the beginning of the 20th century through experiments conducted by J.J. Thomson and Rutherford. The discovery of the electron is attributed to the former through his experiment with cathode rays in 1897. The latter is responsible for demonstrating, through experiments on the scattering of alpha particles in 1911, that the nucleus of the atom, which he named the proton, is concentrated at the center. [1]

Niels Bohr, taking the electron and the proton ideas, proposed a successful (to some extent) atomic model able to describe the Hydrogen spectrum, but not to explain the origin of the big weights of heavier atoms like Helium. It was thanks to Chadwick's discovery of the missing component (Neutron - 1932) what could be completed that we know such as ***classical era of particle physics***. [2]

It's important to mention that those events took place at the same time that important discoveries[a] about the quantized nature of the light and, thus, the quantization of the electromagnetic interaction. That is a fundamental fact in the area of the quantum field theory, and it established that the photon (the electromagnetic quantum) is the mediator particle in any electromagnetic interaction. [1, 2]

With the classical model, physicists finally could offer a simple and satisfactory answer to the fundamental question "What is matter made off?". But a few years were enough to notice some inconsistencies that needed missing components to maintain the coherence of the model. This made the way for the age comprised between 1930 and 1960, also knew such as the ***middle period of the particle physics***. [2, 1]

Since the 30's, several proposals and discoveries set the basis of the modern conception of particle physics. In 1928 Dirac, through his developments in relativistic quantum mechanics, introduced the need for the existence of a positron (e^+), which means antimatter, and even more the need for a matter/antimatter symmetry. In 1930, studies about nuclear beta decay led to the proposal of a new light and electrically neutral particle, called by Pauli as neutron and renamed by Fermi as Neutrino (ν), able to explain the missing energy in the observations of the decays. The notion of weak force was also introduced by Fermi in 1933. In 1935 Yukawa, in a try to answer the simple question "What holds the nucleus together?" introduced the notion of the strong force and thus, the quantum, which analogously to the photon, mediate this nuclear interaction. The needed characteristics of Yukawa's particle seeded the possibility of the existence of a Meson (middle-weight particles whose mass lies between the electron and the proton masses[b]). [2, 3]

Those years were also prosperous in the sense of experimental evidence to support the proposed theories. 1932 brought the positron's discovery thanks to Carl Anderson's experiments of tracks produced by cosmic rays in a *cloud chamber*, which helped to support Dirac's positrons. Since 1937, evidence of the existence of particles that matched Yukawa's predictions was found by analyzing *cosmic radiation*. Nevertheless, it was not until 1947 when C. Powell and his co-workers at Bristol (England) started more detailed studies which concluded that founded particles were not actually Yukawa's mesons, but they were two new middle-weight particles called by themselves such as Pion(π) and Muon(μ). Indeed, they also contributed to Pauli's neutrinos proposal when they studied the decay of those mesons through *bubble chambers* and conclude that $\pi \to \mu + \nu$ and $\mu \to e + 2\nu$. Even more, Powell's research suggested the existence of at least three types of neutrinos. Also, in the same year, Rochester and Butler proved that pion could be himself a product of decay from a Kaon (K^+), a new heavy meson. [1, 3]

[a] Between 1900 and 1924 scientists such as Plank, Einstein, and Compton develop experiments and explanations that show the light behaviors as a particle.

[b] In the same spirit the electron was called Lepton ("light-weight") and the proton and neutron were called Baryons ("heavy-weight")

Thanks to the study of beta-decay processes, the mentioned Powell's results, and others, by 1950, there was compelling theoretical evidence for the existence of neutrinos. But, there was still no direct experimental verification due to neutrinos interacting extraordinarily weakly with matter, and to have a chance of detecting one it was necessary an extremely intense source. So, that is why it was not until mid-fifties when C. Cowan and F. Reines used the Savannah River nuclear reactor in South Carolina, to see the first neutrinos in *nuclear reactors detectors* based on big water thanks. [1]

Over the next years, the meson family was extended with new particles that were called collectively "Stranges". Even, a family of Baryons (heavyweight particles) was established including the proton such as the lightest and other heavy baryons which appeared as a result of incoming conservation rules (like the conservation of the baryon number in a decay). Those strange particles just could be observed after the construction of one of the first modern *particle accelerators*, the Brookhaven Cosmotron, in 1953. [3]

The label strange was not just because it dealt with not seen before particles, it was also because the mechanism of disintegration appeared to involve weak interactions while its production entails strong ones. The puzzle of those strange particles began to be resolved thanks to the A. Pais and M. Gell-Mann's ideas, which resulted in the introduction of the strangeness quantum number. [1]

You can notice at this moment that the original set of particles that seemed so tiny in 1947, begin to increase until in 1960 it became a bigger one that include all types of new proposed particles, many of them, not observed in a laboratory yet. That phenomenon resulted in the basic task of classification of the particle zoo, which started to be implemented around 1961 principally by Gell-Mann in his "Eightfold way". It simply consisted of arranging the baryons and mesons into geometrical arrays according to their charge and strangeness (see Figure 1.1). The Eightfold way allowed Gell-Mann to study in a systematic way known particles and their decays, even, he could predict the existence of one (Ω^-) with charge -1 and strangeness -3. And when this last one was discovered, no one doubted that Gell-Mann's theory was correct. The real importance of Eightfold's way was that it provided an organizational structure to the particle theory in development, and we can consider here that this was the fact that initiated the ***modern era of particle physics.*** [1, 2]

In January 1964, two papers were published individually by Gell-Man and the other by G. Zweig. There, the existence of more fundamental components of the particles was proposed. They were called by Gell-Man quarks, and could be found in three "flavors": u (for "up"), d (for "down"), s (for "strange"), and their respective "anti-flavors". [3]

The quark model was inspired by the question "Why do the hadrons fit into these specific patterns?" (Eightfold's way patterns) and Gell-Mann noticed that his proposed quarks could reconstruct all the particles according to the following asserts:

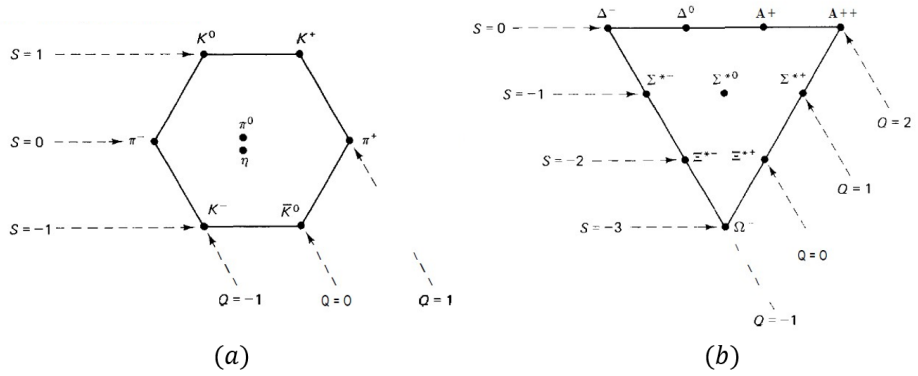

Figure 1.1: (a) The Meson Octet: The eight lightest mesons fill a hexagonal pattern where the diagonal lines determine the charge, and horizontals determine strangeness; (b) The Baryon Decuplet: At that time the only particle that was not known experimentally was the Ω^-. Diagrams taken from [1].

THE BARYON DECUPLET

	Q	S	Baryon
uuu	2	0	$\mathbf{\Delta^{++}}$
uud	1	0	$\mathbf{\Delta^{+}}$
udd	0	0	$\mathbf{\Delta^{0}}$
ddd	-1	0	$\mathbf{\Delta^{-}}$
uus	1	-1	$Z^{\star}+$
uds	0	-1	$\mathbf{\Sigma^{*0}}$
dds	-1	-1	$\mathbf{\Sigma^{*-}}$
uss	0	-2	$\mathbf{\Xi^{*0}}$
dss	-1	-2	$\mathbf{\Xi^{*-}}$
sss	-1	-3	R_{-}

THE MESON NONET

	Q	S	Meson
$u\bar{u}$	0	0	$\pi^{\mathbf{0}}$
$u\bar{d}$	1	0	$\eta_{\mathbf{r}}+$
$d\bar{u}$	-1	0	π^{-}
$d\bar{d}$	0	0	η
$u\bar{s}$	1	1	K^{+}
$d\bar{s}$	0	1	K^{0}
$s\bar{u}$	-1	-1	K^{-}
$s\bar{d}$	1	1	$\overline{K}^{0}$
$s\bar{s}$	0	0	$\eta\prime$

Table 1.1: Table that illustrates the rules of particle reconstruction from proposed Gell-Mann's quarks. Taken from [1]

.

Three quarks form a baryon (and every antibaryon is composed of three antiquarks); One quark and an antiquark form a meson. Therefore, we can tabulate all the combinations to get every particle (See Table 1.1).

Note that the quark model itself predicted the existence of another meson, fortunately, the last was discovered experimentally ($\eta\prime$). But, on the other hand, unfortunately, no quarks had been found, even though they had nonzero charge and should have been easily identified with a simple Millikan oil drop experiment. That occasioned significant skepticism about the quark model. [1]

In the late sixties (and in the early seventies) a light appeared over the model when "deep inelastic scattering" experiments were developed using *high-energy accelerators* to replicate the Rutherford experiment's idea. To their dismay, even though the ex-

perimental results had the expected behavior, they were not completely conclusive. Furthermore, theoretical objections started to appear when physicists noticed that the quark model did not satisfy the Pauli exclusion principle. Luckily another brilliant scientist, O. W. Greenberg, in 1964 proposed a way out of the previous dilemma, introducing the color hypothesis. He suggested that quarks not only come in three flavors but each of these also comes in three colors ("red," "green," and "blue"), so, taking one quark of each color to make a baryon, any discrepancy with the Pauli exclusion principle is avoided. [3]

Ten fruitless years passed after Greenberg´s proposal, and the rescue of the quark model (and its color hypothesis) finally came. In 1974 an event known as the November revolution took place, it was basically the discovery of the psi meson (ψ), one important particle that revealed new physic and also triggered ten prosperous years where the existence of three extra quarks (c for "charm", b for "bottom" or "beauty", and t for "top" or "truth"), and two leptons (τ and its respective neutrino ν_τ) was proven. Every one of the discoveries before could be explained with the quark model, and they confirmed the Glashow, Iliopoulos, and Miaini's prediction about the not logic asymmetry in the number of leptons and quarks. And with this, there have been no doubts about quark's existence. [1, 2]

From now the constituents of matter were revealed, but, what about interactions? As you could recall from previous paragraphs, the first approximations about strong and weak forces were made by Yukawa and Fermi respectively, indeed, the last one modeled a weak interaction as a contact force because of its extremely short range of action. However, this conclusion last failed at high energies and physicists decided to continue with a theory in which the interaction was mediated by the exchange of particles, which started to be called intermediate vector bosons. The challenge was then, besides the experimental demonstration, to predict the properties of these vectors. Some estimations were published during the 50's, but it was not until the emergence of the electroweak theory of Glashow, Weinberg, and Salam that a really firm prediction of the vector bosons mass was possible. They proposed the existence of three intermediate vector bosons for the weak force, two of them charged (W) and one neutral (Z). They were discovered experimentally in *proton-antiproton collisions* at CERN in 1983. On the other side, Yukawa's meson (π) clearly could not be the strong force mediator, but in its place, the notion of gluons was adopted. Gluons themselves carry out color and should not exist as isolated particles, just like the quarks. [1]

At that point, considering the three kinds of elementary particles (leptons, quarks, and mediators), the different postulated antiparticles, and all their hypercharge variations, the number of "elementary" particles reached the large number of 61 particles, including here, that the Glashow-Weinberg-Salam theory calls the Higgs particle, which was introduced in the mid-sixties to explain the origin of the particle's masses. This aims to conclude just one thing; A simple three-particle model of the universe was not enough to explain the experimental evidence and theoretical holes. So, physicists, through several discoveries, theories, and important experimental advances, were able

to make, in a little more than a half-century, a better model of the world, which describes all matter through three kinds of particles (leptons, quarks, and bosons) in that we know today as *Standard model of particle Physics* (SM). [1]

This theory is still in development and continues to yield new discoveries, such as the most recent one, the confirmation of the mentioned Higgs boson in 2012 by CERN, which was achieved through experiments conducted at the Large Hadron Collider (LHC) the biggest particle accelerator built until now.

Due to its importance to understand the current particle zoo, let us expose a few details of the SM in a short section, just before continuing with the main concern of the present research work: the detection issues.

The Standard Model

Today we can not say yet that the standard model is the definite theory that describes nature, but for now, it is the theory able to describe the majority of known phenomena. The particles of the SM can be condensed in a simple and well-known diagram (See Figure 1.2) which divides them into two big categories, Fermions, and Bosons. The formers are constituted by the already seen leptons and quarks which fall naturally into three generations or families according to their characteristics such as mass and charge. [4]

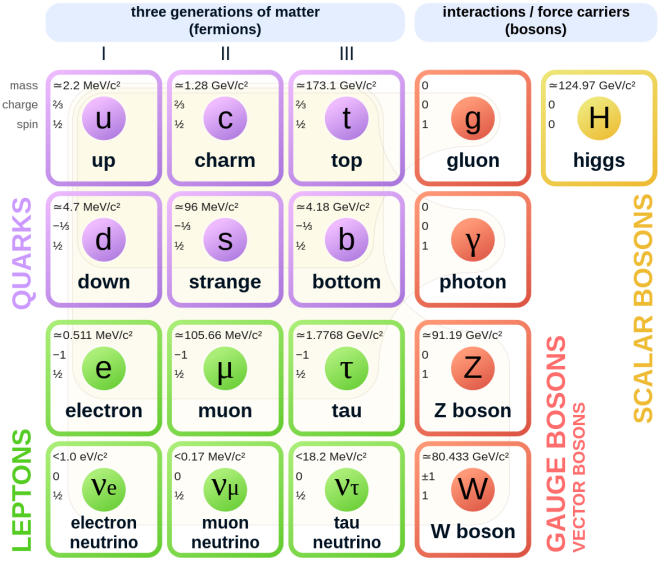

Figure 1.2: Particle content of the standard model, taken from [5].

But SM is not just a form to classify particles, it also contains the mathematical tools to study their dynamics and properties. The SM relies on two of the more elegant constructs of modern physics and mathematics, quantum field theory and group theory [4]. Being very general and not very precise, these fields work together to describe nature as a result of particle interactions governed by symmetry properties

that obey quantum mechanics and relativistic constraints.

The SM is certainly one of the most successful theories in the history of physics. With only 19 free parameters it is able to make thousands of predictions that have been measured and tested over the last seventy to eighty years. However, some aspects of the model are not completely understood and some others are not possible to explain [4]. Therefore, current particle physics focuses its effort on trying to propose BSM (Beyon Standard models) theories to include recently discovered phenomena related to, for example, neutrino masses. This report will not focus on the theoretical details, for the interested reader, a modern formulation of this model is presented in [1]. This short section was just to establish the context of what we will discuss in the next chapters. So, let us start with more practical discussions about detector and detection processes.

1.2 Experimental particle physics

The modern study of particle physics can be divided into three main fields: theoretical, experimental, and analytical. While this has been implicitly evident in historical accounts, it is important to note that particle physics research follows a workflow that traverses all three fields. The theoretical field is responsible for constructing models that make physical predictions. The experimental field establishes the necessary designs and concepts to build experimental setups that enable the production of meaningful data. The final step is the analytical field, where the observed physics is compared to predictions to verify its validity. [6]

The experimental field can naturally be associated with detector physics since its ultimate goal is particle detection. This research work is framed in this field, and therefore, the following efforts will be dedicated to answering fundamental questions, such as how particles are produced and detected and how these apparatuses are designed and built.

1.2.1 How particles are detected?

The previous sections did not delve into the evolution of experimental setups in particle physics, although some interesting related words were marked in italics to indicate the main apparatus or experiments used. Here I will try to explain to you in a general way how physicists began to see what could not be seen.

The first known detector that allowed physicists to see tracks of subatomic particles was the *cloud chamber* which was invented in 1911 and awarded to Thomson Rees Wilson the novel prime in 1927. This detector was the one that allowed the discovery of positrons, muons, and strange particles in the 50's [1, 2, 3]. It works by creating a supersaturated vapor of a liquid that condenses into visible droplets in the presence of ionizing radiation. So, the path of the particles can be tracked by observing the droplets they produce in the chamber.

In the same years, D. A. Glaser invented the *bubble chamber*, a detector with a similar working principle of the former. It uses a superheated liquid that is maintained at a temperature just below its boiling point. When a charged particle passes through the liquid, it ionizes the atoms and molecules along its path, causing the temperature in the ionization track to increase slightly which creates a region of lower pressure, where small gas bubbles can form around the ionization track. These bubbles can be photographed, to study the properties and behavior of the crossing particles. This type of detector allowed the confirmation of the electro-weak theory around 1973. One of the most important bubble chamber was built at CERN and it was called GARGAMELLE. [7]

Other types of detectors like Geiger counters, Cherenkov counters, Spark chambers, Photographic emulsions, scintillators and photomultipliers (just to mention some of them) started to be implemented in the middle of the 20th century. Nowadays, modern detectors consist mainly of arrays of several of these detectors, each one of them optimized to measure specific properties of particles [7]. The important thing to notice here is the main fact that allows them to see the track of a particle.

By examining the various types of detectors, one can understand that the crucial process taking place inside them is the interaction between high-energy charged particles and the medium. In the case of cloud and bubble chambers, charged particles pass through and ionize the atoms of the fluid, leaving a trace of their trajectory. Once the path of a particle is visible, it's a matter of analyzing the characteristics of the path to determine which particle it corresponds to. Typically, to distinguish it, a magnetic field is applied to curve charged particle tracks according to the cyclotron formula (1.1):

$$R = \frac{pc}{qB}, \tag{1.1}$$

where c is the speed of light, p is the momentum of a particle with electric charge q, B is the magnetic field and R is the radios of the particle path.

But, what about not charged particles? they do not cause ionization and they do not leave tracks. The way to study this kind of particle is through their decay products, in this way, invoking conservation of energy and momentum, the path of the original particle can be reconstructed. Some real path pictures are shown in Figure 1.3. The same applies to those particles with a very short lifetime [7]. In cases such as neutrino detection, where the particles are not charged and do not decay into other particles, the detection process must involve irradiative interactions, such as Cherenkov radiation.

The previous description was just the main idea behind the tracking processes. However, currently, the way of reconstructing the path is not visual, today no real pictures (with a camera) of chambers are taken to see the trajectories. In its place, very granular arrays of detectors are sorted to take computational data about the track of the particles, and just until the end of data acquisition, the computational

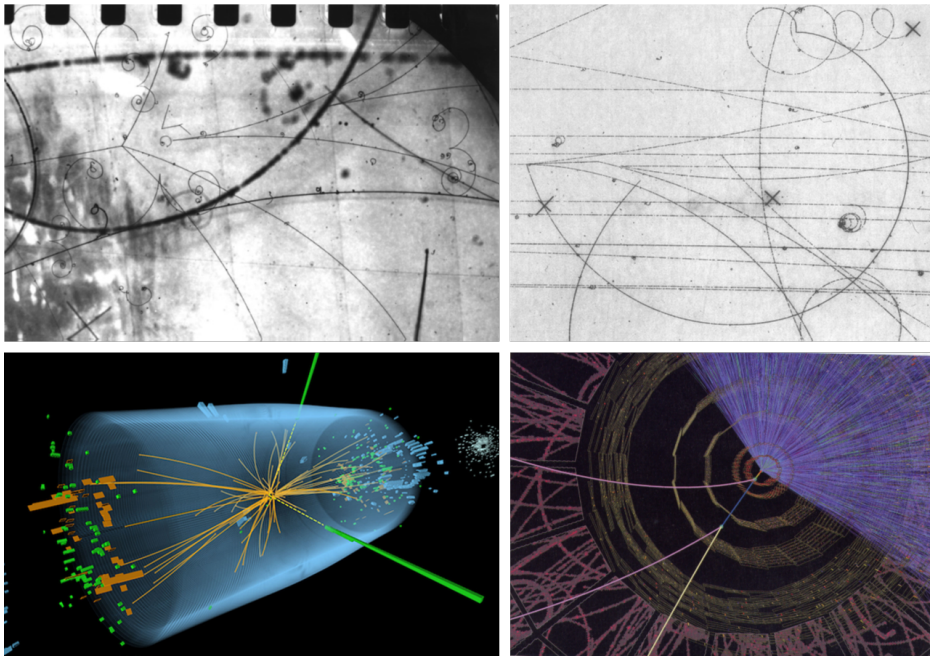

Figure 1.3: Real pictures of particle's tracks, taken from [7, 8].

analysis could show what was the real track by graphical representations of data (See Figure 1.3).

1.2.2 Where do the particles for analysis come from?

The answer to this question depends on the type of particle that is wanted to analyze. Electrons and protons are relatively easy to obtain. The former can be generated simply by heating up a piece of metal, while the latter can be obtained by ionizing the simplest atom, hydrogen. However, for more exotic particles alternative sources are necessary. The key requirement is to produce a physical process with an energy equivalent to the mass of the particle of interest[c], as determined by the famous equation $E = mc^2$. It is possible to mention here three main processes.

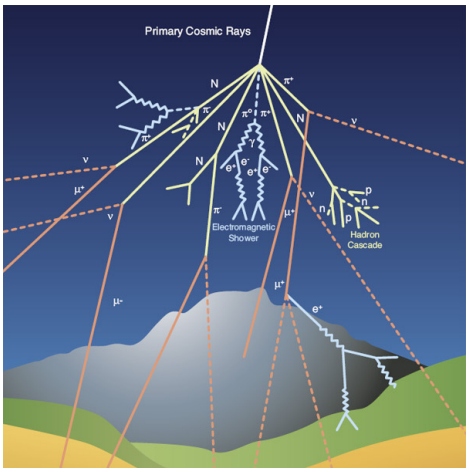

Figure 1.4: Illustrative representation of cosmic ray particle showers. taken from [9].

[c]Actually, we do not know the masses of the particles we are searching for, and we are unsure if they even exist. Thus, the objective is to create processes with energies within a desired range to increase the likelihood of discovering these particles.

The first source of particles is found in nature, the nuclear reactions. Radioactive nuclei can emit a variety of particles such as alpha and beta particles, neutrons, neutrinos, photons, and positrons when they undergo disintegration. However, the energy spectrum produced by this source is limited and typically does not exceed tens of MeV, which is not enough to observe exotic particles.

The second source and one of the mots commonly used from the beginning is cosmic rays. Continuously, the Earth is bombarded with high-energy particles coming from outer space. Those primary particles collide with the upper atmosphere and produce the effect of a shower that falls over us. Many of the secondary particles are pions (See Figure 1.4). Cosmic rays have two virtues, they are free and have huge energy. But they also have two major disadvantages, the rate at which they strike any detector of reasonable size is very low, and their production is completely uncontrollable.

Finally, aiming to produce enough energetic processes in a controlled way, physicists started to study the way to use particle accelerators such as a source of other particles. The main idea here is to take common and preferably stable particles (like protons, electrons, or positrons) and accelerate them to high energy, then smash them against a target which could be anything from a simple plate (to collide their atoms) to other individual particles as protons (to get more fundamental products). It is also possible to collide two accelerated particles, in this way a double energetic process can be achieved. The latter mechanism is the main used in current particle physics experiments which involve an accelerator.

The principle of the acceleration process is simple, but its implementation presents challenges from an engineering standpoint. Acceleration is achieved through the application of electric fields, but there is a spatial limitation to this approach. To overcome this, the first linear accelerators (LINACs) were optimized by using resonant cavities. However, they eventually reached their limitations and motivated the evolution into circular geometrical accelerators, which are more familiar and widely used today to produce increasingly energetic processes. This successive progress in accelerator technology has enabled the study of the most fundamental and rare particles and processes.

1.3 Main particle physics research centers

Various developments in particle physics were reached thanks to big laboratories that were being established along the second half of the 20th century, some of them are:

- The BNL from Brookhaven National Laboratory. Located in Upton (United States), it was established in 1947 and was the home of the first synchrotron, known as the Cosmotron. It made significant advancements by imparting kinetic energy in the GeV range to a single particle, specifically by accelerating protons to 3.3 GeV. Notably, the Cosmotron was the inaugural accelerator to enable

the extraction of particle beams for experiments located physically outside the accelerator. Furthermore, it held the distinction of being the first accelerator capable of producing all known positive and negative mesons found in cosmic rays. [10]

- CERN, initially named "Conseil Européen pour la Recherche Nucléaire," was established in 1954 by 12 European countries. It has been the site of crucial experiments, including the Gargamelle bubble chamber, the Super Proton Synchrotron, and the Large Electron–Positron Collider. Presently known as the Organisation Européenne pour la Recherche Nucléaire, CERN is located in Switzerland, near Geneva, along the French-Swiss border. It hosts the Large Hadron Collider (LHC), recognized as the world's largest and highest-energy particle collider to date. Several important achievements in particle physics have been made through experiments at CERN, principally by This includes the acceleration of heavy ions to around 1.4 TeV and protons to around 7 TeV. [11]

- The Stanford Linear Accelerator Center (SLAC), was established in 1962 and is currently known as the National Accelerator Laboratory. It is located on the campus of Stanford University in the United States. Using its linear accelerator, SLAC successfully accelerated electrons to energies of 50 GeV. Thanks to its experiments it was possible to confirm the existence of the quark. [12]

- Fermilab, officially known as the Fermi National Accelerator Laboratory, is located in Batavia, Illinois, United States, and was established in 1967. It hosted the well-known Tevatron, a synchrotron that accelerated protons and antiprotons in a 6.28 km ring to energies of up to 1 TeV, making it the first accelerator to reach a "tera-electron-volt" energy. One of its most important achievements was the discovery of the top quark in 1995.

- TANDAR (1985), the USP Pelletron (1972), and LNLS (1997) are tandem accelerators and a synchrotron located in Buenos Aires (Argentina) and São Paulo, respectively. These facilities represent some of the few high-energy particle research centers available in Latin America. They have the capability to accelerate various types of ions close to the energy level of 1 TeV. In addition to their contribution to advanced studies in high-energy physics, they also function as astroparticle observatories, like many other particle research facilities in Latin America. [13]

Currently, CERN is the leading laboratory in the world for particle physics research, with the most advanced accelerator complex and the LHC as its flagship facility. While other particle accelerators exist globally, such as the SuperKEKB in Japan, CERN's LHC provides unparalleled opportunities to explore the fundamental aspects of particle physics. This research work is framed in the Compact Muon Solenoid - CMS experiment, one of the four experiments at the LHC. From here on we will detail the most important aspects to contextualize the environment in which this work is carried out.

1.4 The Large Hadron Collider - LHC

The Large Hadron Collider is a machine located on the French-Swiss border near Geneva. It accelerates and collides protons and lead ions, and as we mentioned before, it is the largest particle collider in the world with a circumference of 27 km. This accelerator aims to study particle physics and the fundamental nature of the universe by achieving particle physics searches at the TeV scale. It was designed to be able, in the case of protons, to collide up to center-of-mass energy of $\sqrt{s} = 14$ TeV at an instantaneous luminosity $\mathcal{L} = 1 \times 10^{34}$ cm^{-2}s^{-1} [d]. In the case of heavy ions, with energy up to 6.8 TeV and a peak luminosity of 1×10^{31} cm^{-2}s^{-1}. [14]

To reach those energy values an acceleration process of multiple stages is needed (see Figure 1.5). The particles, whether protons or heavy ions, start from the source with an energy of 750 keV and undergo initial acceleration in a linear accelerator (Linac 2), where they reach an energy of 50 MeV and are organized into particle packages known as bunches, each having around 1.15×10^{11} particles. Subsequently, the particles are transferred to a circular accelerator (Proton Synchrotron Booster) and accelerated to 1.4 GeV. The next stage involves transferring the particles to the Proton Synchrotron (PS), where they reach an energy of 25 GeV. Finally, the particles are injected into the Super Proton Synchrotron (SPS), where they are accelerated to 450 GeV before being injected into the Large Hadron Collider (LHC), reaching center-of-mass energies of 7 TeV per beam. [14, 15]

To achieve those energy scales, besides the large dimensions characterizing the LHC, it is crucial the cutting-edge technologies that were developed during its construction. Accelerating charged particles to such scales poses physical challenges that continue to push the technological limits of recent decades. For instance, total control over the dynamics of the bunches involves deflecting and focusing particles traveling at nearly the speed of light. This necessitates various sets of magnetic dipoles and multi-pole magnets to correct the trajectory, the electromagnetic disturbances, and even the gravitational effects. The LHC employs 1232 magnetic dipoles made of Nb-Ti coils cooled to 1.9 K to maintain a superconducting state, enabling efficient operation and generating a field of 8.3 T (more than 300 000 times the Earth's magnetic field). Maintaining these cryogenic temperature scales requires sophisticated cooling systems using liquid helium at less than 5 K, it is transported through a cryogenic pipeline around the entire LHC. This, in turn, requires strict control over vacuum levels in the tubes, both to manage pressures for maintaining helium at low temperatures and superconductivity in the magnets and to ensure that the bunches circulate ideally in a vacuum to avoid collisions with gas molecules. To provide an idea, the vacuum pressure in the beam pipe is approximately 10^{-7} Pa, and lower than 10^{-9} Pa close to the interaction points. [16]

The LHC uses a system of RF cavities working at 400 MHz to accelerate the particles. Consequently, the number of bunches in the injected beam and its temporal distance cannot be arbitrary. An analysis of the accelerator's characteristics suggests

[d] 1×10^{34} collisions by centimeter square per second that can take place.

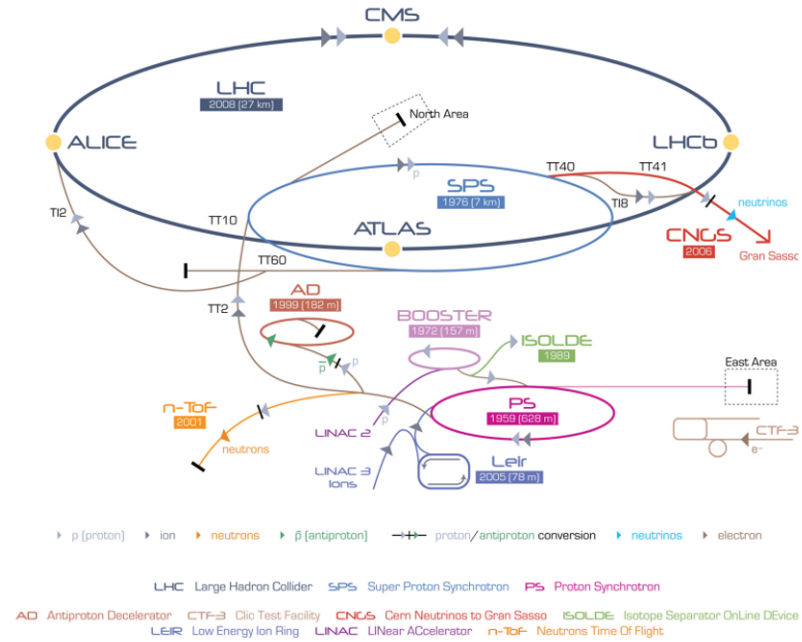

Figure 1.5: Schematic of the LHC main ring design. taken from. [4]

that the LHC could accelerate a beam containing up to 35 640 bunches. However, the currently used configuration is 2 808 bunches with a temporal spacing of 25 ns, This is equivalent to a frequency of 40 MHz, which is the repetition rate of the collisions in the interaction points, also known as "bunch crossing" (BX). This configuration aims to ensure a correct sequence of bunches injected into the ring and allows for the insertion of new bunches when non-useful ones are extracted. [14, 16]

On another note, the crucial parameter of luminosity, referring to the number of collisions per square centimeter per second that can take second that can take place, is achieved, for example, by maximizing the cross-section of the bunches. This involves focusing the beam to maximize the collision probabilities between the particles of the beam. Far from the collision point, the beams consist of cylinder-like bunches of 7.48 cm long with a section of approximately 1 mm^2. As they approach the collision points (the experiments), these bunches are focused to reach a section of approximately 16×16 μm^2. [16]

Despite these remarkable features, the LHC, operating at its nominal luminosity, can only generate events with a few collisions per BX, approximately 50. However, it's crucial to consider only inelastic collisions, as the cross-section from elastic scattering of protons and diffractive events will not be detected by the detectors, given that they do not produce particles at sufficiently high angles with respect to the beam axis. This leads to approximately 20 effective collisions, also known as the "Pile Up vertex" [16]. Therefore, it is evident that the progressive increase in these nominal parameters becomes crucial for the LHC to enhance the accelerator's discovery potential. Further details on this topic will be provided shortly.

The LHC has four main experiments ALICE, ATLAS, CMS, and LHCb, which are located at the interaction points (marked on Figure 1.5) where specific detectors are placed to analyze the products of collisions according to its experimental objectives. For example, the ALICE (A Large Ion Collider Experiment) focuses on studying the confinement of the quarks through the quark-gluon plasma produced in heavy ion collisions, a state of matter believed to have existed in the early universe. The ATLAS and CMS experiments are general-purpose experiments that aim to discover new particles (the Higgs Boson) and physical phenomena (beyond SM), as well as to measure the properties of known particles. The LHCb experiment focuses on particles containing the b-quark, such as B-mesons and lambda-b baryons, and aims to study the asymmetry between matter and antimatter in their decay processes. [15]

You can delve into the LHC experiment, along with additional details and approximate physical calculations common to all particle accelerators, available on [16].

1.4.1 LHC goals and upgrade schedule

The LHC has been undergoing periodic upgrades to reach and improve its nominal parameters and discovery potential. These upgrades are primarily aimed at increasing the center of mass energy and the luminosity of the machine, which will allow access to rare physics processes. This upgrade was planned to be performed progressively intercalating time periods of activity (RUNs), major Long Shutdowns (LS), and an Extended Year End Technical Stop (EYETS) until reaching the desired Hl-LHC (High luminosity LHC), which is planned to produce proton collision at 14 TeV with peak luminosities of 5×10^{34} $\text{cm}^{-2}\text{s}^{-1}$ and integrated luminosity of 3000 fb^{-1} (See Figure 1.6). [15, 17]

According to the original schedule for LHC commissioning, the first low-energy collisions at a center-of-mass energy of 900 GeV were expected to take place before the end of September 2008. The first inaugural beam was circulated through the collider on the morning of September 10, 2008. However, on September 19, an electrical fault vented about six tons of liquid helium into the tunnel, causing the collider to be non-operational until November 2009. Despite the delay, the LHC was officially inaugurated on October 21, 2008. The first operational run (RUN1) did not take place until November 20, 2009, when the desired energy levels were successfully achieved. [20]

During the 2010-2012 period, the LHC was able to increase its energy levels, reaching a combined energy level of around 8 TeV and an instantaneous luminosity of 6×10^{33} $\text{cm}^{-2}\text{s}^{-1}$ in proton-proton collisions, using a bunch spacing of 50 ns. The LHC was originally planned to start the first long shutdown (LS1) from the end of 2012 until around 2015 to allow upgrades to a planned beam energy of 7 TeV per beam and nominal luminosity. However, in late 2012, considering the discovery of the Higgs boson in July 2012, the shutdown was postponed for several weeks into early 2013 to allow additional data taking. [16, 20]

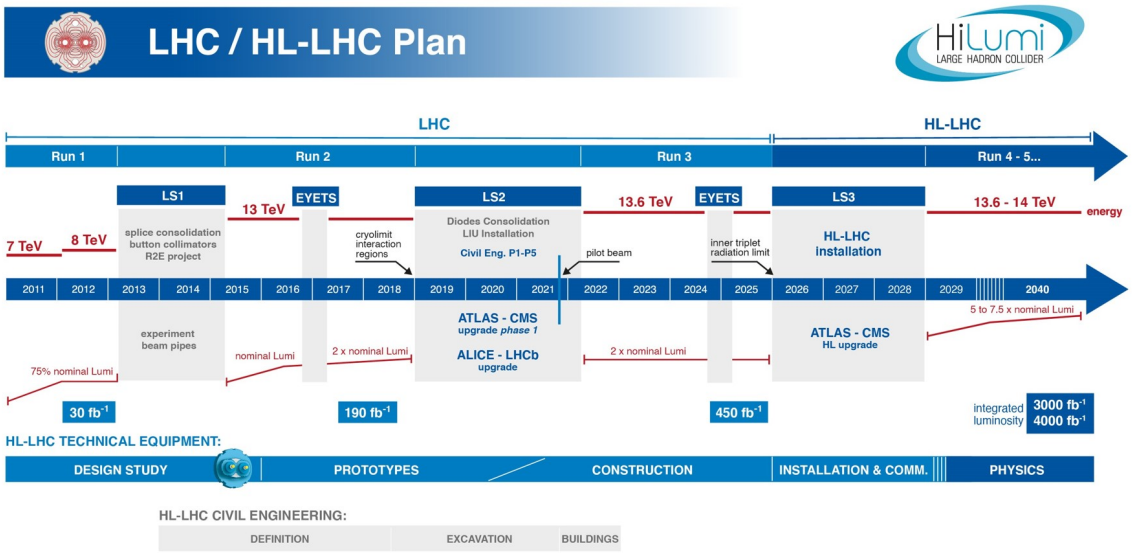

Figure 1.6: HL-LHC planned upgrade schedule, taken from [18]. The most updated one can be always consulted in [19]

During LS1, upgrades brought that the center-of-mass energy possibilities were increased from 7-8 TeV to 13 TeV, and the luminosity to 1×10^{34} cm^{-2}s^{-1}. On April 5, 2015, the LHC started RUN2, maintaining that energy during this period but progressively increasing luminosity to reach around two times the nominal value. The bunch spacing was reduced to 25 ns. RUN2 allowed for the production of lead-ion collisions of around 5 TeV. At that point, the LHC had produced a wide range of results and hundreds of scientific articles, including investigations into the different properties of the Higgs boson, precise measurements of the mass of the W boson, and the discovery of new exotic particles [e]. [16, 20]

During the period from 2018 to 2022, corresponding to an extended LS2 due to the COVID-19 pandemic, the LHC and the entire CERN accelerator complex were maintained and upgraded. One of the representative changes was the replacement of Linac2 with Linac4 (160 MeV) as an injector to the PS Booster, making it possible to upgrade the LHC injectors for higher intensity and an increase in LHC luminosity. [16]

Officially, the LHC started its RUN3 physics season on July 5, 2022, and immediately reached a record energy of 13.6 TeV, maintaining the luminosity level at $2 \times 10^3 4$ cm^{-2}s^{-1} until now as planned. This round is expected to continue until 2026. [16, 20, 21]

Notice that upgrades take place during periods of accelerator inactivity and that involves improvements to both the machine and installed experiments. This research work relates particularly to the CMS experiment upgrade, so from now on we will focus on the main aspects of this collaboration.

[e] A complete catalog of those particles can be found at www.nikhef.nl

1.5 CMS experiment

At point 5 of the accelerator ring, near Cessy in France, we can find at 100 m underground the Compact Muon Solenoid experiment (CMS), the second biggest general-purpose LHC Experiment which has a broad physics program that covers phenomena in the TeV energy range such as standard model limits, dark matter or super-symmetry evidence, and another new physics that the LHC might reveal. CMS detector was designed by layers (4 main subdetectors sections at least) in a cylindrical shape with 15 m diameter and 28.7 m long. Each layer is in turn, composed of specific strategically placed subdetectors to study the different types of particles produced in the high-energy collisions. [4, 22]

The qualificative of "compact" is well deserved because CMS, in its 14000 tons and around 5000 m^3, has a huge of high-performance technologies to study beyond standard model physics. In the region closest to the interaction point the Silicon tracker is placed (beige sectors of Figure 1.7), it is a section of several layers of high granularity detectors focused on tracking the ionizing particles. In the second and third sections (green and orange sectors of the same Figure), the Electromagnetic Calorimeter (ECAL) and Hadronic Calorimeter (HCAL) are respectively placed, they use the scintillation and photodetection principles to get the energy of the particles. A superconducting solenoid (gray sector of the Figure) divides the detector into an inner and outer region and it makes it possible to produce a strong magnetic field (∼4T) that bends the charged particle trajectories allowing it to compute their momenta. [4]

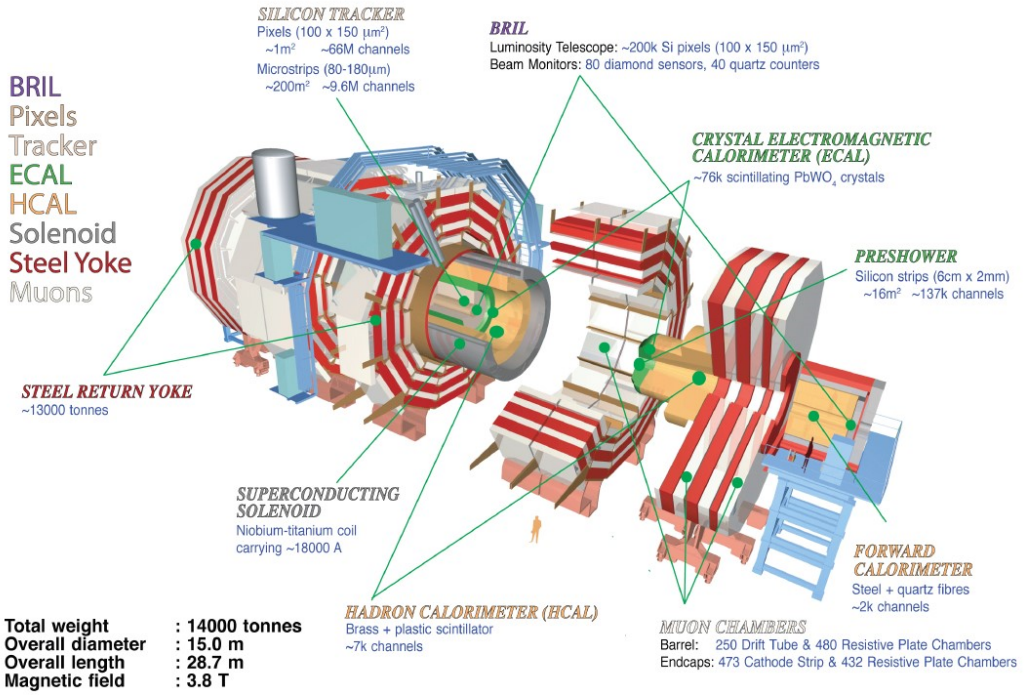

Figure 1.7: Exploded view of the CMS detector composition. Taken from [23].

In the outer and endcaps region, an important section of CMS is placed: the muon system (bone white sectors in Figure 1.7). This is a key part of the experiment because, as indicated in its name, CMS is a Muon-specialized detector, then, the Muon CMS section has several types of gaseous detectors to perform analyses of muon trajectories and other physical aspects. These few interacting particles are particularly interesting because muon detection is a powerful tool for recognizing signatures of interesting processes over a very high background rate. For example, the predicted decay of the Standard Model Higgs boson into ZZ or ZZ^*, which in turn decays into four leptons, could be achieved with very high mass resolutions in the case of the four leptons being muons. [22]

Geometrical references in the experiment (see Figure 1.8) were set in such a way that: The origin of the coordinates is located in the nominal collision point of CMS, the center. The y-axis is defined in the direction of the Zenith (differing in a slight tilt of $\sim 1.23°$ with respect to the true vertical). The x-axis is placed with respect to the ground plane, leaving from the center of the LHC ring. The z-axis is defined along the beam pipeline pointing towards the Jura mountains. This latter axis determines the positive and negative sides of the detector. [4]

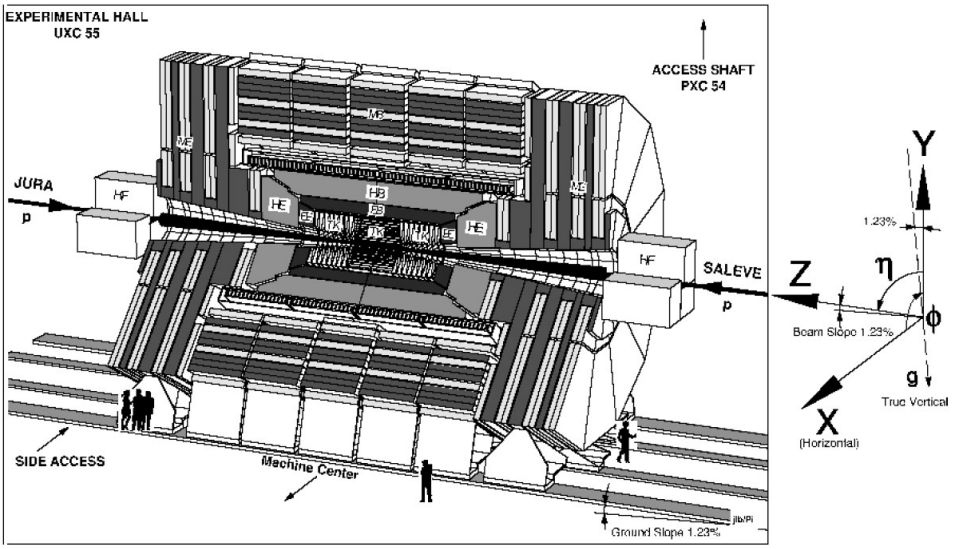

Figure 1.8: The CMS coordinate system. Taken from [4].

Because of its cylindrical shape, it should be natural the need to define the principal angles ϕ and θ, which are respectively the angle in the x-y plane from the x-axis towards the positive y-axis and angle in the z-y plane from z-axis towards the positive y-axis. Additionally, due to experimental particle physics being preferred to work with relativistic invariant quantities, instead of working with θ directly, the pseudorapidity η is selected in most of the data analysis and descriptions. It is defined by the relation (1.2): [4]

$$\eta = -\ln\big(\tan(\theta/2)\big). \tag{1.2}$$

The radial coordinate is defined as usual over the x-y plane, which is called the transverse plane and it is orthogonal to the z-axis [4].

Having a general view of the shape and location of the CMS detector subsystems, in the following sections you will find more detailed information about each of its main subsystems.

1.5.1 CMS subdetectors

Magnet

The magnet is a very important part of the detector because it bends the trajectory of charged particles and together with high-precision position measurements, allows accurate determination of its momentum. That measurement is possible with the relation (1.3) [4]

$$p = m\gamma v = qBr, \tag{1.3}$$

where γ is the relativistic factor, B is the magnitude of the uniform magnetic field to which the particle is subjected, and r is the curvature of the trajectory.

Particles with greater momentum need a strong magnetic field to be deflected. That's why CMS decided to build the currently strongest (considering the size limitations), achieving a magnetic field of 4 T (more than 100 000 times Earth's field) in the tracker region, see Figure 1.9. This feat was possible with a magnet made of superconducting coils of wire (Nb-Ti) cooled to 4.65° K, through a current of about 20 kA flows. [15, 22]

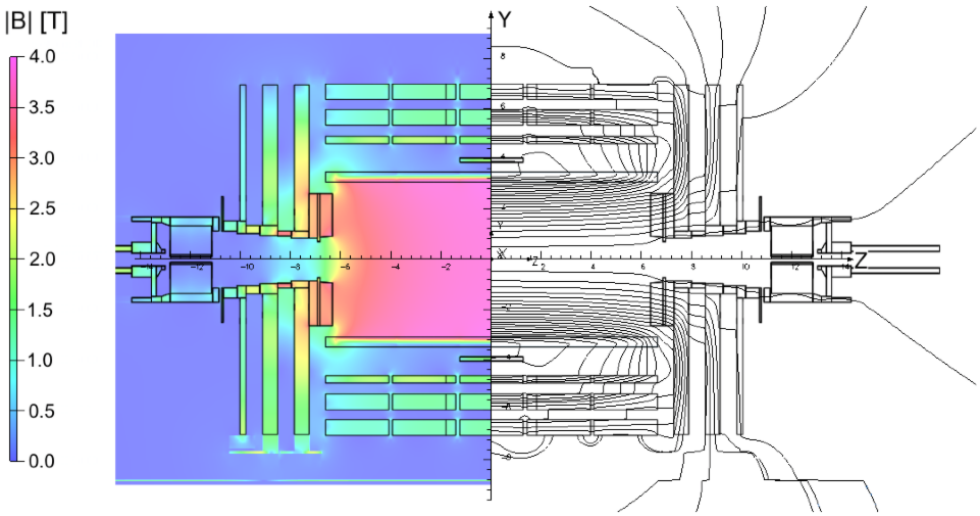

Figure 1.9: Magnetic field prediction for a longitudinal section of the CMS detector by a magnetic field model at a central magnetic flux density of 3.8 T. Left: Map of the $|B|$ field. Right: field lines. Taken from [24].

The structural support of the CMS detector is principally provided by the steel return yoke (red structure in Figure 1.7), which is an element that, in addition to containing and guiding the field, it acts as a filter of some particles, allowing through principally just muons and weakly interacting such as neutrinos. [22]

Tracker system

The closest subsystem to the interaction point has been designed to provide a precise reconstruction of the paths (and secondary vertices) of high-energy particles under hard radiation conditions. The requirements on granularity, speed, and radiation for this system led to a design entirely based on silicon detector technology. The tracker system was built with two types: Silicon pixel and silicon micro-strip detectors. [22]

The tracking volume is contained in a cylinder of 5.8 m long and 2.5 m in diameter. It was composed (its first version) of thirteen layers of detectors (3 pixel, and 10 strip layers) in the barrel, and fourteen disks (2 pixel, and 3 + 9 strips disks) of detectors in each endcap. It is possible to distinguish between the inner and outer tracker systems (see Figure 1.10). CMS tracker covers the detection region $|\eta| < 2.5$ with the major layer density contained in $|\eta| < 1.6$. [4, 22]
The *pixel* tracker system Corresponds to the innermost subdetector of the cylinder

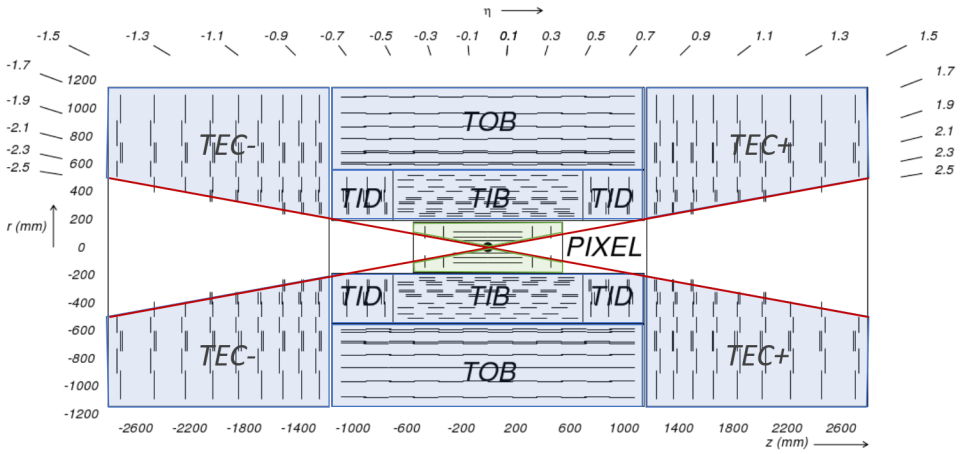

Figure 1.10: CMS tracker system configuration: Pixel, Tracker Inner Barrel (TIB), Tracker Inner Disks (TID), Tracker Outer Barrel (TOB) and Tracker EndCap (TEC). Image taken and modified from [4].

(the green region in Figure 1.10). Because it is the closest to the beam pipe, it is vital in the reconstruction of secondary vertex and trajectories of very short-lived particles. And that is why, the pixel system has an extremely high silicon pixel density, about 66 million in 1 m^2. [22]

Each layer of the pixel system is split into segments like tiny kitchen tiles, each one corresponding to a silicon sensor of around 100×150 μm^2 [f]. Its working principle is based on the electron-hole pairs signals produced by the particle and silicon atoms.

[f] 50×50 μm^2 and 25×100 μm^2 in the upgraded version.

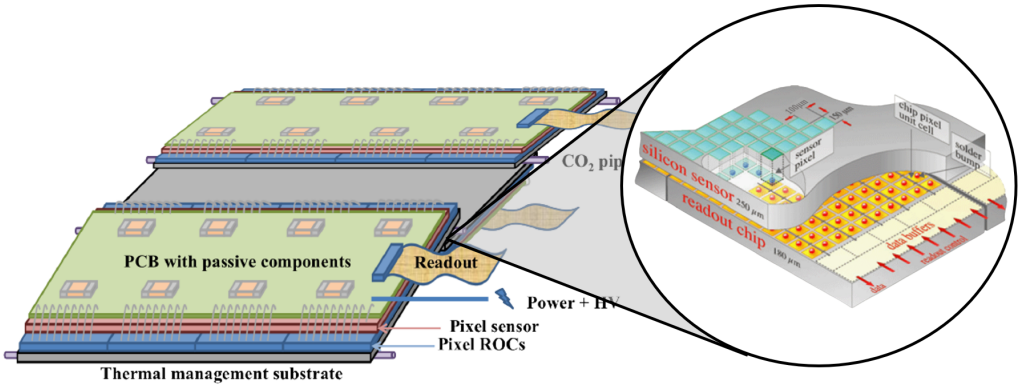

Figure 1.11: sketch of the on-detector pixel electronics system, shown for the barrel configuration with a zoomed view of the pixel configuration. Taken and modified from [23, 25]

The signal is collected by specialized electronic (readout chips - ROCs) (see Figure 1.11). [22]

The complete pixel system consisted of three 53 cm-long barrel layers[g] and four end-cap disks [h]. That configuration allows obtaining three highly precise trajectory points that were mainly used for reconstructing vertexes, principally for b and τ decays. [4, 22]

The pixel detector was upgraded during LS2. The improvement consisted of changing barrel layers and disks (and one extra) to new versions with increments in the density of pixels by making them smaller and that satisfies the requirement for the incoming RUNs. You can get details in the technical proposal for phase II of the CMS. [23]

The *silicon strips* system (outer tracker) is an arrangement of Micro strips planar sensors made of a different but strategically oriented silicon crystal [22]. As was shown in Figure 1.10, the outer tracker system is composed of an inner and outer region. The former is composed of four barrel layers (TIB - Tracker Inner Barrel) and three small disks (TID - Tracker Inner Disks) in each endcap. The outer region consists of six barrel layers (TOB - Tracker Outer Barrel) and nine big disks in each endcap (TEC - Tracker endcap). Sensor geometries are shown in Figure 1.12. [4]

The tracker system has been designed to specifically address the reconstruction of high p_T particles, with a particular interest in the isolation of electrons and, as a consequence, to isolate photons. Its work principle is based on two parallel closely spaced silicon sensors with an electronic acceptance window (see Figure 1.13) according to the bend of particles with a programmable p_T threshold. It is able to reconstruct tracks of particles with at least 0.1 GeV of p_T. Charged hadrons are reconstructed with an efficiency of at least 85% for $p_T = 1$ GeV and up to 95% for p_T above 10 GeV. [4, 26]

[g] Bpix, with 48 million pixels.
[h] Fpix, with 18 million pixels

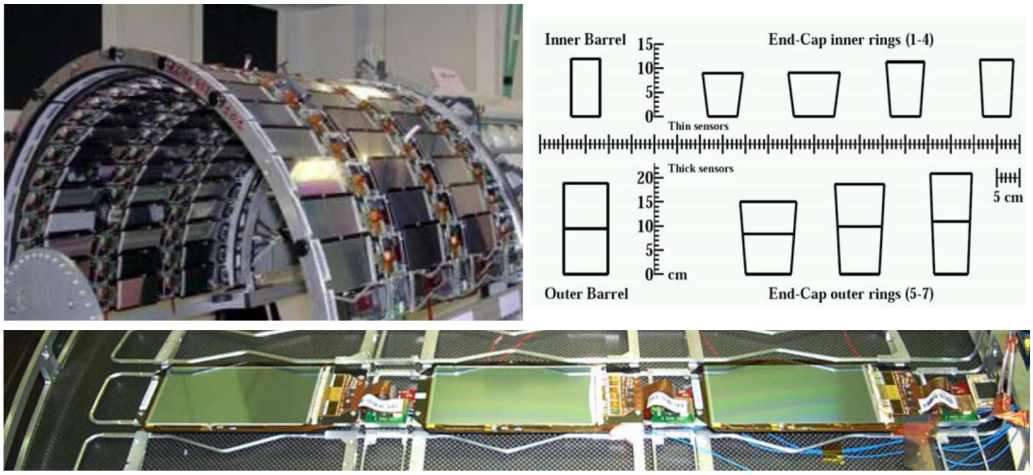

Figure 1.12: Upper left: One half of TIB layer three shells assembled and cabled at the INFN Pisa integration facility. Upper right: silicon sensor geometries utilized in the CMS tracker. Lower: Three TIB modules mounted on a layer 3 shell. [22]

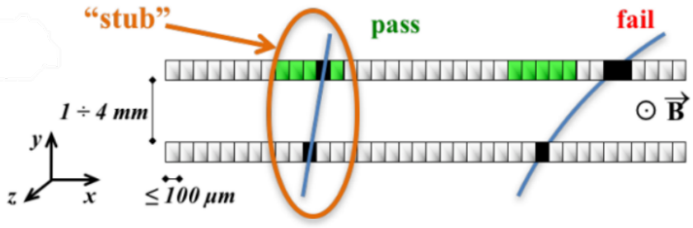

Figure 1.13: Illustration of an accepted and a rejected track according to the defined p_T window. Taken from [23]

Calorimeters

Two types of calorimeters are used in CMS to determine the energies of emerging particles. The inner one is the electromagnetic calorimeter (ECAL), which is used to measure the energies of electrons and photons with high precision. The outer one is a hadronic calorimeter (HCAL), used to measure the energy of hadrons, particles made of quarks and gluons (as protons, neutrons, pions, and kaons). Additionally, it provides an indirect measurement of the presence of non-interacting, uncharged particles such as neutrinos.

For the ECAL, a truncated pyramid crystal of lead tungstate ($PbWO_4$)(a high-density crystal $\sim$ 8.3 g/cm^3) is used as dedicated detector material due to its resistance to the high magnetic field, high levels of radiation, high transparency, and ability to scintillate when electrons and photons pass through it. The scintillator crystals produce light in proportion to the impinging particle's energy. Photodetectors, specifically designed to work within the high magnetic field, are glued onto the back of each of the crystals to detect the emitted light and convert it to an electrical signal that is amplified and sent for data processing and storage. [4, 22]

The ECAL is made up of a barrel section and two endcaps. The former consists of 61200 crystals arranged into 36 supermodules, each weighing around three tons and containing 1700 crystals. The flat endcaps seal off the barrel at each end and are made up of almost 15000 more crystals. It also contains a preshower detector that sits in front of the endcaps, allowing CMS better discrimination between photons and π_0's. Figure 1.14 shows how they can be distinguished by measuring the transverse profile of their electromagnetic showers. [4, 22]

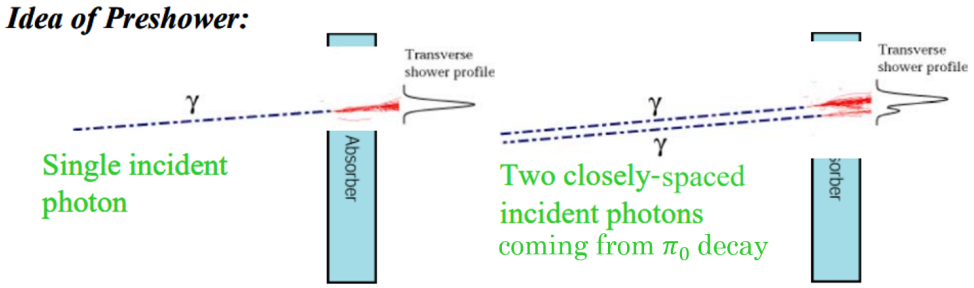

Figure 1.14: The basic principle of the endcap preshower. Taken from [27].

Because of the loss of transparency due to aging by radiation, the system requires a constant compensation correction. The aging of the crystals is measured by a laser monitoring system that measures their transparency. To validate the corrections derived from the laser monitoring, a comparison is performed between the reconstruction of electrons by the tracker and the ECAL. This calorimeter has an energy resolution typically with $\sigma(E)/E = 0.5\%$ for an energy of 50 GeV and $\sigma(E)/E = 0.4\%$ for an energy of 100 GeV, but its high dependence on temperature (about 2%/°C) makes it crucial to maintain a stable temperature in the ECAL system. [4]

Surrounding the ECAL is placed the HCAL (see Figure 1.15). This is a subdetector particularly important for the measurement of hadron jets and neutrinos or exotic particles resulting in apparent missing transverse energy. HCAL is a hermetic subsystem covering up to $|\eta| < 5.2$ which is divided into 4 sections: barrel (HB); endcap (HE), Outer (HO), and forward (HF).

Because the basic idea of this calorimeter is to stop and absorb the energy of hadronic jets. The general design is just an intercalated set of metal and scintillator layers. that what changes between every subdetector section is the type of material, and light detectors used. This is due to their positions in CMS. [4]

For HB and HE, plastic scintillators (Kuraray SCSN81), and steel and brass absorber layers are used together with Hybrid Photo Diodes (HPDs) for detection. The scintillators emit light proportional to the energy of the incident hadron (neutron, proton, pion, kaon, etc). This light is then taken to the outside via optical fiber waveguides to the HPDs that measure the amount of light. This design uses this type of diode because it is small sensitivity to the magnetic field, a critical requirement

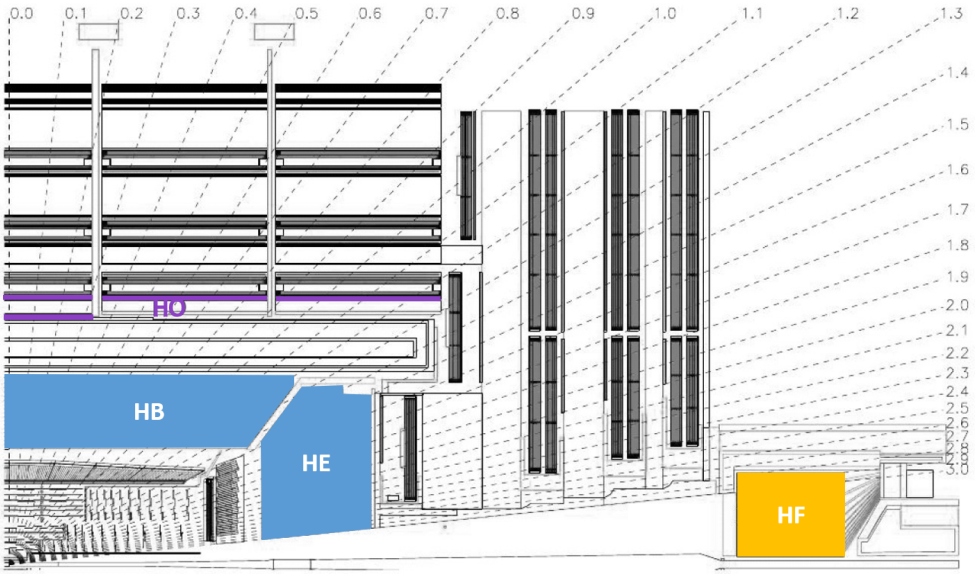

Figure 1.15: A quadrant longitudinal view of the CMS detector showing the locations of the hadron barrel (HB), endcap (HE), outer (HO), and forward (HF) calorimeters. Image modified from [22].

considering that it is placed inside the magnet. [27]

In the case of HF, a large steel absorber embedded with quartz fibers is used to produce Cherenkov light, which is detected via photomultipliers. This design is because the radiation conditions (energy of particles) increase up to seven times in the region $|\eta| > 3$ where HF is located. [4, 27]

Finally, outside the magnet solenoid, complementing the barrel calorimeter, as an additional absorber or tail catcher, the outer calorimeter (HO) is located. It is added because, in the central region, the HB and EB do not provide sufficient containment for hadron showers. [22]

Together, calorimeters and tracker systems are the fundamental pieces to identify the hadronic products of collision events. You can look up [4] to know how exactly the jets reconstruction is performed. For now, let us continue with the last detection system of CMS.

Muon system

The outer magnetic region is dedicated to muon detection. Due to the penetration power of these particles, at that point in the CMS, after crossing the calorimeters and magnet, just muons and neutrinos are expected. Therefore, CMS has dedicated their last 4 m barrel and almost 7 m endcap detector spaces to put a complete muon system composed principally of 3 types of gaseous detector technologies: Drift tubes (DT) in the barrel region, cathode strip chambers (CSCs) in the endcap region, and resistive plate chambers(RPC) in both regions (see Figure 1.16). This design aimed to guarantee efficient muon identification, precision measurement of its charge and

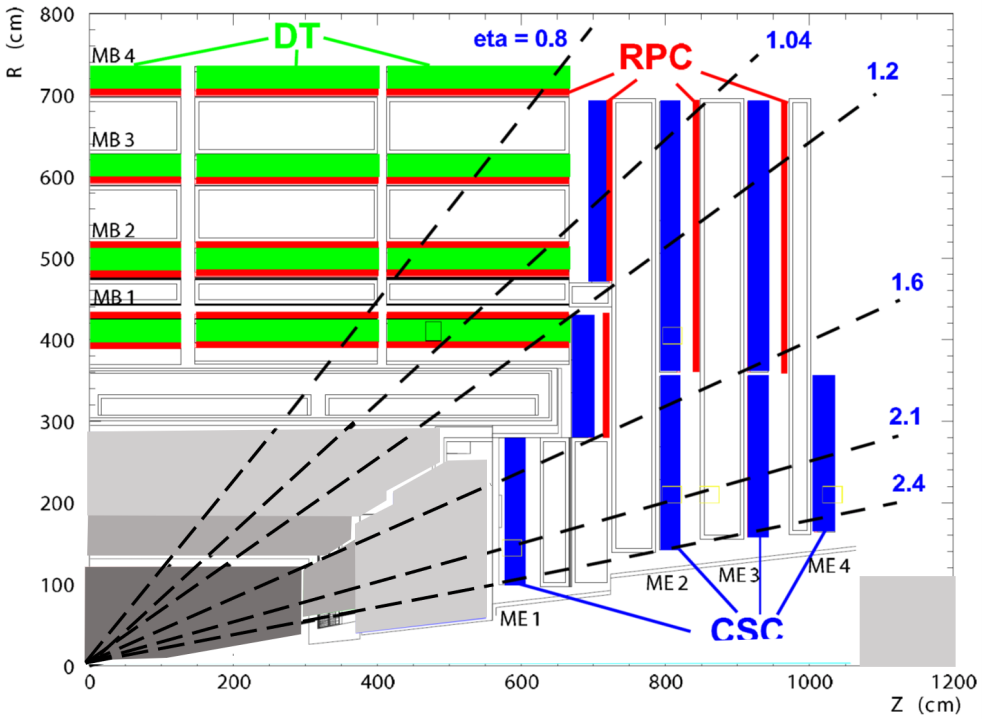

Figure 1.16: A quadrant longitudinal view of the muon system showing its chamber composition.

momentum, and a fast measurement to provide trigger capabilities. [4]

DT chambers are used in the barrel region such as tracking detectors because the neutron-induced background is small, the muon rate is low, and the ~ 4 T magnetic field is almost uniform. Under those characteristics, this technology can achieve 2 ns of time resolution and 100 μm of spatial resolution by using 172000 sensitive wires arranged in 3 "superlayers" which, in turn, are made of 4 consecutive layers of thin tubes staggered by half a tube, filled with a gas mixture of Ar-CO_2 (85-15). [22, 28]

On the other hand, CSCs are used in the two endcap regions of CMS because they reach, even with high muon rates, high background levels, and a large and non-uniform magnetic field, 3 ns and 50-140 μm (depending on chamber type) of time and spatial resolution respectively. There are 4 stations of CSCs chambers in each endcap made of 6 planes of anode wires with 7 cathode planes. [22, 28]

Finally, in both (barrel and endcap) regions, RPCs are placed principally for accurate timing and fast triggering. This is because they have an excellent time resolution of about 1.5 ns, although their spatial resolution is limited to a range of 0.8-1.3 cm. There are 480 RPCs distributed in 6 layers in the barrel with the DT and 3 layers in the endcaps with the CSC. [22, 28]

As you can notice from the previous description, the complete muon system is composed of gaseous detectors with different characteristics. That is why, a better discussion of the working principles, physical processes, and other relevant details

about gaseous detectors will be the main topic of the next chapter. For now, let us continue with the CMS experiment description.

1.5.2 Trigger and data acquisition

An implicit factor that has not been mentioned before is the nature of the beam. The hypothetical scenario of two individual particles circulating the LHC ring and colliding is merely for illustrative purposes. You would agree that this process would be highly inefficient, especially when considering that the production of rare or short-lived particles is statistically infrequent. Such a scenario would require hundreds of collisions to occur before obtaining an interesting result. In reality, the LHC uses a bunch structure built from protons extracted via the ionization of hydrogen gas in the Duoplasmatron Proton Ion Source. These protons, after successive injection chain steps, reach the ring in a 25 ns spaced bunches structure[i]. This way, depending on luminosity, several collisions occur at each crossing of the proton bunches (approximately 20 simultaneous pp collisions at the nominal design luminosity). [4, 22]

Taking into account that each recorded event by CMS could have a nominal size between 0.5 and 1 MB, it would be impossible to store and process the large amount of data (around 10^9 MB/s = 1 PB/s) associated with the resulting high number of events. Therefore, a drastic rate reduction has to be achieved considering that the enormous majority of events coming from pp collisions correspond to well-understood phenomena. This is where the trigger system steps in. [4, 22]

The trigger system is the start of the physics on-line event selection process. The rate is reduced in two steps called Level-1 (L1) Trigger and High-Level Trigger (HLT), respectively. The former is hardware-based, and the latter is software-based. They reduce the data flux by at least a factor of 10^5. L1 reduces the data flux by two orders of magnitude, and the HLT by another three orders of magnitude. [4, 22]

The L1 trigger system begins by receiving data from subsystems (muon system and calorimeters), which are then integrated into the Global trigger (GT) forming trigger objects ranked according to their significance. Then, Topological requirements (based on basic properties of the events, e.g., the content of high p_T muons, high energy electrons, photons, or hadrons) are applied to integrated data through the Trigger Control System (TCS) to decide on keeping or disregarding the event with a latency of 3.2 μs. This decision time is achieved thanks to the front-end pipelined memories[j]. Aiming to flexibility, L1 Trigger hardware is implemented in FPGA technology where possible, but ASICs and programmable memory lookup tables (LUT) are also widely used where speed, density, and radiation resistance requirements are important. [4, 22, 27]

The data from the detector front-ends are passed through a high-bandwidth builder network to the HLT, a CPU farm of about 10^4 cores where up to 128 fast versions of the

[i]It corresponds to a crossing frequency of 40 MHz.
[j]It can keep in memory up to 128 bunch crossings.

offline filtering algorithms can classify the collision events. Finally, HLT stores events on disks under several paths depending on the selection performed in the computing service. Figure 1.17 shows a schematic overview of the data flow steps described. [4, 22, 27]

All of the previous storage, analysis, and filtering processes are managed by the CMS Data Acquisition (DAQ) system which works at the LHC bunch crossing frequency of 40 MHz. Its architecture is shown in Figure 1.18. [22]

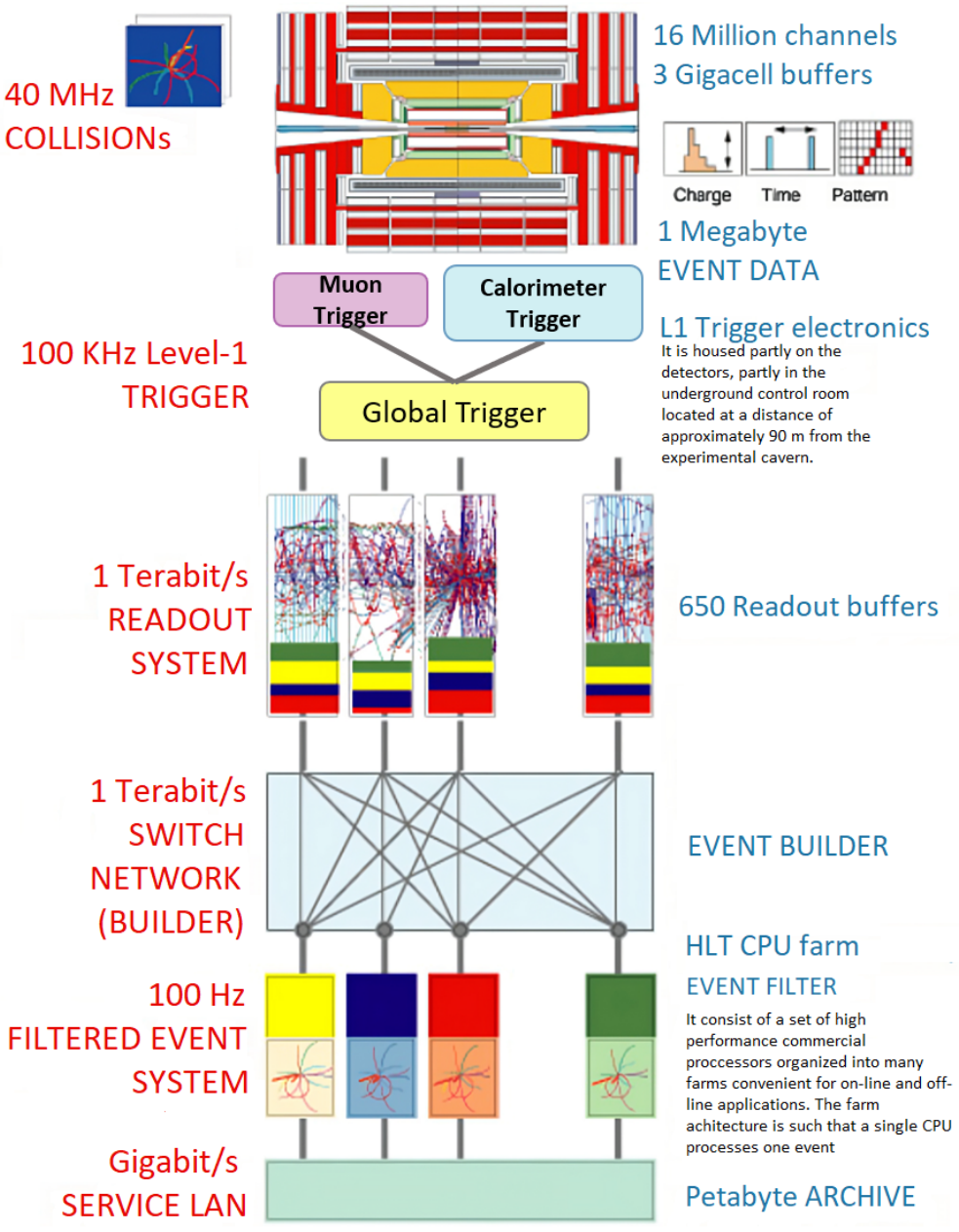

Figure 1.17: Schematic overview of data flow through the trigger and DAQ system. Taken from [29].

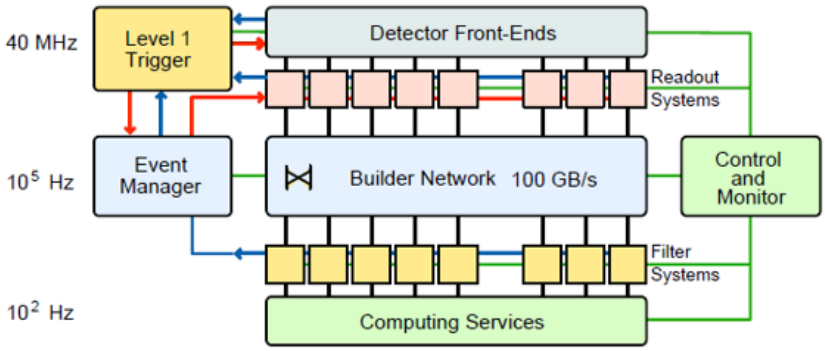

Figure 1.18: A more compressed view of the CMS DAQ system's architecture. Taken from [29].

1.5.3 CMS upgrades

As we mentioned before, LHC is improving itself. Therefore, like other experiments, CMS is undergoing a series of major upgrades before the LHC Run 4 to better exploit the LHC performance and sustain the higher luminosity foreseen for the next few years. With the HL-LHC, more data, more irradiation, and much larger rates must be handled both by the detectors and the trigger systems. Therefore, both the DAQ-trigger infrastructure and detection systems are undergoing extensive improvements, which were planned, according to the HL-LHC schedule (see Figure 1.6), to be performed in two phases mainly during LS2, YETS, and LS3. [14, 15]

These CMS upgrades include a new tracker with extended coverage and L1 trigger capabilities, new readout electronics, lower operating temperatures for the barrel ECAL, a fully redesigned endcap calorimeter named high granularity calorimeter (HGCAL), and various innovations in the muon system. For this research work, let us describe the muon system enhancement in detail [14]. You can find a detailed explanation of the other upgrades in the technical proposal for the upgrade [23].

There are three types of muon upgrades proposed: [28]

- Upgrading of existing muon detectors and associated electronics to ensure their longevity and good performance.
- Addition of muon detectors in the forward region $1.6 < |\eta| < 2.4$ to increase redundancy and enhance the trigger and reconstruction capabilities.
- Extension of muon coverage up to $|\eta| = 3$ or more to take advantage of the pixel tracking coverage extension.

Formally, complete muon system upgrades will be carried out during Phase II upgrades. However, during LS1, some points referring to the first item of the desired upgrades were performed. The CSC system was arranged with a fourth layer of detectors and an extension of the RPC system, which corresponded to the ME4/2 station and the RE4/2 - RE4/3 shown on the left in Figure 1.19 [15, 28].

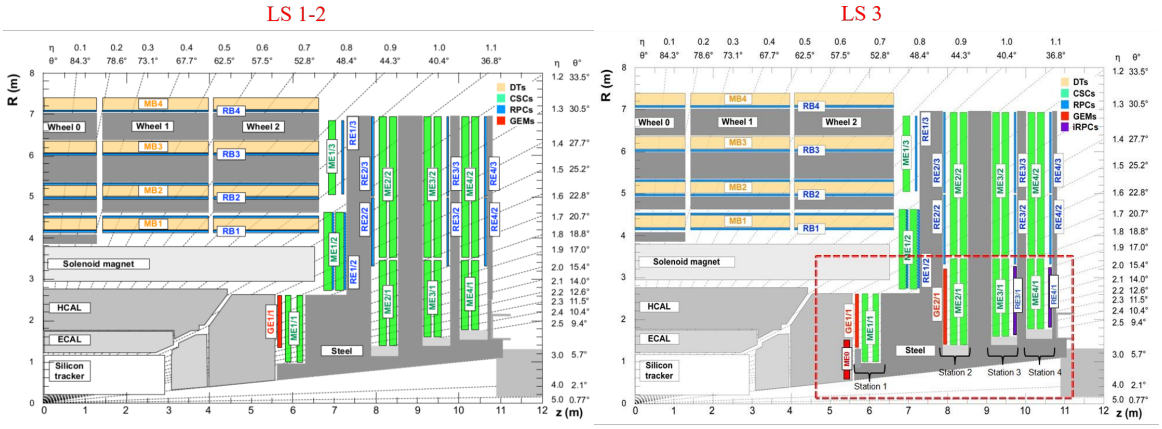

Figure 1.19: A quadrant of the CMS longitudinal cross section showing the foreseen system for Phase I (left) and Phase II (right).

During LS2, the first station of GEM-based detectors was installed, covering the pseudorapidity region $1.6 < |\eta| < 2.15$. This station is called GE1/1. During LS3, new detectors based on the RPC technology called iRPC (RE3/1 and RE4/1) will be installed, increasing the detection coverage up to $|\eta| = 2.4$. And to complete the second point of the upgrade, another GEM-based project called GE2/1 will be installed during LS3. It will also add an additional detection layer at $|\eta| = 2.4$ [15].

The last upgrade point will be achieved by adding the GEM-based project, ME0, which will increase the covered region up to $|\eta| = 2.8$, the maximum possible range due to mechanical constraints. This upgrade will improve the physics performance in many physical channels, such as multi-muon final states and very forward particle production. Figure 1.19 on the right shows the Phase II changes. [15]

The GEM-based upgrades adopt GEM technology in the form of triple-GEM chambers, a Micro-Pattern Gas Detectors (MPGD), due to their proven performance in high energy physics (HEP) experiments where they have shown high rate capabilities, fine spatial resolution, and high gain stability. They are the ideal tool for upgrading the forward muon spectrometer in CMS. A detailed description of the design and working principles of a GEM detector is given in the next chapter. For now, let us briefly describe the geometrical aspects of GEM detectors included in the CMS endcaps. [14]

The GE1/1 and GE2/1 detectors are rings of superchambers, each made up of a double layer of trapezoidal triple-GEM chambers. They cover 10.15° and 20° in the ring, respectively, and overlap in ϕ like the corresponding CSC chambers in stations ME1/1 and ME2/1. ME0 detectors also cover 20°, but each superchamber is composed of six single-layer triple-GEM chambers. GE1/1 superchambers alternate in ϕ between long and short versions due to differences in available space: the long ones cover an η range of 1.5 - 2.18, while the short ones cover an η range of 1.6 - 2.18. Therefore, 36 superchambers will be installed for the GE1/1 station in each muon endcap to ensure full azimuthal coverage. Similarly, 18 GE2/1 superchambers and 18

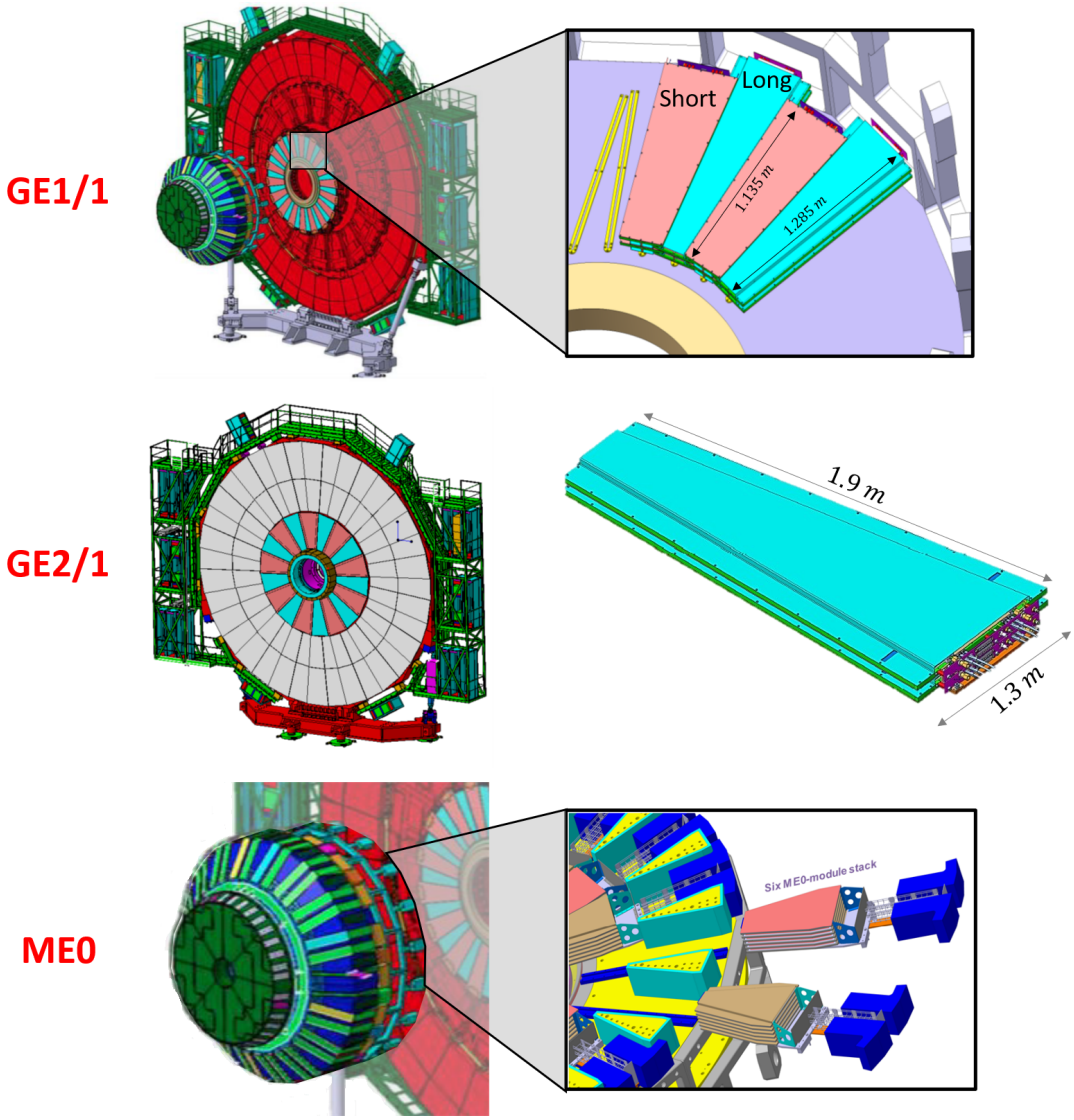

Figure 1.20: Detailed view of the GEM detectors and their location on the CMS endcaps.

ME0 stacks are needed in each endcap. A complete illustration of the GEM detector dispositions on a CMS endcap is shown in Figure 1.20. [23]

As previously mentioned, the first GEM endcap installation occurred during LS2 between July and October of 2019. However, the installation process required several prior stages, including extensive production and quality control processes to ensure optimal performance. Since 2017, approximately ten pre-production phases were conducted to establish the first assembly line and quality control procedures. These efforts resulted in successful mass production and the establishment of guidelines for subsequent GEM upgrade stages. Consequently, detector assembly and quality control processes are now well-defined and being used in the production of GE2/1 and ME0. [30]

Before delving into production and quality control tasks, it is important to first

explore the main aspects of the working principle of gaseous detectors. Therefore, this will be the focus of the next chapter, aiming to provide a better understanding of how GEM detectors operate.

Chapter 2

Overview on gaseous detectors and GEM-based detectors

Since the phase II CMS muon system upgrade has such a lead actor in triple GEM chambers, it is natural to dedicate a part of this manuscript to the understanding of their physical fundamentals. This chapter will cover the general aspects of gaseous detectors, including their historical evolution, the types of interactions that can take place, and the particularities of GEMs chambers. It will be explored how these detectors take advantage of the concept of amplification to achieve excellent characteristics, making them an important technology today. The chapter will progressively focus on the specific characteristics of triple GEM-based detectors, and the type of chambers used for the upgrade. The nature of the signals generated by muon detections will be touched providing a starting point for the next chapter.

2.1 Physical operation principle

The physical process starts when an ionizing particle arrives and crosses a gaseous or condensed medium. The important thing is that the incoming particle is energetic enough and it interacts with the atoms of the medium generating a variety of macroscopic mechanisms due to partial or complete energy transfer processes which are the ones that can be exploited to produce direct or indirect detectable signals. This interaction, in principle, is speed dependence (energy dependence). But anyway, it could imply a big set of physical phenomena. In the case of fast charged particles, they are due principally to the electromagnetic interactions between the Coulomb fields of the projectile and of the atoms in the medium. Strong or weak interactions can produce loss of energy, but their cross sections are very low compared to electromagnetic one (except in the case of neutrinos which it is the only possible interaction). [15]

Electromagnetic interactions between a crossing charged particle and a medium give rise to various processes that contribute to the particle's energy loss. Their impact is entirely dependent on the particle and the medium, for instance, in the case of a heavy charged particle (with mass much greater than the electron mass) crossing a material, the following mechanism could take place: [14, 15]

- **Atomic excitation and ionization:** Incoming particle could yield sufficient energy to an atomic electron in order to create an ion-electron pair. Here, a resonance effect could appear if the deposited energy is very similar to the medium excitation energy, in that case, target atoms will become in an exited state before releasing a photon.

- **Bremsstrahlung radiation:** When charged particles with significant momenta experience deceleration due to electromagnetic interactions with the nuclei of the material, they have the potential to release photons in the process.

- **Pair-production:** Besides ion-electron pairs, particles with kinetic energies greater than 1.022 GeV (due to interactions with the nuclei of the material) might prompt the emission of electron-positron pairs ($e^- + e^+$).

- **Coherent Cherenkov photoemission:** It occurs when a charged particle travels through a medium at a speed exceeding the speed of light in that medium ($\beta > 1/n$[a]). As the charged particle passes through the medium, the polarization of the atoms (molecules) becomes asymmetric, leading to the emission of radiation by the generated dipoles.

- **Transition radiation emission:** When a charged particle approaches a dielectric material with $n > 1$, it induces an equivalent image charge within the dielectric, manifesting as dipoles. At the moment of transition, the dipoles realign and return to a neutral configuration, resulting in the emission of radiation.

- **Secondary interactions:** Charged particles could interact with the cascade of electrons and photons generated because of primary interactions (during radiative emissions and pair productions).

In the context of gaseous detectors, focusing on the energy range typical for muons detected in CMS end-caps (the primary focus of this manuscript), certain effects may be negligible and can be disregarded. In these cases, the primary energy loss process is the production of electron-ion pairs, and the average differential energy loss can be succinctly expressed by the Bethe-Bloch formula. [29, 31]:

$$\langle \frac{dE}{dx} \rangle = -k \frac{Z}{A} \frac{\rho}{\beta^2} \Big[\ln \Big(\frac{2mc^2 \beta^2 W_{max}}{I^2(1-\beta^2)} \Big) - 2\beta^2 - \delta - 2\frac{C}{Z} \Big], \qquad k = \frac{2\pi N e^4}{mc^2}. \tag{2.1}$$

Here, N is the Avogadro number (6.022×10^{23} mol^{-1}), m and e are the electron mass and charge, Z, A, and ρ are the atomic number, mass, and density of the medium, respectively. I is the mean ionization (excitation) potential of the target; z is the charge and β is the velocity (in units of the speed of light c) of the projectile. $K = 0.1535$ MeVg^{-1}cm^2, and W_{max} is the maximum kinetic energy imparted to an e^- in a single collision[b]. In the system used, the rest energy of the electron, mc^2, equals

[a] n is the refraction index of the medium.
[b] For $M >> m$, $W_{max} \approx 2mc^2\beta^2/(1-\beta^2)$.

0.5110 MeV. Finally, δ and C are, respectively, a density effect correction (important at high energy) and a shell correction (already important at low energy). [29, 31]

It is customary to substitute the length x for a reduced length X, defined as $x\rho$ and measured in gcm^{-2}, i.e.: [31]

$$\langle \frac{dE}{dX} \rangle = \frac{1}{\rho} \langle \frac{dE}{dx} \rangle. \tag{2.2}$$

The value of the effective ionization potential I is material-dependent, but a rather good approximation could be $I = I_0 Z$, with $I_0 = 12$ eV. In the case of gas mixtures, average values for Z, A, and I have to be taken. [31]

The Bethe-Bloch formula is applicable across a broad spectrum of materials, encompassing gases to solids, and integrates major of the mentioned interaction mechanisms. Minor discrepancies become apparent, especially with extremely lightweight materials ($Z < 7$). On the other hand, it is not valid when applied to crystals because of their ordered structure, leading to preferred paths, which are called the channeling effect. Notably, electrons and positrons stand out as exceptions due to their sharing indistinguishable traits with the electrons within the material.[14]

It is also important to bear in mind that the ionization of atoms is a stochastic process that undergoes fluctuations. So, In the case of thick materials with $dx > 1$ g cm^{-2}, where the number of individual interactions is sufficiently high, the distribution of the deposited energy follows a Gaussian distribution, as it satisfies the Central Limit Theorem (CLT). However, for our specific case of interest, where the medium is gaseous and very thin (3 mm, as we will discuss later), the distribution loses its symmetry and transforms into a Landau-Vavlilov distribution. [14, 15]

As evident from equation (2.1), the energy loss depends on the velocity of the projectile, making it convenient for experimental and analysis procedures. By sweeping the velocity, the so-called stopping power curve can be obtained (an example of positively charged muons on copper is shown in Figure 2.1), which shows a fast-decreasing function of the particle velocity before reaching a minimum, then slightly increases to an approximately constant value before continuing to increase as radiative effects become predominant due to relativistic influences. This region is referred to as the minimum ionizing region and indicates the energy range where an ionizing particle would cause the minimum ionizing interactions. Typical muons to be detected in CMS end-caps have an average energy loss close to that minimum, then, they can be considered for practical estimation such as Minimum Ionizing Particles (MIP). [15]

Produced electron-ion pairs, which are known as the *primary charges*, diffuse throughout the volume via random thermal processes[c]. These primary electrons might have enough energy (larger than the ionization potential of the medium) to further

[c]It will be addressed later because it is an essential subject that determines the positional accuracy of a gaseous detector.

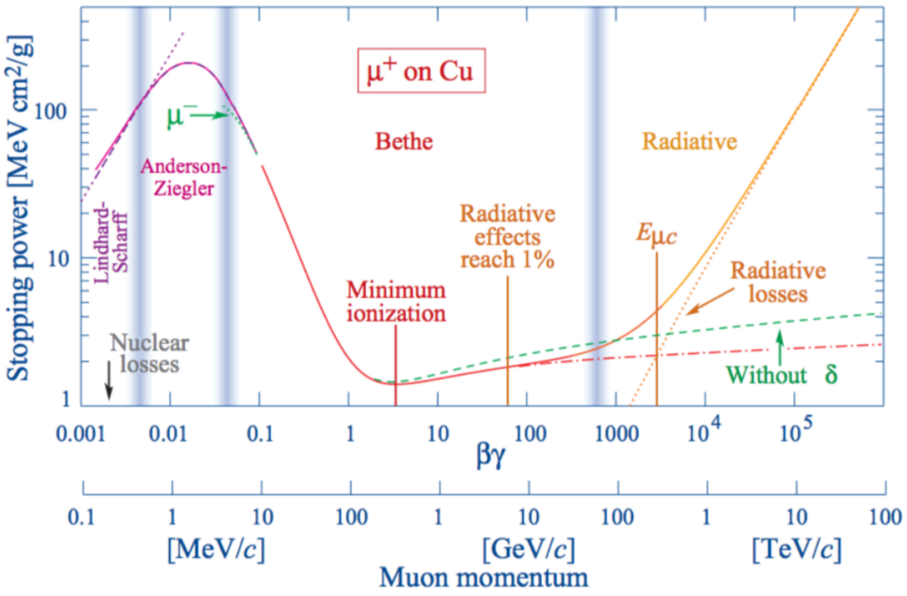

Figure 2.1: Stopping power as a function of the particle momentum for positively charged muons traversing copper. Taken from [14].

ionize other gas atoms, generating clusters of secondary charges. Therefore, the total number of electron-ion pairs present in the gas after an ionization event is the sum of primary and secondary charges, i.e., $n_T = n_P + n_S$. Conveniently this can be estimated by computing [31]:

$$n_T = \frac{\Delta E}{W}, \tag{2.3}$$

where, ΔE is the total energy loss in the gas volume considered, which can be computed using the Bethe-Bloch formula (2.1). And, W is the average energy required to create an electron-ion pair in the gas.

The gaseous detection principle relies on these charges produced by ionization. Precise measurements allow us to identify different types of ionizing particles since the number of primary ionizations and their spacing depend on the gas (or gas mixture), the type of radiation, and its energy, as we have seen. However, a direct measurement could turn difficult considering that produced charges quickly lose their energy in multiple inelastic collisions with the medium and assume the average thermal energy distribution of the gas (see [31] for an explicit analysis).

One way to counteract this is by applying an electric field that increases the energy of the charges, thus favoring charge multiplication phenomena. This results in an adequate amount of detectable charges that diffuse until they reach the electrodes of a specialized device for readout of the ionization current (see Figure 2.2 left). Therefore, the focus shifts to properly adjusting the magnitude of the electric field, favoring desired processes and preventing undesired ones. Additionally, if a structure is added

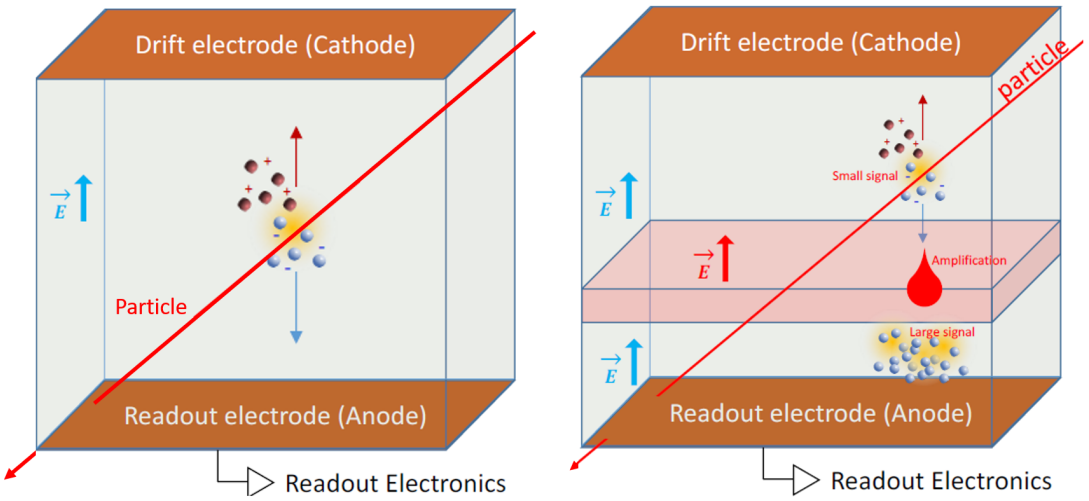

Figure 2.2: Schematic view of the physics principle of a gaseous detector. Taken from [6].

inside the gas volume, an extra amplification of the charge can be produced before it goes towards the readout electrode (see Figure 2.2 right). This fact is used in most of the gaseous detectors of our interest, particularly in GEM-based detectors, which will be explored later in this chapter.

The charge multiplication phenomena can be identified as an electron avalanche, which is a well-known process that principally depends on the gas and the applied electric field. Figure 2.3 shows the general behavior of the primary charges produced in a gaseous chamber (or cavity) as a function of the applied electric field. It is important to note from the curve that there are some values of the electric field for which the multiplication curve differs significantly depending on the nature of the ionizing particles (proportional region), while other ranges are indistinguishable. This fact can be exploited for different detection purposes. The clearest example is the case of Geiger-Muller detectors, which use high electric fields to produce an amount of primary charge that does not depend on the nature of the ionizing particle, making it commonly used as a counter. It should be noted that the electric field should be selected to avoid regions where, due to the high electric field, electric discharges start to occur inside the cavity. Additionally, the electric field should not be too low as it can lead to slow charge multiplication and undesired collision and recombination effects.

More interesting to us is to focus on gaseous detectors that use noble gases mixed with organic vapor [d] operating in the proportional region (where recombination effects can be neglected) to identify specific types of particles. This means that the electric field produces accelerations with energy that exceeds the ionization potential of the atom or molecule in the gas. Under these conditions, primary and secondary charges follow the paths determined by the field lines and inelastically collide, ionizing more

[d]Noble gases are usually preferred to just polyatomic molecules in particle detection because they don't show too many de-excitation channels. [15]

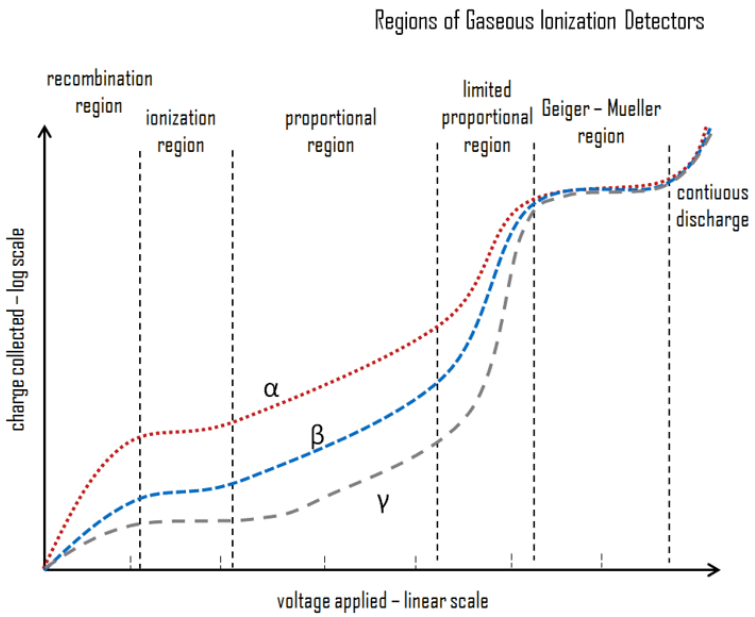

Figure 2.3: Amplification Curve of Gaseous Detectors. It shows how charge multiplication curves as a function of the applied electric field behave differently depending on the nature of radiation. Lines for α, β, and γ radiation is shown. Taken from [32].

molecules and producing an avalanche effect, which can be modeled by the *Townsend model*.

Defining the ionization coefficient (also known as the first Townsend coefficient[e]), as $\alpha = \lambda^{-1}$, we can describe how the number of electrons in a given position n increases after traveling a distance dx by $dn = n\alpha dx$. Integrating over a path length x, we obtain: [33]

$$n = n_0 e^{\alpha x} \tag{2.4}$$

The Townsend coefficient is a quantity that encloses the physical properties of the gas such as density, pressure, and temperature, and it is electric field-dependent as it is shown in Figure 2.4.a for noble gases. In the b side of the figure, it is possible to notice that the behavior is completely different in the case of a mixture of gases and those effects could be leveraged to set the desired detector characteristics.

Equation 2.4 is clearly the product of an approximation. Nevertheless, since the early developments of gaseous detectors, the study of the statistical fluctuation of the generated avalanche was investigated because of its importance in energy resolution. An extended and more detailed treatment of this topic can be found in [33], so here only the final result of the deduction will be presented.

For any avalanche starting with n_0 primary electrons, we can write the expression to the distributions of the final avalanche size such as:

[e]which simply means the inverse of the mean free path that an electron has to travel before having an ionization collision

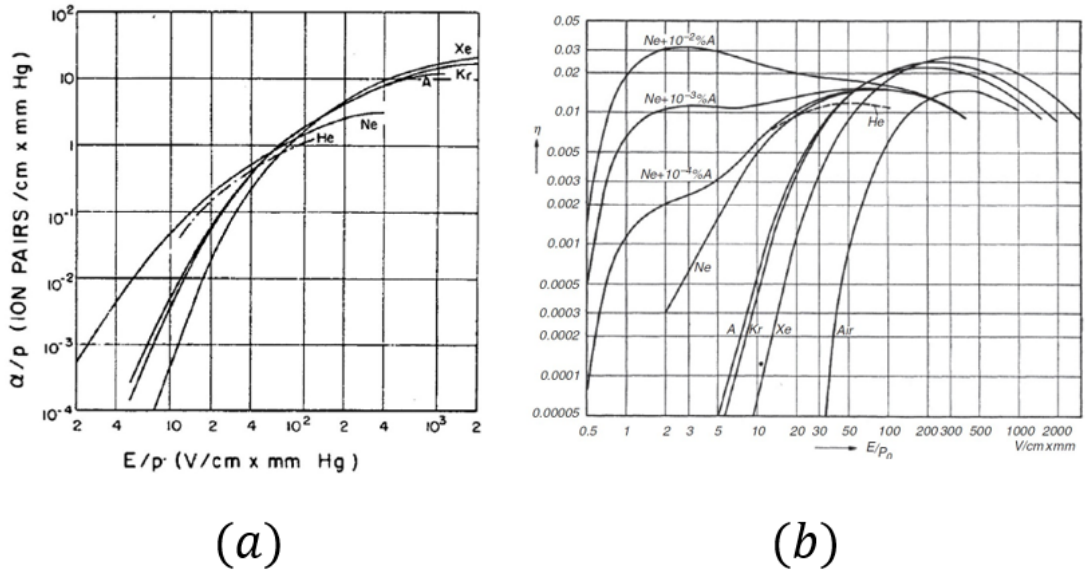

Figure 2.4: (a) First Townsend coefficient as a function of the field for the rare gases; (b) Ionization coefficient in rare gases and mixtures. [33]

$$P(n, n_0) = \frac{1}{\overline{n}} \left(\frac{n}{\overline{n}}\right)^{n_0 - 1} \frac{e^{-\frac{n}{\overline{n}}}}{(n_0 - 1)!}, \tag{2.5}$$

where $\overline{n}$ is the average avalanche size for one electron. This distribution is functionally identical to a Poisson distribution in the parameter $\frac{n}{\overline{n}}$.

In terms of detector performance, it is useful to compute a multiplication factor defined as:

$$M(x) = \frac{n}{n_0} = e^{\alpha x}. \tag{2.6}$$

In the case of a non-uniform electric field, it should be written as $M = e^{\int_{x_1}^{x_2} \alpha(x) dx}$.

The goal is to set the detector parameters to achieve a sufficient multiplication factor that can produce a detectable signal by the readout electronics. However, unfortunately, the multiplication factor cannot be increased arbitrarily. An inappropriate choice of detector parameters may cause the transition from the proportional avalanche region to a streamer and eventually to a spark breakdown. The reason is essentially that secondary ionization processes in the gas and on the walls, produced by photons emitted in the primary avalanche, spread the charge over the gas volume and induce modifications of the electric field, which strongly increases in front of and behind the multiplying charge. An illustration of this phenomenon is shown in Figure 2.5. If the streamer is not damped by the detector geometry or a reduction of the electric field, it can propagate through the entire gas gap, leading to a spark breakdown. [33]

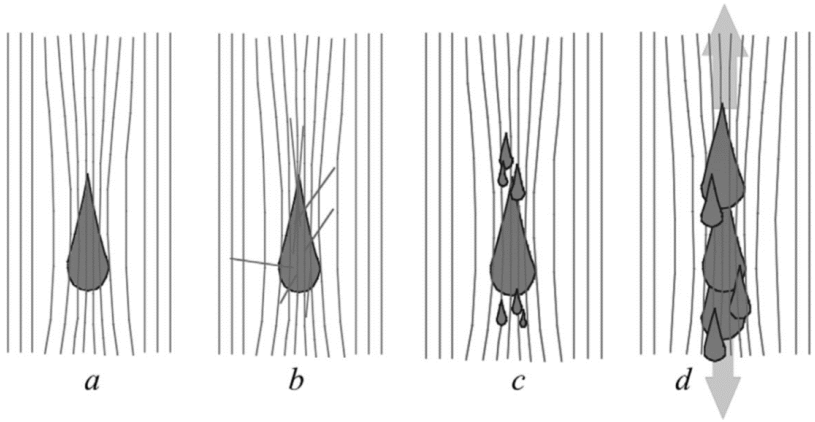

Figure 2.5: (a) the high density of ions and electrons in the avalanche modify the original electric field, increasing it in front of and behind the avalanche; (b) photons emitted isotropically from inelastic collisions in the avalanche front create secondary electrons by photo-ionization of the gas molecules; (c) secondary avalanches then develop from electrons created in the regions of higher field; (d) and the process continues with a forward and backward propagation of the charges, starting a streamer. Taken from [33].

The limit to the proportional avalanche multiplication before the transition to the undesired region is given by the empirical Raether's limit: [33]

$$\alpha x < 20,$$

or a total avalanche size (product of initial ionization and gain) of around 10^8. However, experimentally, the statistical distribution of the energy of electrons, and therefore of the gain, generally does not allow one to operate gaseous counters at average gains above around 10^6 to avoid breakdown. [33]

In practice, M is usually expressed as an absolute gain, which is defined simply as the ratio between the collected charge in the electrode of the detector and the primary charge. One way to measure the gain is through direct measurement of the detector current under a controlled irradiation source. As we will see in Chapter 4, particularly for GEM detectors, this is the procedure performed during a quality control known as QC5. Therefore, Measurements of the current I and rate R under exposure to radiation with a known ionization yield, such as a soft X-ray source, can be made to determine the absolute gain M at a given voltage: [33]

$$M = \frac{I}{n_0 e^- R}. \tag{2.7}$$

To complete the explanation of the operational principles of gaseous detectors, let's retake the matter of charge diffusion and motion in an electromagnetic field, with a discussion based on the insights presented by [14].

Charged particles generated by ionizing events tend to diffuse within the gas medium and recombine through natural thermal processes. However, as they are influenced by electric and magnetic fields, their trajectories involve a combination

of thermal motion, drift caused by the electromagnetic field, and collisions with gas atoms and molecules.

Here It is necessary to distinguish between the motion of ions and electrons. For the former, let's assume they have zero velocity immediately after a collision with any particle in the cavity. Driven by the electric field (Magnetic fields have negligible effects on ions), ions will move until a collision occurs at a time τ, where their velocity reaches a value given by:

$$v^+_{\max} = a \cdot \tau = \frac{eE}{m^+}\tau, \tag{2.8}$$

where e, E, and m^+ represent the electron charge, the applied electric field, and the mass of the ion in motion, respectively. Considering that the average drift velocity (referring to the component of the averaged velocity aligned with the applied field) is half of the maximum one, the equation for the ion's drift velocity is then given by:

$$v^+_D = \mu_+ E, \tag{2.9}$$

with $\mu_+ = \frac{e\tau}{2m^+}$, known as ion mobility, taking typical values of around 1-2 cm^2 s^{-1} kV^{-1} for commonly used gases. [14]

The analysis of the drift motion of electrons, on the contrary, is quite different since their significantly lower mass, enabling them to readily gain kinetic energy. In this scenario, we can contemplate a time interval that exceeds the characteristic time between collisions ($\Delta t >> \tau$), and then, consider the velocity such as the average over this interval. The collisions can be conceptualized as viscous friction, which is proportional to the velocity. Therefore, The equation of motion for the electrons becomes:

$$\langle m_e \frac{d\mathbf{v}}{dt} \rangle = e\Big(\mathbf{E} + \mathbf{v}^-_D \times \mathbf{B}\Big) - \frac{m_e}{\tau}\mathbf{v}^-_D = 0, \tag{2.10}$$

which, after simplification, results:

$$\mathbf{v}^-_D = \mu_- \mathbf{E} + \omega\tau(\mathbf{v}^-_D \times \mathbf{B}), \tag{2.11}$$

where $\mu_- = e\tau/m_e$, and $\omega = eB/m_e$ is the Larmor frequency.

One important thing to consider in this case is that the motion will be influenced by the type of gas employed. Gases can be broadly categorized into two types based on electrons' mobility: hot and cold gases. The distinction lies in how much energy an electron may lose upon colliding with an atom or molecule. In the case of cold gases, characterized by several low-energy freedom levels, collisions result in a significant loss of energy, leading to an almost constant μ_- and behavior akin to ions. Conversely, in hot gases, the loss of energy is smaller, so, μ_- becomes proportional to τ, and not constant as electric fields increase. An example of a hot gas mixture is Ar-CH_4, while Ar-CO_2 is a cold gas. [14]

The diffusion processes, which in the absence of an electromagnetic field involve thermal motion characterized by the diffusion coefficient D, depending on the mean free path λ and the typical collision time τ as $D = \lambda^2/\tau$, transform into a magnitude of two components, namely longitudinal (D_L) and a transversal (D_T), when applying an external electric field in one direction. The nature of the gas also plays a role in this phenomenon. In hot gases, $D_L > D_T$ due to the kinetic energy spread in the electrons' cloud, resulting in significant diffusion. Conversely, in cold gases, the two components are similar and small, getting closer to the pure thermal diffusion. Which is characterized by a time evolution following the equation of charge conservation, with the solution:

$$\rho(r,t) = c \cdot \exp\Big(-\frac{r^2}{4Dt}\Big). \tag{2.12}$$

Additionally, when a magnetic field comes into play, it does not impact the longitudinal component of diffusion, but it restricts the transversal component. This occurs because the Lorentz force works to keep the electrons' cloud together by causing the charges to spiral around the longitudinal axis. As a result, the transverse diffusion coefficient becomes limited and takes the form of: [14]

$$D_T(B) = \frac{D_T(0)}{1+\omega^2\tau^2}. \tag{2.13}$$

Further details are available directly from [14] and [33].

Finally, there is one more crucial process that may occur during the journey of charges within the gas, potentially influencing the gain factor and overall performance of the gaseous detector. Along this path, electrons have the potential to be absorbed by atoms or molecules, forming negative ions. This phenomenon is particularly notable in the presence of highly electronegative elements, such as oxygen or fluorine. Hence, it becomes imperative in gaseous detectors to maintain a continuous gas flow in the cavity to safeguard it from contaminants, such as the oxygen found in the air or the accumulated ions after interactions. The latter is a critical aspect since it is closely related to the aging problems of gaseous detectors. [14]

2.2 Types of gaseous detectors

The described physics forms the basis for almost all gaseous detectors known to date, which have been applied and evolved according to desired performance since the beginning of the 20th century. Due to their simple construction, Parallel Plate Avalanche Counters (PPACs) have been used in the past and are still widely used in particle physics with several improvements. However, they suffer from basic limitations such as the detected signal being dependent on the avalanche length (the point of release of the primary ionization) and the presence of large statistical fluctuations in the avalanche size. Therefore, more sophisticated designs have been developed [33].

The first significant contributions in this direction were made by Rutherford and Geiger when they extended the concept of gaseous detectors to cylindrical tubes

known as proportional counters. They chose a cylindrical coaxial geometry with a thin metal wire stretched on the axis of the cylinder (and insulated from it). This is the basic idea behind the well-known Geiger counters. However, while single-wire proportional counters are widely used for the detection and measurement of ionizing radiation energy loss, their localization capability is limited by the physical size of the counter. Fortunately, a major improvement was achieved by G. Charpak and his collaborators in the 1960s with the conception and successful testing of the first multi-wire proportional chamber (MWPC), which led to the seed image of the electronically-readout detectors of the modern era. Let us now take a brief tour of this and other important gaseous detector designs that have been conceived. [15, 33]

2.2.1 Multi-wire proportional chambers

A MWPC consists of a set of thin, parallel, and equally spaced anode wires placed symmetrically between two cathode planes, typically with gas gaps three or four times larger than the wire spacing (see Figure 2.6). When a sufficiently strong voltage is applied, an electric field is developed that amplifies the primary charge in the region near the wire, similar to the proportional counter. Due to the availability of several wires, a spatial resolution of $\sigma = \text{pitch}/\sqrt{12}$ is achieved[f], where "pitch" refers to the separation between wires. Also, in Ar-CO_2 mixtures, those types of detectors could reach time resolutions of the order of 10 ns. [15, 33]

On the other hand, these detectors come with certain disadvantages. The long ion drift path, approximately 100 μs of travel time, leads to an accumulation of positive charge within the gas volume, constraining the detector's rate capability. They are also vulnerable to geometric alterations, making operation and manufacturing challenging. Additionally, they face issues associated with classical aging effects, requiring specific conditions for prolonged operational efficiency. [15, 33]

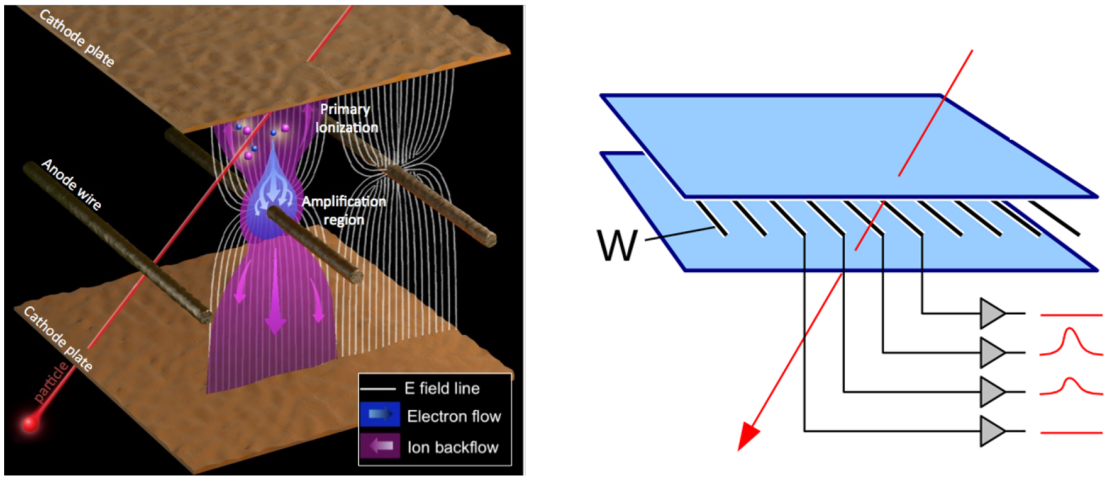

Figure 2.6: Schematic view of an MWPC and its working principle. Taken from [6].

[f]This can be improved by adding more detection layers and/or segmenting the cathode.

2.2.2 Multi-tube arrays

Gaseous detectors with a multi-wire geometry are susceptible to accidental wire rupture, which can lead to the malfunctioning of a significant portion or even the entire system. To mitigate this issue, multi-tube arrays enclose each anode in a cylindrical tube, protecting surrounding elements from local failures.

The design is modular in nature, and each constituent element could be a typical proportional counter. This design serves as the foundation for the drift tubes used in the muon system of CMS (check its description in chapter 1). Figure 2.7 shows the real design used in the DT chambers of the barrel region of the muon system.[33].

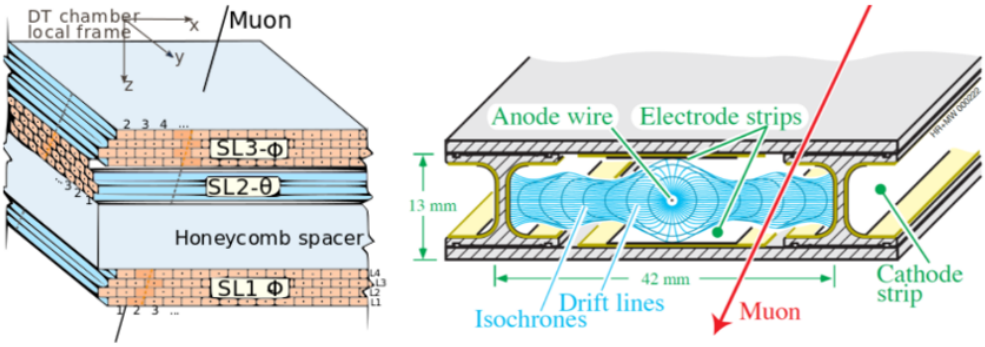

Figure 2.7: Schematic view of the Drift tube system installed on CMS. Images taken from [25].

2.2.3 Resistive plate chambers

Wire-based detectors have inherent limitations in achieving high time resolution due to the statistical distribution of primary ionization clusters and the dispersion caused by diffusion during amplification. To achieve the desired response, one solution is to apply very high electric fields, but this would push the detector to its critical operation point. To address this problem, the Resistive Plate Chamber (RPC) was developed, which can achieve high gains while limiting the discharge generated by large current surges resulting from an avalanche. RPCs are gaseous detectors with high-resistance electrodes made of graphite or other suitable materials (see Figure 2.8 left). Graphite has high electrical conductivity and can dissipate charge build-up on the surface of the plates quickly, allowing the detector to operate at high voltages without experiencing breakdowns or other electrical instabilities. Its high resistivity also helps to limit the discharge current during the formation of an avalanche. [33]

2.2.4 Micro-pattern gaseous detectors

Thanks to the advances in the semiconductor industry, specifically in microelectronics and photolithographic technology on flexible and standard PCB substrates, it was possible to build an electrode thickness of about 100 mum with a very good position

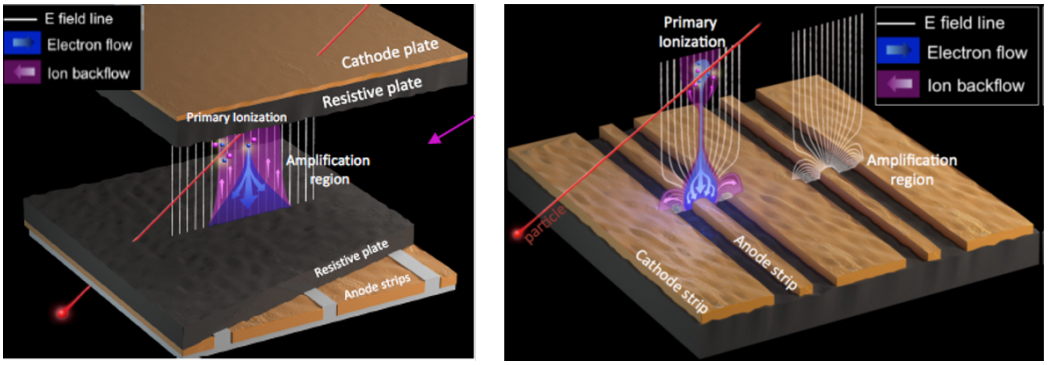

Figure 2.8: Schematic view of an RPC (left) and an MSGC (right). Taken from [6].

accuracy. Therefore, aiming to address the localization and rate limitations of wire-based detectors, A. Oed introduced the micro-strip gas counter (MSGC) in 1988 (see Figure 2.8 right).

The MSGC provides full electron collection efficiency due to its field lines. Moreover, the transverse dispersion of the avalanche during multiplication reduces positive ion backflow in the drift gap and field distortions, improving crucial factors such as the rate capabilities of the detector. The MSGC consists of thin parallel metal strips on a thin insulating support with alternating anodes and cathodes, and an upper electrode that delimits the sensitive gas-filled drift gap. With a pitch of 100 μm or less, it offers an order of magnitude improvement in granularity over wire chambers. The MSGC has been shown to achieve gains over 10^4, space resolution down to 30 μm RMS, and rate capabilities over 10^6 Hz/mm^2. However, a problem appears in this design. The close distance between the electrodes can cause discharges and permanent strip damage in cases of high-energy releases, limiting the electric field that can be applied and the gain of the chamber. [15, 33]

The limitations of MSGC technology in long-term experiments and harsh environments can be addressed by returning to the proportional plate counter combined with the micro-strip anodes and, with an intermediate structure to achieve a pre-amplification of signals. They are known as Micro-pattern gas detectors (MPGDs). They are capable of achieving comparable performance, but they are more resistant to radiation and damage. [33]

The MPGD's configuration allows for large gains with decreased sensitivity to gap variations and imperfections. One well-represented example is the Micro-mesh gaseous chamber (MMGC or Micromegas). This detector came up in 1996, and it consists of a thin metal grid stretched at a small distance, 50 to 100 μm, from the readout electrode. Electrons released in the upper drift region are collected and multiplied with large gains with a high field applied across the gap, typically above 30 kV/cm. Furthermore, this geometry enables the separation of the active volume from the multiplication one. Since the overlying drift field is generally much smaller, most ions are collected on the cathode mesh, minimizing the charge backflow into the drift

gap. Additionally, the use of a high resistivity layer insulating the multiplication gap from the anode helps to dump the discharges before a full breakdown, similar to the approach used for RPCs. See Figure 2.9. [33]

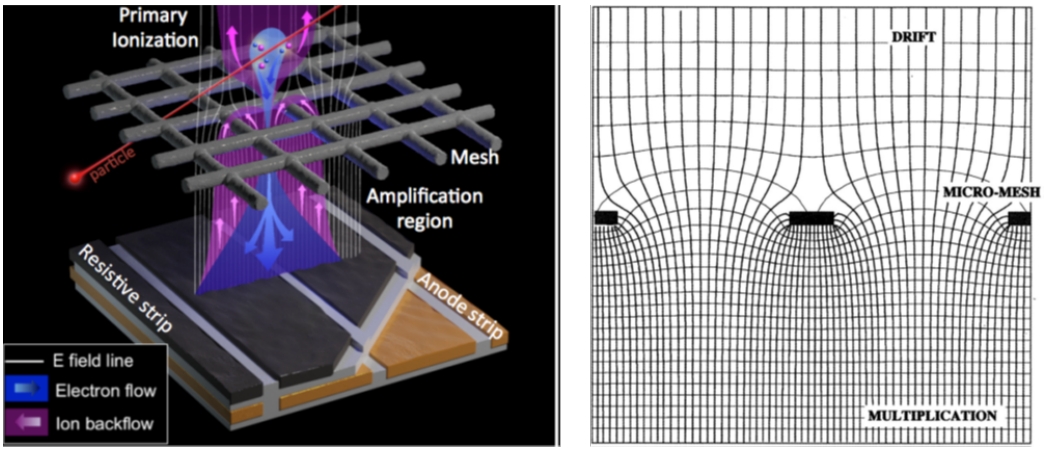

Figure 2.9: Schematic view of a Micromegas detector and its electric field. Taken from [6, 33].

Another important representative of MPGD is the Gas Electron Multiplier (GEM), introduced by F. Sauli in 1997. It focuses on improving the signal pre-amplification in MMGC detectors. Due to the significant role of this type of detector in this work, let us dedicate a detailed discussion to it. The next section will cover the main aspects of the working principle of these types of gaseous detectors in detail. It will also highlight some of the studies that led CMS to include triple-foil GEM-based detectors as part of its muon system.

2.3 Gas electron multiplier - GEM

Inspired by the same basic concept described above and others that also were developed (Multi-step avalanche chambers), the gas electron multiplier (GEM) uses a thin polymer foil, metal coated on both sides and chemically pierced with photolithography techniques with a high density of holes (typically 50 - 100 mm^{-2}) as micro-pattern structure, inserted between drift and a charge collection electrodes (see Figure 2.10). A standard foil used in CMS GEM chambers has 60 μm thickness[g], 70 μm holes, and 140 μm pitch in a hexagonal pattern (See Figure 2.11). [35]

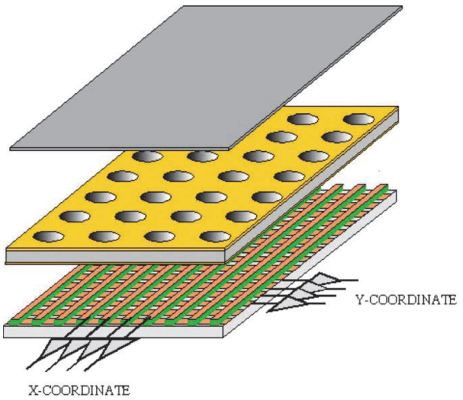

Figure 2.10: Schematics of a single-GEM detector with two-dimensional strip readout. Taken from [34]

[g] 50 μm for the polyimide, and 5 μm for the copper.

The design is thought to drift into the holes every electron released by ionization in the upper region (DRIFT) and take advantage of the geometry to produce a significant electronic multiplication due to the high density of electric field lines ($\sim$ 80 kV/cm), produced by putting large difference of potential between the two face of the foil, see Figure 2.12). This electric field drifts the electrons to the lower region (TRANSFER) when it can be collected by electrodes, which can be patterned with, e.g., strips in two dimensions as is shown in Figure 2.10. So, in essence, a GEM foil acts as a charge pre-amplifier which to a large extent preserving the original ionization pattern. The main fact in this design is the goal of achieving high gain without the need to apply very high voltage ($<$ 600 V), which was the cause of many of the problems of previous designs. [35]

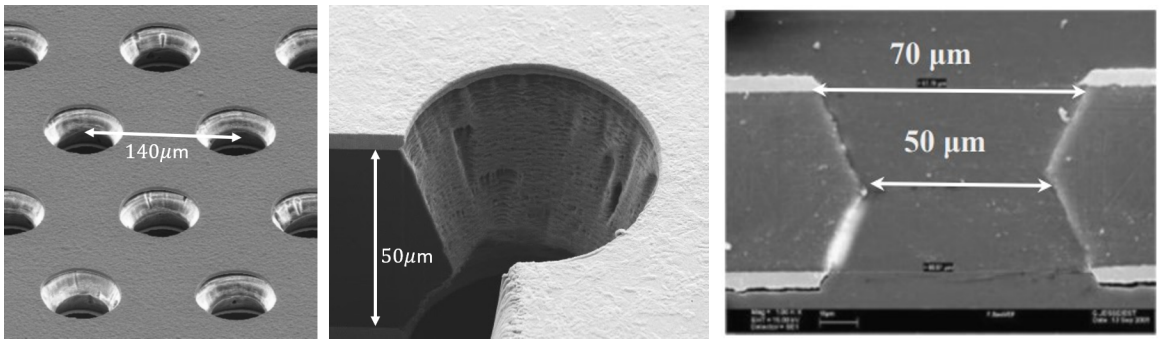

Figure 2.11: Microscopic view of a GEM holes structure. Taken from [6, 33].

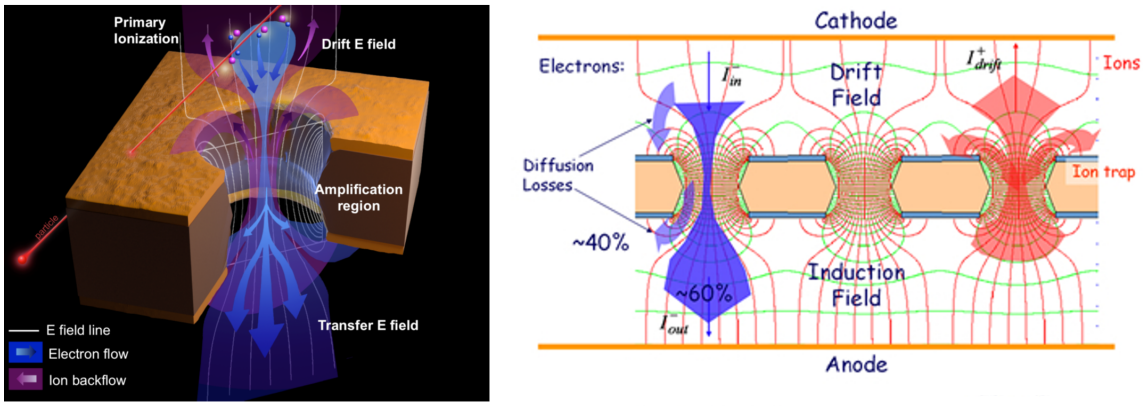

Figure 2.12: Left: schematic view of the electric field lines (white), electron flow (blue), and ion flow (purple) through a bi-conical GEM hole. Right: Illustration of the charge multiplication principle of a single-GEM detector. [28, 34]

Unlike other gaseous detectors, the GEM anode generates a signal solely through the collection of electrons, without any input from positive ions in motion, which can make the device very fast and help to minimize space charge issues. The moderate field strength between the multiplying and sensing electrodes, known as the transfer or induction gap, also lowers the risk of a discharge propagating to the sensitive front-end readout electronics. [35]

Since its introduction in 1997, several studies have been conducted to improve the performance characteristics of the GEM chamber. Starting with the mechanical aspects, it was observed that the diameter and shape of the holes have a direct influence on the detector's performance and long-term operational stability. One important result was to ensure high extraction efficiency (the ratio between the total charge of the avalanche inside the GEM holes and the extracted amount from the foil), the hole diameter should be comparable to the foil thickness, as shown in plot (a) of Figure 2.13. Studies on the transparency of the foil (the fraction of electrons transferred through the GEM foil) showed that it is drift field-dependent and follows the behavior depicted plot (b) of Figure 2.13. From this, it is evident that the suitable value of the drift field should not be very high or very low. Moreover, considering what was learned before, the choice of gas plays an important role in the performance of any gaseous detector. For CMS GEMs, an Ar-CO_2:70-30 gas mixture was chosen, and the proportions were tested to ensure desired performance. The different gains achieved as a function of the gas mixture are shown in plot (c) of Figure 2.13. Similarly, other characteristics of the detector have been thoroughly studied, which can be found in documents resulting from the R&D phase of GEM chambers [28], as well as in [35].

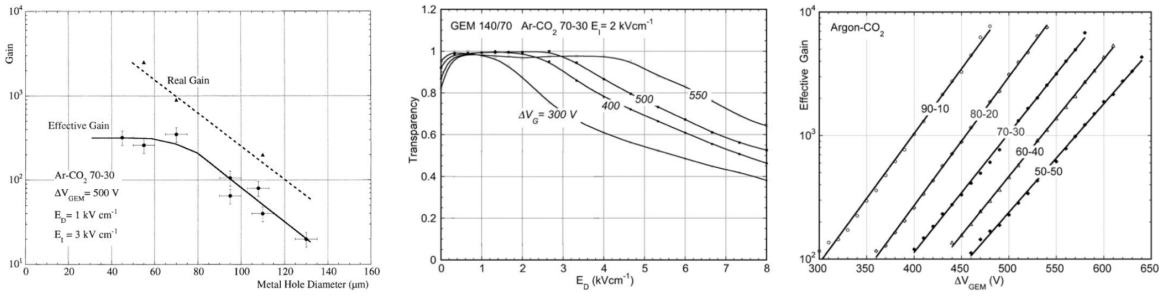

(a) (b) (c)

Figure 2.13: (a) Foil extraction efficiency. Notice that because a field-dependent fraction of the multiplying electrons is collected on the lower face of the GEM electrode (see Figure 2.12), the useful or effective gain is lower than the real gain of the multiplier. (b) Foil transparency. (c) Effective Gain for different gas mixtures. [35]

In general, single-GEM electrodes can reach gains of around 10^3 (less if the manufacturing conditions are not favorable). However, similar to other micro-pattern devices, the probability of getting discharges increases when higher gains are required (i.e., higher voltages) or in case of high-rate beam environments (see Figure 2.14.a). Studies have revealed that multi-GEM configurations can achieve better performance by acting as multiple pre-amplification steps, allowing for the application of moderating operating voltages to achieve desired gains (see Figure 2.14.b). Double and triple GEM configurations are the most widely used but work such as those by Bondar et al. (2003), Dehmelt (2015), and Nath Patra et al. (2018) have tested and compared the performance of quadruple and quintuple GEM devices. [35]

Each parameter of the chamber should be carefully selected to achieve the optimum operating performance in terms of gain, ion backflow, and discharge. Particularly,

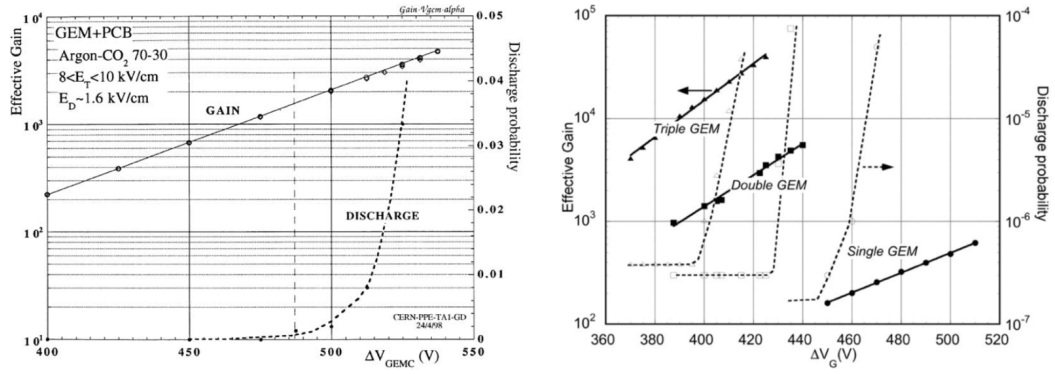

(a) (b)

Figure 2.14: (a) Single-GEM gain and discharge rate as a function of voltage. (b) Effective gain of a single-, double- and triple GEM detector measured on soft X- rays. [35]

the triple GEM configuration is the one that CMS chose to include for upgrading the muon system. Therefore, the next section will cover this specific type of GEM chamber, including the characteristics used for the CMS upgrade.

2.4 Triple GEM detector

Three identical GEM foils are stacked between an anode-cathode cavity filled with gas with separations (from top to bottom) of 3 mm, 1 mm, 2 mm, and 1 mm to form a triple GEM chamber (see Figure 2.15). Each GEM, as mentioned earlier in this chapter, plays the role of an intermediate structure that ensures the production of higher detectable charge avalanches, and the specific layout mentioned was chosen for its significant signal amplification and low discharge probability. A distance of 3 mm is sufficient to ensure ionization of more than 99.9% of minimum ionizing particles. The 1 mm distance between GEM1 and GEM2 (transfer gap 1) maintains a thin structure while preventing foil contact and redirecting electrons. Transfer gap 2 requires a 2 mm distance to reduce the probability of discharge between GEM3 and GEM2. Finally, a 1 mm induction gap was chosen to minimize signal drift time. [14]

As stated previously, the gas mixture used in CMS GEM detectors is Ar-CO_2:70-30. This choice was made because, while it may not have the highest efficiency in terms of electron diffusion and discharge probability, the mixture has positive attributes in other important areas. For example, it is non-flammable and has no impact on the greenhouse effect. Additionally, the absence of polymerizing gas makes it optimal for use in harsh radiation environments. [14]

The GEM voltage primarily determines the gain of the device, while drift, transfer, and induction voltages mainly regulate the flow, spread, and collection of electron and ion charges. The specific voltage scheme used for the CMS GEM chambers is shown also in Figure 2.15. In particular, for CMS GEMs, each voltage is applied through simple resistive voltage dividers, which is the simplest method. However, other stud-

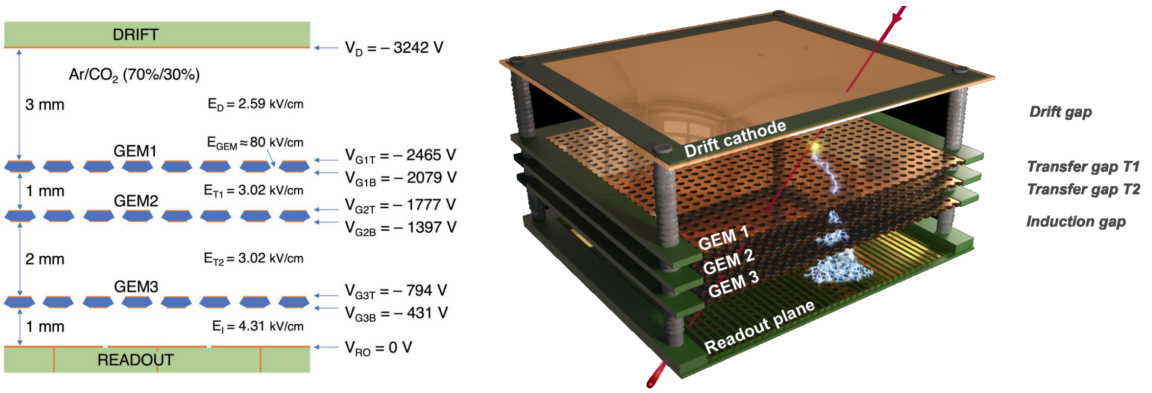

Figure 2.15: Left: schematic view of the geometrical gap sizes inside a triple GEM chamber. They also show typical values for electric potentials on the seven electrodes and typical values for voltages and electric fields across the four gaps and holes. Right: Illustrative view of charge multiplication processes in a triple GEM configuration. Taken from [14, 6].

ies have implemented individual power supply systems to allow more flexibility in choosing voltage sharing [36]. The asymmetry in GEM voltages is a result of studies that showed that a decreasing amplification factor over the three stages provides the lowest probability of discharges propagating [37].

The nature of the signals produced in this GEM chamber is quite fascinating, as its design allows for good temporal resolution and avoids the tail effects caused by the ions and charges resulting from the diffusion of electrons through the chamber. Let's take a closer look at this.

The signal induced in the readout board strips begins when electrons exit the GEM3 holes. This induces an increasing current as the electrons reach the anode strips, followed by a return to the baseline. As a result, a single cluster of electrons would produce GEM signals with a steep rise, a narrow flat central part, and a steep fall. However, since ionizing particles can generate multiple clusters, a train of (partially) overlapping signals is induced on the readout (see Figure 2.16). In the Triple GEM design, significant effects caused by ion diffusion are unlikely because ions are quickly collected by the foils, without interacting significantly with more gas atoms. This means that the GEM signal is determined purely by the electrons, resulting in very good achieved temporal qualities considering their high mobility and that it depends solely on the time of arrival of the nearest ionization cluster. [14]

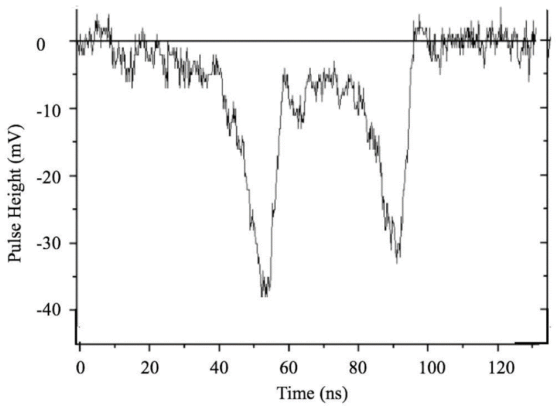

Figure 2.16: Fast signals recorded on the GEM anode. Two tracks separated by less than $\sim$ 20ns are well resolved. [35]

The last assertion has a small loophole, as primary ionizations can occur anywhere inside the cavity. However, you will likely agree that only those originating in the drift gap would be considered, as all others undergo amplification at least twenty times smaller, making them less significant in the overall collected signal. This means that the time resolution will primarily depend on the distance of the nearest primary ionization from GEM1 foil and the drift velocity of electrons in the gas, which was previously explored in the last part of Section 2.1. With that in mind, in the case of a CMS GEM, the expected chamber's time resolution is anticipated to be approximately 5 ns, as indicated by the estimation provided by [14].

In addition to intrinsic time resolution, we can consider another parameter, the width of the signal, which, as shown in the figure, corresponds to around 70 ns. This estimation can be made using reasoning similar to the previous one, by considering the spatial difference between the farthest and nearest primary ionizing clusters, resulting in an approximate temporal difference of 43 ns. To this, we should add the rising and falling time, which can also be estimated at around 13 ns. [14]

The last signal characteristic that we can explore is the amplitude of the signal. For this estimation, it is necessary to ask ourselves how many primary charges would be produced in the drift region when a muon crosses it. This estimation can be done by using the concepts developed at the beginning of this chapter.

Let us use the expression 2.3. Therefore, we need to compute the total energy loss first. For that, since we are using a gas mixture (Ar-CO_2:70-30), we need to compute:

$$\left\langle \frac{dE}{dx} \right\rangle_{\text{Ar-CO2}} = \rho\text{mix}\Big[0.7\Big\langle \frac{dE}{dX} \Big\rangle_{\text{Ar}} + 0.3\Big\langle \frac{dE}{dX} \Big\rangle_{\text{CO}_2}\Big], \tag{2.14}$$

where, for a MIP[h], we have [38]:

$$\begin{aligned}
\left\langle \frac{dE}{dX} \right\rangle_{\text{Ar}} &= 1.519 \text{ [MeVcm}^2\text{g}^{-1}\text{] at } \rho_{\text{Ar}} = 1.662 \times 10^{-3} \text{ [gcm}^{-3}\text{]}, \\
\left\langle \frac{dE}{dX} \right\rangle_{\text{CO2}} &= 1.819 \text{ [MeVcm}^2\text{g}^{-1}\text{] at } \rho\text{CO2} = 1.842 \times 10^{-3} \text{ [gcm}^{-3}\text{]}, \\
\rho\text{mix} &= 0.7\rho_{\text{Ar}} + 0.3\rho_{\text{CO}_2} = 1.716 \times 10^{-3} \text{ [gcm}^{-3}\text{]}.
\end{aligned}$$

Therefore,

$$\Rightarrow \left\langle \frac{dE}{dX} \right\rangle_{\text{Ar-CO}_2} = 2.761 \text{ [keVcm]}.$$

With this, we can get the average energy deposited by a muon in the 3 mm drift gap of a GEM detector as:

$$\Delta E = \left\langle \frac{dE}{dX} \right\rangle_{\text{Ar-CO}_2} \cdot 0.3 \text{ cm} = 828.3 \text{ [eV]}. \tag{2.15}$$

[h]Remember that typical muons to be detected in CMS end-caps can be considered such as Minimum Ionizing Particles.

Finally, we can take $W_{\mathrm{Ar}} = 25.5 \pm 0.3$ eV and $W_{\mathrm{CO_2}} = 32.6 \pm 0.1$ eV from [39] and compute 2.3 as:

$$n_T = \Delta E \left[\frac{0.7}{W_{\mathrm{Ar}}} + \frac{0.3}{W_{\mathrm{CO_2}}} \right] \approx 30 \text{ pairs.} \tag{2.16}$$

After obtaining this result, let's assume the best-case scenario where the Triple GEM is operating with an effective gain of 10^4. Following three charge transfer multiplications, the anode could potentially collect approximately $\sim 3 \times 10^5$ electrons, or equivalently, receive a charge of approximately ~ 50 fC. Clearly, this is just an approximation since this exact value depends, for example, on the rate of received radiation, or statistical fluctuations of electrons production and diffusion.

Although it may seem like a minuscule signal to process, the CMS GEM detector implements a sophisticated data acquisition system. This system can effectively analyze these small detections through a powerful specialized ASIC called VFAT. However, this is an extended topic, which we will cover in a separate chapter. For now, the next section will discuss the specifics of configuring GEM detectors for the CMS upgrade.

2.5 GEM in CMS: GE1/1, GE2/1 and ME0

The last section of chapter 1 introduced well the desired location and geometries for GEM chambers on CMS detectors, and the previous discussion described the working principles of this technology, so, we can now highlight some aspects of the internal structure forming of the specific GEM detectors used for the CMS Muon upgrade. All three detector versions are Triple GEM-based chambers, differing principally in geometrical aspects and dose radiation conditions (see Figure 2.17). For that, let us take the GE1/1 chamber as the illustrative base.

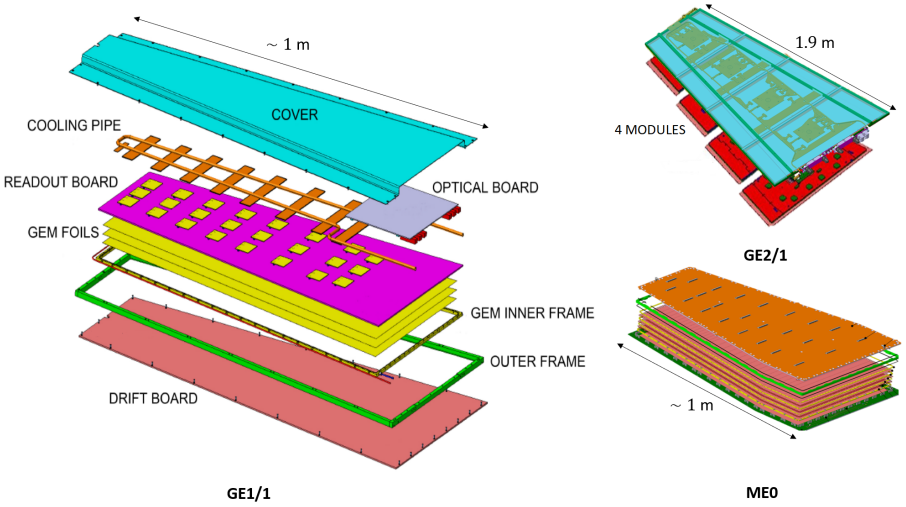

Figure 2.17: Exploded view of the three types of detectors. Taken and modified from [28, 6].

At the heart of the chamber, there are three GEM foils spaced in the 3-1-2-1 configuration forming the drift, transfer, and induction regions, as mentioned before. The plastic internal and external guide frames help maintain this spacing. The foils are sandwiched between a drift and a read-out board, with the former acting as the cathodic plate and the latter as the anodic plate. The drift board is a double-layer PCB board with a simple drift copper cathode surface on its inner side and a 140 μm ground copper plane on the outer side. The anode board is a PCB that is finely segmented into radial strips along the ϕ direction, each with a pitch of 461 μ rad (see Figure 2.18). [14, 28]

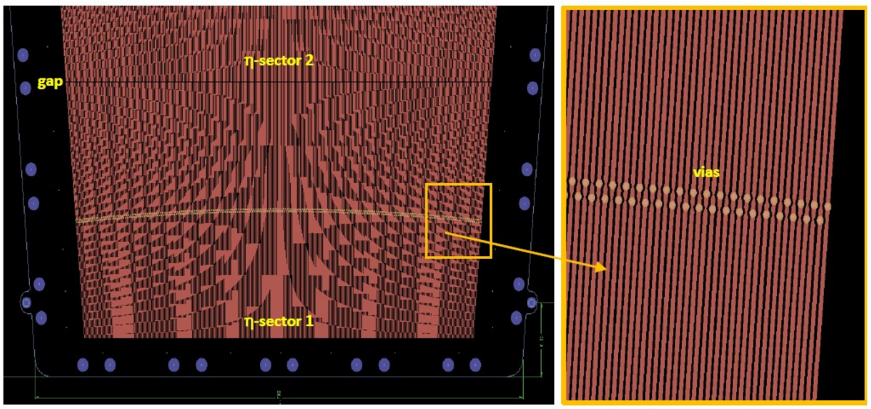

Figure 2.18: Close-up of readout strips on the inner part of the readout board. Taken from [28].

The read-out board is divided into 8 regions (η partitions) along the longitudinal axis of the chambers, each with 384 strips. Each partition is then subdivided into three groups of 128 strips. The traces from these groups are routed from the vias to 130-pin connectors that are used by the front-end VFAT (see Figure 2.19). [28]

The last components of the chamber are the cooling system and the aluminum cover. The cooling system, made entirely of copper (plate and pipe), dissipates heat from the on-chamber electronics through 16 °C water injection. An aluminum cover, together with the back of the drift board, creates a Faraday cage that protects the read-out strips and electronics from external RF noise interference [14].

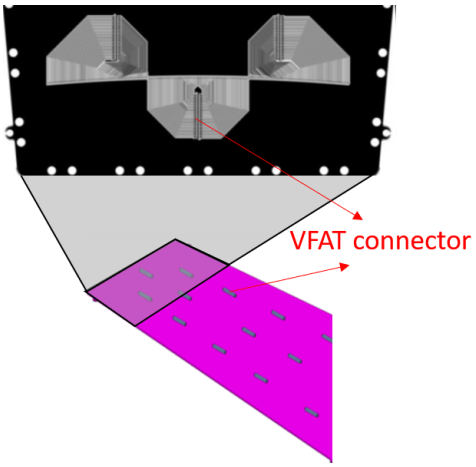

Figure 2.19: Close view of the outer side of the readout board. VFAT connectors are marked. Taken from [28]

As mentioned in Chapter 1, GEM ring endcaps are assembled using puzzle-based GEM superchambers. Referring to Figure 1.20, it can be observed that the

GE1/1 case consists of two GEM chambers (Chosen strategically based on their gain and working point characteristics) attached to each other. A long and short version of GE1/1 is needed due to its position in the CMS detector. Similarly, GE2/1 and ME0 superchambers are assembled from two chambers.

It is worth noting that GE2/1, due to its large size, must be divided in a modular way to avoid discharge problems caused by high capacitance in large-area GEM detectors. To complete a GE2/1 superchamber, eight slightly different triple GEM modules (M1 to M8) are used (see Figure 2.20).

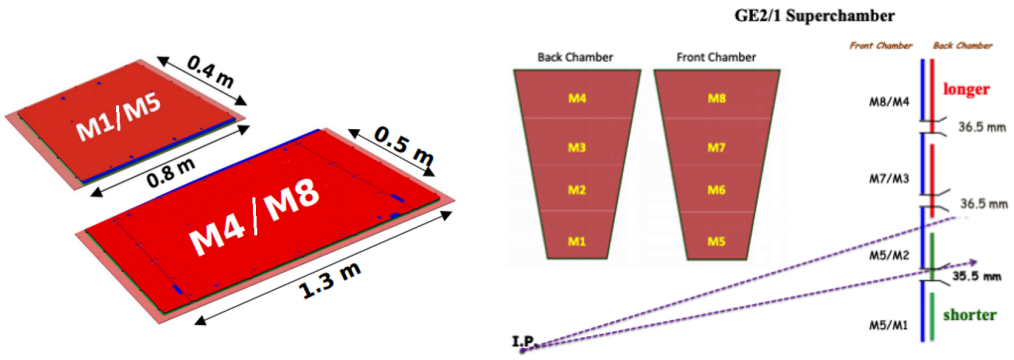

Figure 2.20: GE2/1 superchamber, modular composition. Taken and modified from [28].

Deeper details on the manufacturing and quality control test processes will be explored in the upcoming sections, particularly in the last chapter. For now, let us return to the problem of the small GEM signal that readout strips would receive in case of muon detection. The next chapter will show how GEM electronics was designed and implemented to collect, transport, and analyze detection, including the front and back end CMS GEM electronics.

Chapter 3

GEM data acquisition system (DAQ)

The GEM detector physics was well described in the previous chapter. There, after the crossing of an ionizing particle an amplified electric signal through the readout board, which is divided into sectors of 128 strips (refer to sec. 2.5), is gotten. Those analog lines are the starting point of the DAQ system. They are connected to the electronic system through a 130-pin Panasonic connector placed on the outer side of the read-out PCB. The GEM DAQ system, which is divided into two main parts (see Figure 3.1), the front-end (on-detector) and back-end (off-detector) electronics, is responsible for transmitting the information of muon detections to the central CMS DAQ.

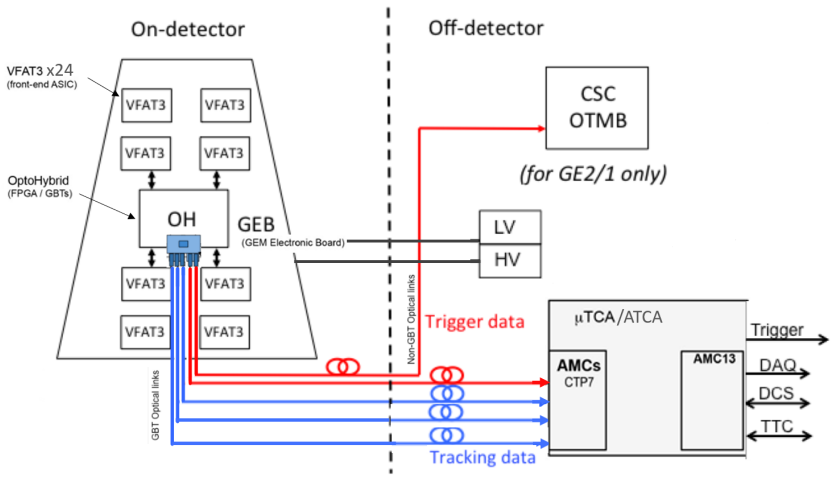

Figure 3.1: Overall schema showing main components and communication paths of the GEM DAQ systems. Taken and modified from [40].

This chapter will attempt to illustrate the DAQ architecture for GEM detectors in CMS, with a particular focus on the VFAT ASIC. It serves as a complex and multichannel high-radiation-hardening chip responsible for connecting the strips of the chamber and digitizing the signals. Furthermore, a dedicated section will describe

the calibration and scans performed to assess the detector's functionality and performance. Additionally, it will highlight my contributions to the DAQ software made during my master's internship at CERN's GEM laboratory in Switzerland.

3.1 Front-end electronic

The front-end electronics is located near the detectors and therefore it is exposed to high radiation doses, so its components usually have protection against high radiation to ensure its correct operation in a CMS environment. Leading this system, it is possible to find the VFAT, because it is the digitizing device that transforms the muon analog signals coming from strips. The rest of the components focus on control and readout VFATs. Data outing from them is routed to the OptoHybrid (OH) through the GEM electronic board (GEB) where all components are plugged in. OH target is an FPGA-based (except for ME0) device which acts as a concentrator board and communication relay for the VFATs. Finally, all communication with the Off detector system is performed through the GigaBit Transceiver (GBT) chipset and the Versatile Link installed on the OH.[41]

Let us explore some important details about the mentioned on-detector electronics beginning from the VFAT.

3.1.1 VFAT ASIC

The VFAT3 ASIC, optimized for use with gaseous detectors in the GEM project, is a specialized chip that digitizes analog signals to provide fast trigger and tracking data. It sends trigger data at the LHC clock frequency (40 MHz) over a fixed latency path and tracking data over a variable latency path. Its logic diagram is depicted in Figure 3.2. The chip comprises an analog stage (per channel), which amplifies, shapes, and digitizes signals from GEM strips, and a digital stage that handles slow control, fast control, and data readout. It is worth noting that VFAT2, which was successfully used in other GEM detectors at the TOTEM experiment, served as the predecessor to VFAT3. [41]

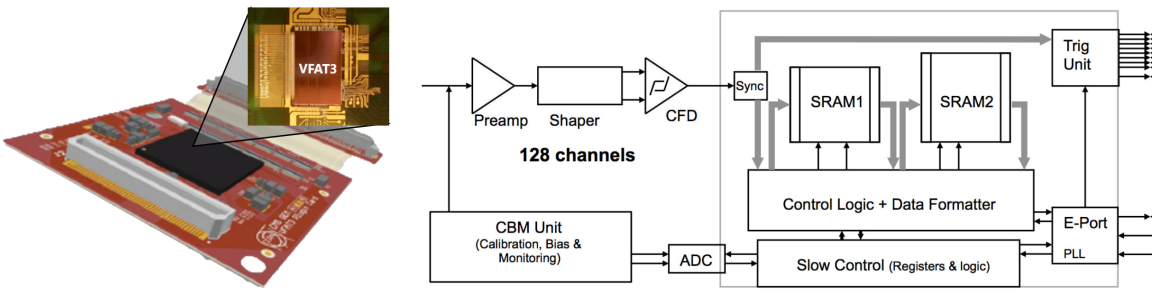

Figure 3.2: Left: Illustration of the latest design of the VFAT3 plugin card, featuring a rigid + flexible PCB configuration. Right: Schematic diagram depicting the internal composition of the VFAT3. Taken from [40, 42].

As was mentioned in the previous chapter, the charge arriving (which can be seen in Figure 2.16) can be in the order of tens of femto coulombs ($\sim 10^{-15}$ C) and exhibit randomness in the signal shape due to statistical fluctuations in production and diffusion, as well as signal time. Therefore, The firmware design of the VFAT3 ASIC was created with a high degree of flexibility to set shaping times and gains according to the detector specifications. Then, changing the shaping time, for example, it is possible to prior time response or full integration of the charge, which could result in a different signal-to-noise ratio. [40, 41]

This ASIC was developed using TSMC-130 nm CMOS technology, and it features 128 channels simultaneously capturing the charge from the GEM detector strips. The analog treatment of the VFAT3 signal occurs in each channel independently, and it involves the following steps: a pre-amplifier stage that transforms the charge pulse from the detector into a high-gain voltage pulse (see Figure 3.3.*a*); a shaper stage that softens the signal and offers adjustable shaping times (see Figure 3.3.*b*); and a Constant Fraction Discriminator stage, which produces an amplitude-independent digital pulse (see Figure 3.3.*c*). A single-to-differential stage is also embedded in the shaper stage, which helps with noise reduction and serves as an interface to the next step, producing a differential signal. The last component is crucial to the VFAT3 because, unlike traditional comparators, it allows for the arrival time of a signal independent of the desired threshold (see Figure 3.4).

The VFAT3 Constant Fraction Discriminator (CFD) can be configured to work in normal mode (Arming or leading edge mode) or CFD mode (full charge mode). The former follows the usual behavior of a simple comparator according to an 8-bit threshold value ($V_{\text{TH\_ARM}}$) and is used when the fastest shaping time is needed [44]. However, this type of comparator mode suffers from the common issue of producing a digital pulse with timing dependent on the threshold value. Figure 3.4.*a* shows a simple simulation that I conducted in Python to illustrate the behavior where the mentioned shift can be observed.

The other mode allows for the integration of all the GEM signal charges, maximizing the signal-to-noise ratio [44]. This also avoids the digital signal time problem by performing a set of transformations to produce a digital pulse that crosses the zero level at a time that closely coincides with the defined threshold level for the original signal. This idea was also simulated and is shown in Figure 3.4.*b*. The working principle is based on detecting the zero-crossing (ZC) of the bipolar pulse obtained by subtracting a fraction of the input signal from a delayed version of the original one [40].

On-chip calibration, bias, and monitoring block (CMB) is embedded in the VFAT3 (see Figure 3.2). It is responsible for the high programmability of the analog channel. The calibration part of this block is used, for example, to produce "calibration pulses" directly to the different channels. That pulse can be generated in either "Voltage Pulse" mode or "Current Pulse" mode. The bias block is added to compensate for physical device variations due to temperature and radiation fluctuations. It consists of several 6 and 8 bits DACs, providing voltage and current references to

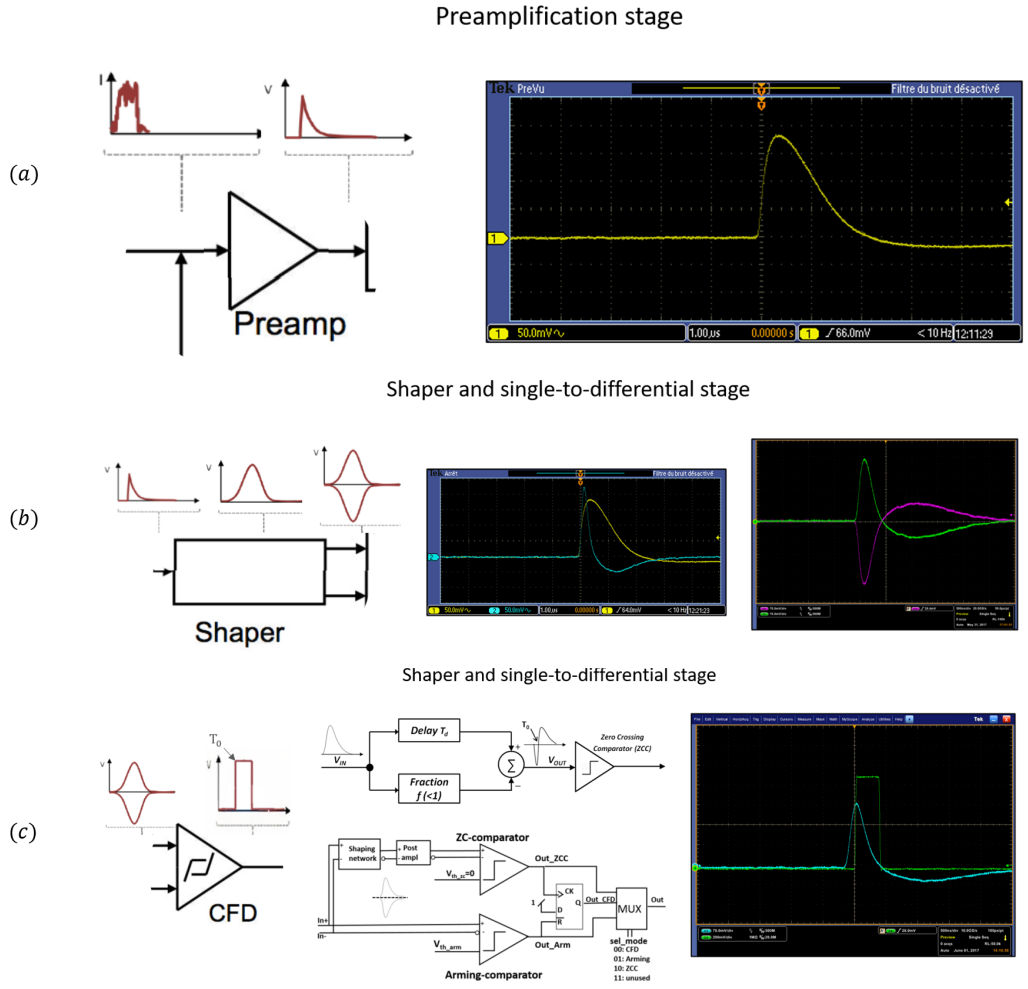

Figure 3.3: (a) A schematic representation of the pre-amplifier stage and an example of the signal response to a calibration pulse. (b) A schematic representation of the shaper-single to differential stage, along with an example of the signal response to the out pre-amplifier signal pulse. (c) A schematic representation of the CFD stage, along with an illustration of the electronic process and an example of the resulting signal from the CFD operation. Taken from [40, 43]

achieve the expected analog response. Finally, for monitoring and adjustment of the programmable parameters, a monitoring block based on 10-bit SAR ADC modules[a] is used. In particular, for VFAT3, two instances of the same ADC are implemented, ADC0 and ADC1. The former uses an internal reference derived from the bandgap, while ADC1 has an external reference of digital power rails. [40]

The already digitized comparator output signals are directed through a synchronization block (see Figure 3.5) that transforms the asynchronous signals according to the 40 MHz LHC clock and carries them through two lines: the trigger path and the tracking path. Synchronization of the signals is possible thanks to a clocked monostable that also allows masking channels and stretching tracking path signals between

[a]SAR architecture for the ADC was chosen because of power consumption when resting

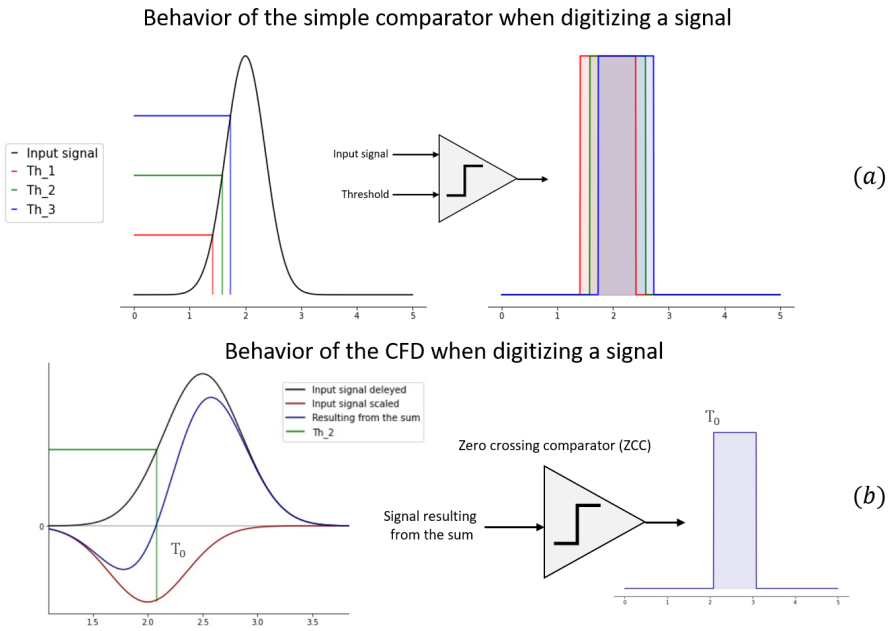

Figure 3.4: Simulations of a comparator's behavior: (a) a typical comparator and (b) a CFD-type comparator.

1 and 8 clock cycles according to a programmable register [40, 44, 45]. In the trigger path, the 128 synchronous signals are reduced to 64 with fast OR operations between adjacent channels, and they enter directly into 8-bit asynchronous counters. Due to its path being a 9 lines bus (SLVS - Scalable Low-Voltage Signaling), it is necessary to include a programmable channel selector logic block that sends 8 channel sectors per time to the trigger unit at a speed of 320 MHz. The last results in the desired rebuilt 64-count package at the precise rate of 40 MHz to finally be sent out of the detector by the trigger line. The ninth trigger path line works such as a start of frame pulse. [44]

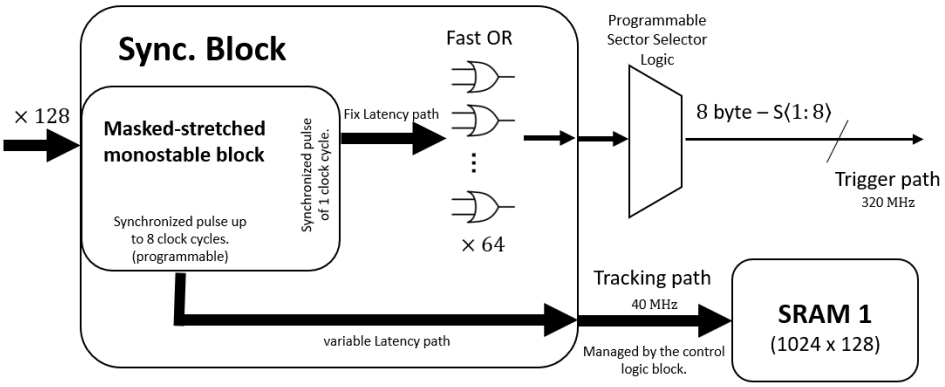

Figure 3.5: Schematic representation of the VFAT synchronization block.

The output signal going through the tracking path (128 bits) is directed by the control logic part of the control logic + data formatter block (see Figure 3.2) to the first of two SRAM memories (SRAM1). It has a depth of 1024, allowing us to store up to 25.6 μs of history until a first-level trigger (LV1A) event identifier is received[b]. When this happens, the triggered events are moved to the second SRAM of 512 depth (SRAM2) after being formatted with an associated header, a bunch crossing (BC) and event (EC) counter time tag, a data field, and a CRC code to ensure packet integrity. The data packet content is highly configurable. It is possible to take out data in a compressed or uncompressed state, using some configurable characteristics such as zero suppression to reduce the data packet size, and hence, to allow trigger rates to go much higher [44].

The last key component to mention here is the VFAT3 communication port (V3CP) which is an SLVS bi-directional port that operates at 320 MHz. It was designed to be compatible with the CERN GBT and lpGBT ASICs (Which will be contextualized later). V3CP is the bridge that connects the VFAT3 with the on-detector electronics by managing VFAT3 fast and bi-directional slow control commands [40, 44].

The fast serial codes managed by the V3CP are 8-bit commands sent through differential e-links at 320 MHz which control the chip at the frequency of 40MHz. They are used to send synchronization, trigger, and several internal counters reset instructions. they control the operation of tracking data paths with extremely low latency using commands such as " LV1A" (to send the trigger request) or "Calpulse" (to inject the internal calibration pulses into the selected channels)(see the commands Table 3.1). [40, 41]

FAST COMMAND	**8-BIT REPRESENTATION**	**FUNCTION**
EC0	0000 1111	*Reset of Event Counter (EC)*
BC0	0011 0011	*Reset of Bunch-crossing Counter (BC)*
CalPulse	0011 1100	*Injection of calibration pulse*
ReSync	0101 0101	*Reset all VFAT3 state machines*
SCOnly	0101 1010	*Force "Slow control Only" Mode*
RunMode	0110 0110	*Return from "Slow control Only" Mode*
LV1A	0110 1001	*First level trigger*
ReSC	1010 0101	*Reset of Slow Control*
LV1A + EC0	1010 1010	*First Level Trigger and reset of the EC*
LV1A + BC0	1100 0011	*First Level Trigger and reset of the BC*
LV1A + EC0 + BC0	1100 1100	*First Level Trigger and reset of the EC and the BC*
EC0 + BC0	1111 0000	*Reset of EC and BC*
CC-A	0001 0111	*Sync character, need to send 3 consecutive for sync*
CC-B	1110 1000	*Sync verify character*
F1	0111 1110	*IDLE character 1*
F2	1000 0001	*IDLE character 2*
SC0	1001 0110	*Sends "0" to the slow control*
SC1	1001 1001	*Sends "1" to the slow control*
SyncAck	0101 1010	*Synchronization Acknowledge*
VerifAck	0110 0110	*Verification Acknowledge*

Table 3.1: List of the Fast Synchronous Control Commands (FSCCs). [40]

[b]VFAT3 also has a "self-trigger" option that makes it independent from an external trigger.

On the other hand, slow control communication handles the configuration of the internal registers of the VFAT3. These registers define quantities such as the threshold of the analog front-end, the latency, and the readout data format. Together, the V3CP and CBM units enable calibration routines on the chip, which will be discussed further in this chapter. Additionally, data transfer is prioritized through two fast control commands, "SC0" and "SC1" that send "1" or "0" respectively. [40, 41]

3.1.2 The OptoHybrid

Based on a Xilinx Virtex-6 FPGA (except for ME0 which does not integrate FPGA technology), the OptoHybrid serves as an interface between the VFAT3 ASICs and the off-detector system. It is mounted on the GEB and includes circuits dedicated to operating the optical links. Configuration of the front-end chips and tracking data transmission for the VFAT3s are carried out directly through three bi-directional links, the radiation-hard Gigabit Transceiver - GBT (low power - LpGBT in the case of GE2/1 and ME0) chipsets installed on the OptoHybrid using GBT protocols (see Figure 3.6). Each GBT chipset can handle one column of eight VFAT3s. relies on radiation-hard optical transceiver modules from the Versatile Link project of CMS, called VTTx (transmitter) and VTRx (receiver) devices.

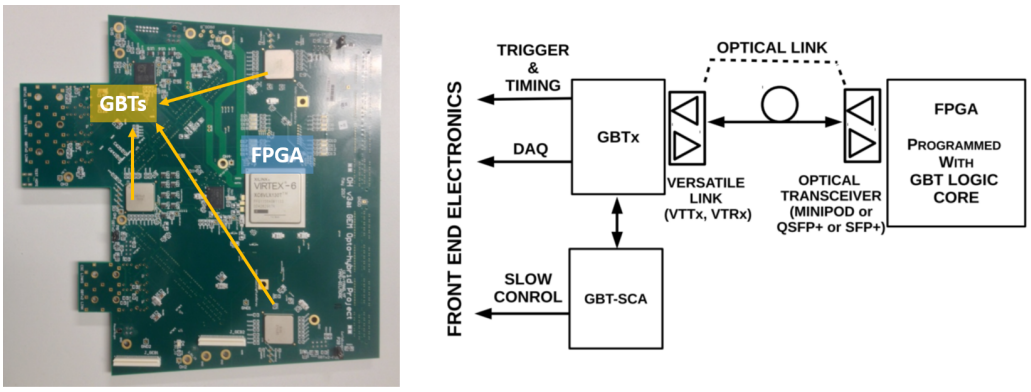

Figure 3.6: Left: A photograph of the GE1/1 OH board indicating the location of the FPGA and GBT chips. Right: A schematic representation of an LHC detector electronics system that employs GBT chipset and a Versatile link component, adapted from [40].

In this system, the use of an FPGA instead of the simple standard GBT data flow aims to improve the efficiency of the existing CSC trigger subsystem at Level-1. This is necessary because the existing optical fibers to the CSC TMB cannot handle the GBT transmission protocol. As a result, trigger information is transmitted and split into two separate optical links, directly through the FPGA, using a VTTx device to connect to both the CSC trigger processor and the GEM trigger system.[28, 40, 41]

In summary, the OptoHybrid is responsible for performing all the multiplexing, formatting, zero suppression, and data transmission to CSC and μTCA back-end electronics. [40]

The previous discussion provides a comprehensive overview of the front-end components of the GEM DAQ system. Now, let us shift our focus to the back-end part, which encompasses more robust systems designed to control the commissioning and calibration operations of the GEM detectors in CMS.

3.2 Back-end electronic

The GEM back-end electronics provide a fast, low-latency interface between front-end electronics and CMS DAQ, TTC (timing, trigger, and control) systems [40]. It is based on a common CMS Phase-2 platform known as the Advanced Telecommunications Computing Architecture, xTCA (μTCA for GE11 and ATCA for the others). It provides a modular way to build equipment with swappable computing units. For GE1/1, the μ format was adopted, and the principal difference is the form factor for the computing unit connectors. In simple terms, the back-end electronics is a crate that hosts different swappable expansion cards AMCs (Advanced Mezzanine Cards) to give the system its functionalities. These cards are inserted into expansion slots within the chassis to complete the system.

The current detectors (GE1/1 and GE2/1 demonstrator) are mounted with μTCA crate that supports 12 dual-slot AMC and 2 MCH (μTCA Carrier Hub) modules. A carrier hub is a network equipment that acts as a central connection point for various devices. In this case, The first MCH slot (MHC1) houses a commercial module used for standard gigabit ethernet communication and Intelligent Platform Management Interface (IPMI) control. The second (MCH2) slot contains a custom AMC13 board, which is a standard module in CMS that interfaces μTCA crates to the CMS data acquisition system and also provides the CMS trigger Timing and Control (TTC) signals downlink. [40, 41]

The AMC used[c] for GE1/1 is the CTP7, a board developed by the University of Wisconsin. It is equipped with a large Virtex-7 FPGA, providing extensive computational power, along with a Zynq FPGA, capable of running a Linux operating system for monitoring. This card serves as the interface with the on-detector electronics of six GEM chambers using 48 optical links. Specifically, six are required to connect with the three GBTs of each OptoHybrid in the chamber to obtain tracking data (three for transmission and three for reception). This amounts to 36 optical links for the three GEM detectors. Additionally, two optical links per OH are needed for the trigger paths, resulting in a total of 12 optical links for the three superchambers. Therefore, a total of six CTP7s are necessary per endcap for the GE1/1 detectors (see Figure 3.7. The CTP7 board plays three primary roles: handling slow control requests for the subsystems, interpreting TTC (Timing, Trigger, and Control) signals, and reading out the trigger and tracking data from the OptoHybrids.[40, 41]

A more comprehensive discussion about the GEM DAQ electronics can be found in [40]. However, with this concise understanding of the electronic system, it is now time

[c]For GE2/1 and ME0 a board known as X20 is planned to be used.

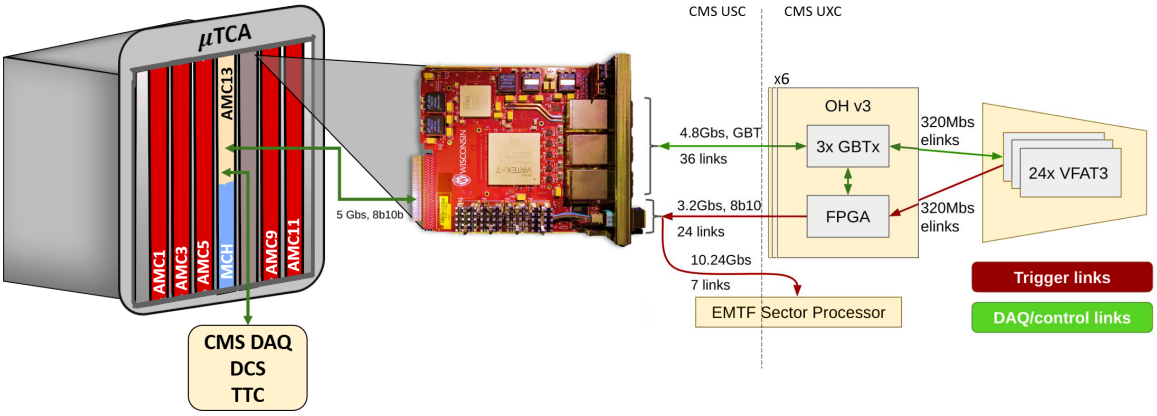

Figure 3.7: Illustration of the GEM back-end electronic architecture. USC and USX refer to the User Service Cavern and User Experimental Cavern, respectively. Based on descriptions of [40, 41, 44, 46]

to delve into the software that facilitates the manipulation and control of the GEM detectors in CMS. The next section will introduce the firmware and software currently utilized by the GEM collaboration to control the system. Special emphasis will be placed on some scans, calibration procedures, and data analysis just to introduce those that were my personal contributions to the DAQ software team.

3.3 DAQ firmware and software

The GBT-based bi-directional links allow the control of on-chamber electronics, including VFAT3 ASICs. Therefore, on one side, the xTCA firmware is focused on transmitting fast commands, slow control, calibration routines, and trigger and tracking data acquisition to the VFAT3s. On the other side, the DAQ software establishes a high-level interface for the common operations of P5[d] and test stands. [28]

The last firmware version is hosted on CERN GitLab (gitlab.cern.ch/emu/0xbefe) with open access for collaborators. It uses a firmware build system called Hog, developed by ATLAS and is highly portable, with most of the code being board/technology agnostic. A thin board-dependent layer is used as an adapter to map I/Os, clocks, and implement slow control. Currently, four different backend boards are supported[e], and the same code is planned to be used for all three GEM stations. Common code is also used in both CSC and GEM. [46]

The firmware repository includes a Python-based software suite that is intended for use in small-scale lab systems. The software suite is easy to develop on, requiring only a single function call to write/read any register. Some of the included applications are: scripts to program the FPGA, initialize and configure the backend and frontend, an interactive shell to manipulate registers, and a text-based user interface

[d]Remember that this is the position on the LHC ring of CMS experiment.
[e]X2O VU13P, X2O KU15P, CTP7, CVP13.

that provides overall status and the ability to configure/start/stop a DAQ run. Additionally, there are numerous scripts that implement specific functionalities, such as optics diagnostic monitoring, automated GEM frontend production tests, GBT and SCA chips control, phase scans, temperature monitoring, PROMless feature tests, GEM S-Curve scans, and data format checker. [46]

The P5 and test stand at CERN use GEM online software, which is also hosted on CERN GitLab (gitlab.cern.ch/cmsgemonline). This software provides complete control, diagnostic facilities, and analysis tools for common development, testing, and commissioning operations. This is particularly interesting for this research project because one of the contributions that could be achieved was the development of some of the routine analyses for the diagnostics and characterization of detectors. Therefore, before moving on to the next chapter where production issues will be discussed, let us describe the analyses that we can implement, emphasizing those to which I contributed.

3.4 Calibration, testing and data analysis

To ensure the desired performance and efficiency of the GEM detectors during commissioning periods, it is crucial to have accurate electronic characterization, with a particular emphasis on VFAT3 and OptoHybrid. While the characterization process primarily takes place during the production stage, relevant analyses are also carried out during intermediate periods of CMS RUNs to monitor performance and identify possible failures online. Several test scans, calibrations, and analysis procedures are continually performed, some of them, by injecting calibration pulses, and optimizing the parameters to achieve uniformity over the entire detector. That could be accomplished using firmware and software tools. This section aims to highlight some relevant scans and analyses, with a focus on two in particular: threshold scan analysis and s-curves scan analysis. These two analyses are personal contributions that were achieved during this research work and were already included in cmsgemos-analysis, a subgroup of the DAQ online software suite mentioned earlier.

Just to clarify the notation, have in mind that each VFAT3 has a unique Chip ID, but it is sometimes also identified by its relative position on the CMS detector with a mapping notation that has the form “fed xxxx- slot xx- oh xx – vfat xx”, and comprises four pieces of information: “Fed” refers to the VFAT’s endcap position, such as 1467 for GE11 minus endcap. “Slot” indicates which AMC module the VFAT is connected to (which CTP7), while “Oh” specifies the OptoHybrid. Finally, the last number is the VFAT’s identification number on the GEM board.

3.4.1 Characterization procedures

ADC and DAC scans

These scans read out the currents and voltages produced by the VFAT to bias its analog front-end. When writing values into registers to define the threshold and other

parameters, a conversion to an analog value is performed inside the chip. Due to the high sensitivity of the analog circuits, this conversion will vary from component to component, so it is essential to record the results of each chip. In order to access the analog signals inside the VFAT, two analog signals (one for the voltage reference and one for the current reference) are sent out through the GEB and transmitted to the OptoHybrid, which uses the already mentioned ADC0-ADC1 to digitize the information. The embedded monitoring system offers the possibility to convert voltages to ADC counts with a resolution of 10 bits over 1 V, resulting in a precision of 977 μV. It is vital to establish the correct values for each chip since they power the front-end and are used to define the length of the tail of the signal shape, the rise time of the distribution, etc. [41]

The DAC scans create a correlation link of every value in the VFAT registers with its corresponding ADC counts, and thus, voltage or current. Figure 3.8 shows an example output for DAC 2 of the constant fraction discriminator (CFD), it is, DAC register value vs. ADC0 bias current. [41, 47]

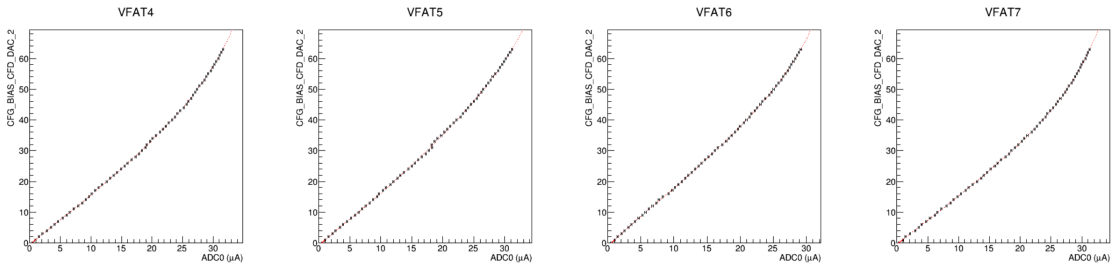

Figure 3.8: Example of a DAC scan plot produced, taken from [47].

Those procedures result in the creation of configuration files containing the relevant parameters. Accessible from a CMS-Hosted database during the tuning process for commissioning. These calibration files include parameters such as: [41]

- Reference current (IREF) values for the digital-to-analog (DAC) converter after the bandgap circuit in the CBM unit, used to generate reference currents for all programmable DACs.
- Analog-to-digital (ADC) reference values for ADC0 and ADC1 in the CBM unit, used to monitor all references.
- DAC calibration values, cal-DAC, used for calibrating the calibration pulse circuit.

Last parameter provides information on how to convert DAC unit readings to amounts of charges (fC), as illustrated in Figure 3.9 (left) which shows this relation for a particular VFAT. [41]

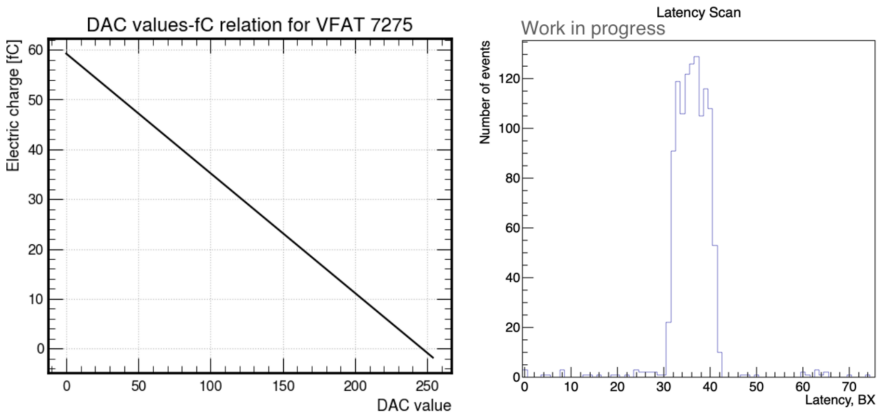

Figure 3.9: Left: Linear relation of the charge values and the DAC Values for fed 1467 - slot 1 - oh 2 - vfat 3. Right: Graph that illustrates the latency scan results. Taken from [47].

3.4.2 Calibration procedures

The calibration routines involve data-taking procedures that are subsequently analyzed to establish relevant parameters used for commissioning or revealing information about the detector's performance. Each of the aforementioned scans exists in two versions: one for performing scans on a single VFAT in production stages and another for conducting scans on multiple chips simultaneously during commissioning stages.

Latency scan

The purpose of this procedure is to find the optimal latency value for a VFAT, which is the time difference between the arrival of an LV1A signal and the storage of the related event in the VFAT buffer. That is an important parameter to determine since the changes in the length of the fibers that transmit the L1A trigger signals between chambers are not negligible. This process is carried out during particle beam operation. In a latency scan, trigger signals are sent to the chamber and the total number of hits for each latency value is recorded. An ideal latency scan should reveal that if the VFAT is noiseless and has 100% detection efficiency, the hit ratio would be 0% outside the correct latency window and 100% inside it. An example of how the plot scans look is shown in figure 3.9 (Right). [41, 47]

Threshold scan

This scan measures channel noise as a function of the VFAT threshold. The number of events with hits is recorded for each threshold value set on the VFAT when no radiation source is present. Essentially, the scan shows how noise decreases as the threshold increases, allowing the determination of the point at which the system can operate with minimal noise. This scan is one of the first steps in qualifying the electronics as it reveals non-responding or noisy components. Figure 3.10 illustrates the evolution of noise levels as a function of the threshold. [41]

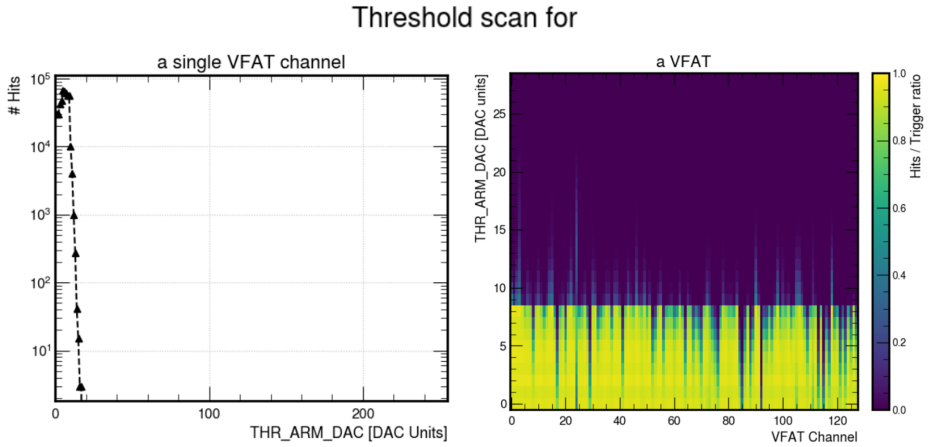

Figure 3.10: Example of data resulting from threshold scans. Left: graph showing results for fed 1467 - slot 3 - oh 9 - vfat 3 - ch 51. Right: map showing how the results for each channel in a VFAT looks like, the particular map is for the channels of the same VFAT (1467, 3, 9, 3).

S-curve scan

An S-curve measurement involves injecting a calibration pulse into a VFAT channel[f] and recording the response of the voltage comparator at a specified threshold. This method is used to measure the equivalent noise charge (ENC) present in the detector's preamplifier/amplifier combination. In an ideal scenario, the voltage comparator should only respond when the injected charge exceeds the threshold, resulting in a step function. However, due to noise, the actual response of the comparator generates an S-shaped curve, giving it its name. Figure 3.11 illustrates this phenomenon. The S-curve can be fitted to an error function, and two parameters can be obtained that represent the detection and noise level of the S-curve for each VFAT channel. However, further details on the analysis will be presented later.

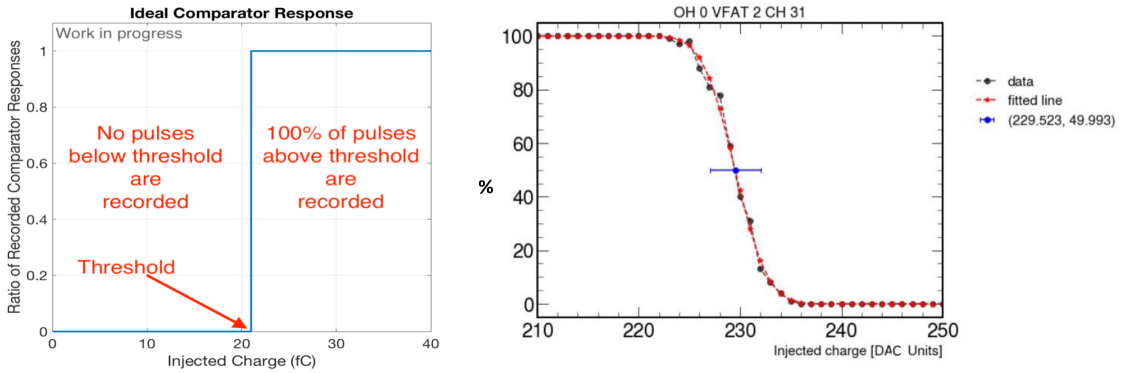

Figure 3.11: (Left) Representation of the ideal scan result, taken from [47]. (Right) An example of a real S-shaped line. It should be noted that the difference in orientation is due to the units used to produce the plots.

[f]This can be done by sending the command "CalPulse", as shown in the commands table 3.1.

3.5 Analyses procedures

Data resulting from previous calibrations scans are analyzed with the different tools available in cmsgemeos-analysis[g] suite. The following section will describe in more detail the two of the analysis software I contributed to.

3.5.1 Threshold scan analysis

Data from threshold scans, apart from establishing threshold values, is instrumental in identifying non-responsive or noisy channels in various VFATs. The concept is simple: utilize the data to categorize a channel as either broken (unable to detect), not fully working (exhibiting anomalous detection behavior), or not readout (inactive since before).

Identifying a broken or masked channel from the data is a relatively straightforward process. A broken channel is typically an isolated case. If there is another channel in the same VFAT with signs of having a non-empty entry, then the anomalous channel should be identified as broken. In contrast, for the masked channels, it implies that all channels in the VFAT are turned off, resulting in every VFAT channel being labeled as not readout. This distinction arises because the not readout channels are expected to correspond to sectors that were intentionally inactive for reasons determined by the commissioning or technical team. Conversely, a broken channel is an anomaly that arises channel by channel during operation. Figure 3.12 illustrates a schematic representation of potential problematic channels in a chamber. On the right side of Figure 3.10, the 2D map of a VFAT data is presented, allowing for straightforward visual identification of non-responsive channels through the use of threshold scan data.

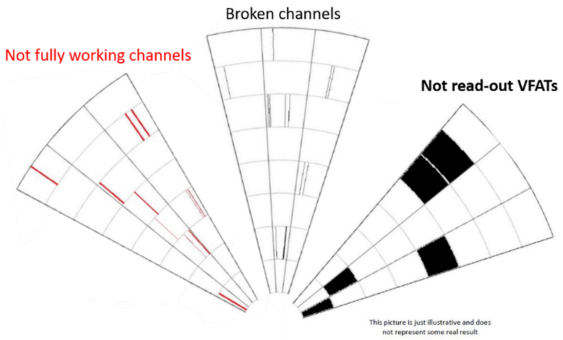

Figure 3.12: schematic representation of the channel classification.

From the previous description, it is easy to see that a simple algorithm that performs the steps shown in the flow diagram of 3.13 will classify the masked VFAT channels correctly. The basic idea is to consider that if a VFAT is masked, none of its entries will be different from zero. As shown in the diagram, this analysis step is performed in parallel for all VFATs, which means 24 VFATs by 12 OHs by 6 slots (CTP7) by 2 endcaps in the case of GE1/1 rings. The same approach can be followed to classify broken channels. However, in this case, after filtering out the previously masked channels, the same algorithm is applied but grouping data by channels instead of VFAT.

[g] gitlab.cern.ch/cmsgemonline/gem-daq/cmsgemos-analysis.

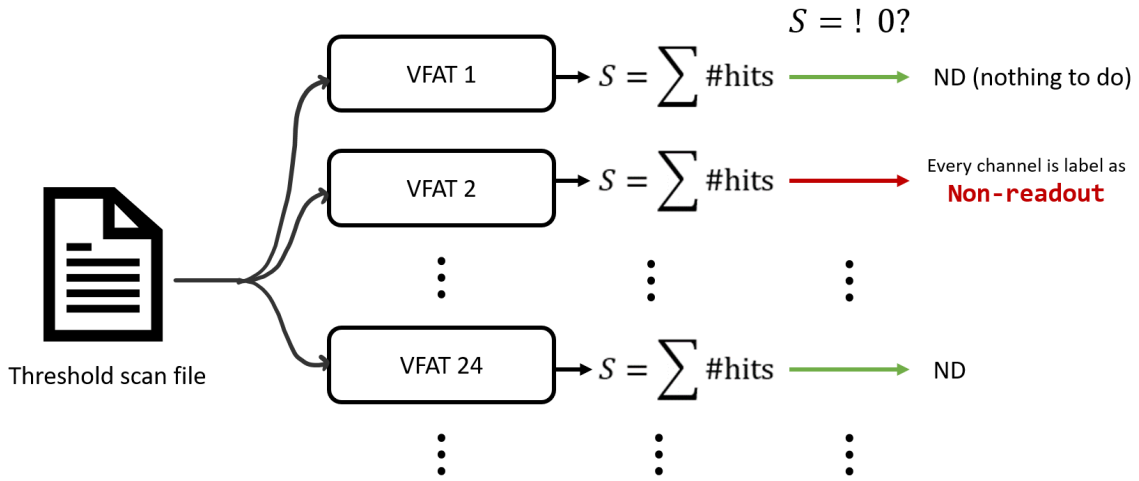

Figure 3.13: Flow diagram of the designed algorithm to perform the threshold scan analysis.

On the other hand, the case of not-fully working channels is more complex, because, after several in-depth studies, we have not been able to find a single criterion that allows us to label such channels as anomalous. Figure 3.14 shows two cases in which the behavior of hit data is markedly different. While in the first case, a direct inspection of the values can identify the anomalous channel (around 55-60) which has significantly fewer hits than the others, in the other cases, there is no uniform behavior that makes it easy to establish a criterion.

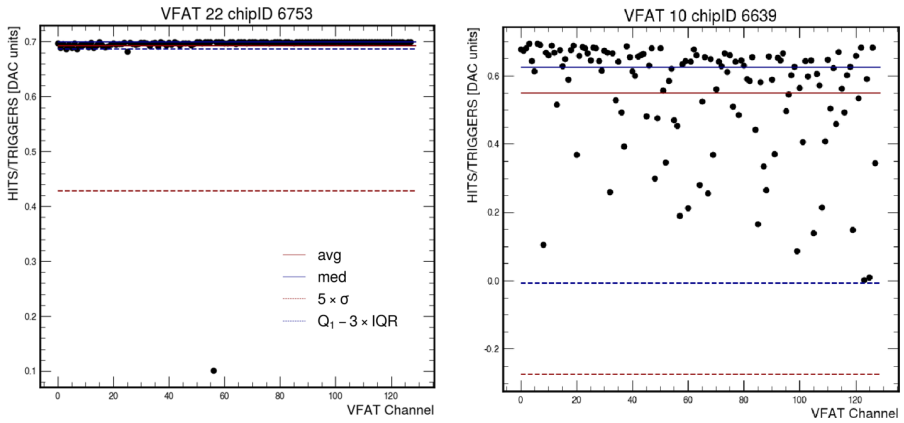

Figure 3.14: Plots of the hist data dispersion over VFAT's channels.

Other approaches were attempted, where the data were grouped and compared with its average behavior. For instance, Figure 3.15.a illustrates that the data has a pronounced increasing trend as the η-partition position increases. This suggests that it would be appropriate to identify which channels are anomalous by comparing them with the expected behavior of an average η-group. Unfortunately, a thorough inspection revealed that while some channels clearly needed to be labeled as anomalous (Figure 3.15.b), some others actually followed the expected trend but with more

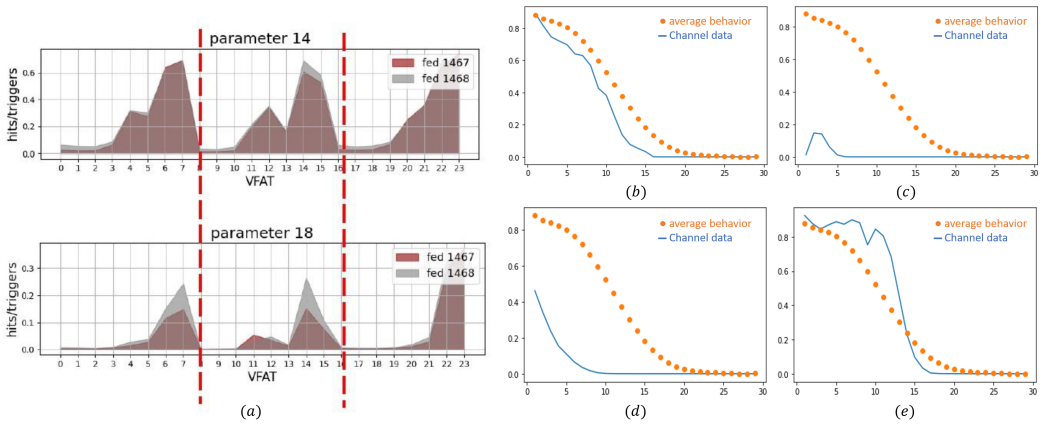

Figure 3.15: (a) Trend of the hits data averaged over all the detectors grouped by VFAT. It shows that the general hits behavior is η-partition dependent. The parameter refers to a parameterization of the threshold applied. (b-e) Comparison of the hits behavior of a single channel with the expected averaged behavior.

attenuation compared to others (Figure 3.15.d), possibly due to intentional changes in the VFAT shaping parameters or external factors such as their position in the CMS detector infrastructure. Therefore, it was not possible to define a single criteria for this case. In the end, it was decided to focus on the previously mentioned classifications and not pursue this one further.

The current version of this code can be found in the gemos-analysis suite as threshold_scan_analysis.py, and addition to give the analysis result in a file, it produces plots like the map of the left in Figure 3.16.

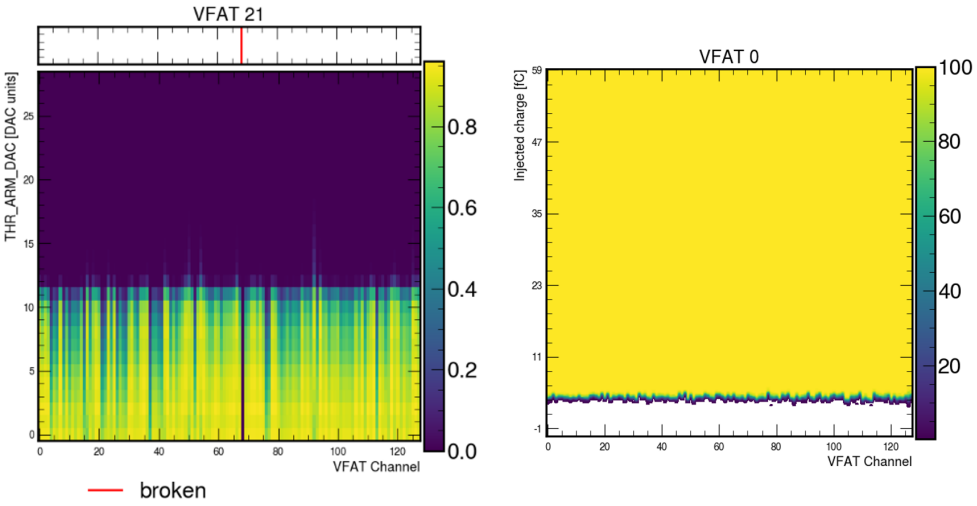

Figure 3.16: Summary 2D plots resulting from the analysis codes: (Left) for Threshold scan analysis, and (Right) for S-curve scan analysis.

3.5.2 S-curve scan analysis

As explained before, the effective noise channel and activation threshold can be obtained through a fit to the scan data. The function to fit has the form:

$$f(x) = A + A * \text{erf}\left(\frac{\pm(x-\mu)}{\sigma\sqrt{2}}\right), \tag{3.1}$$

where A would be equal to 0.5 if the data is normalized, and the sign of the argument of the error function depends on whether the analysis is performed with data in DAC units or fC.

The algorithm designed to perform the analysis is shown in Figure 3.17. A critical aspect of this procedure is the need to perform it as fast and efficiently as possible since this test is planned to be used both in P5 commissioning operations and in production stages, where time needs to be minimized. Therefore, it is noticeable that for this case, a software parallelization over VFAT was implemented. As one of the final outputs, the code provides summary plots, such as the one shown on the right in Figure 3.16. Additionally, the implemented code is also able to produce plots that display statistical information about the results. Figure 3.18 displays a plot of the dispersion of values obtained for the channels in a VFAT, including the histogram distribution on the right. Furthermore, Figure 3.19 shows the boxplots that comprise the statistics of the results for a single OH grouped by VFATs.

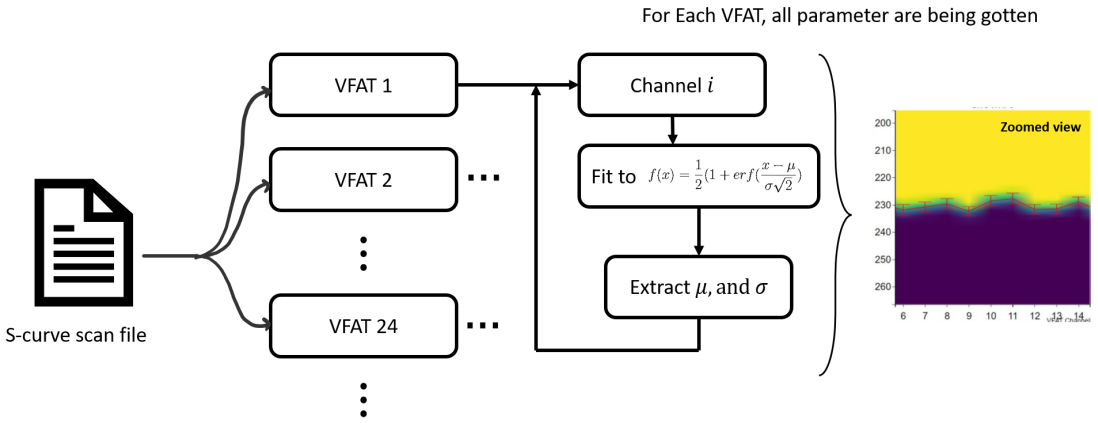

Figure 3.17: Flow diagram of the designed algorithm to perform the s-curve scan analysis.

It is clear that there exists a bias in the effective values that is not constant across the chip. In the case of the threshold, [41] mentions that the resulting information from this scan analysis is used to eliminate this effect. It is possible to equalize the response of the front-end by using channel-by-channel programmable registers that slightly adjust the threshold value. This allows for scans such as the one shown in Figure 3.20 (left) to be transformed into scans like the one on the right. However, this procedure does not affect the slope of the response curve and thus the noise parameter, since it is intrinsic to the VFAT and cannot be changed. [41]

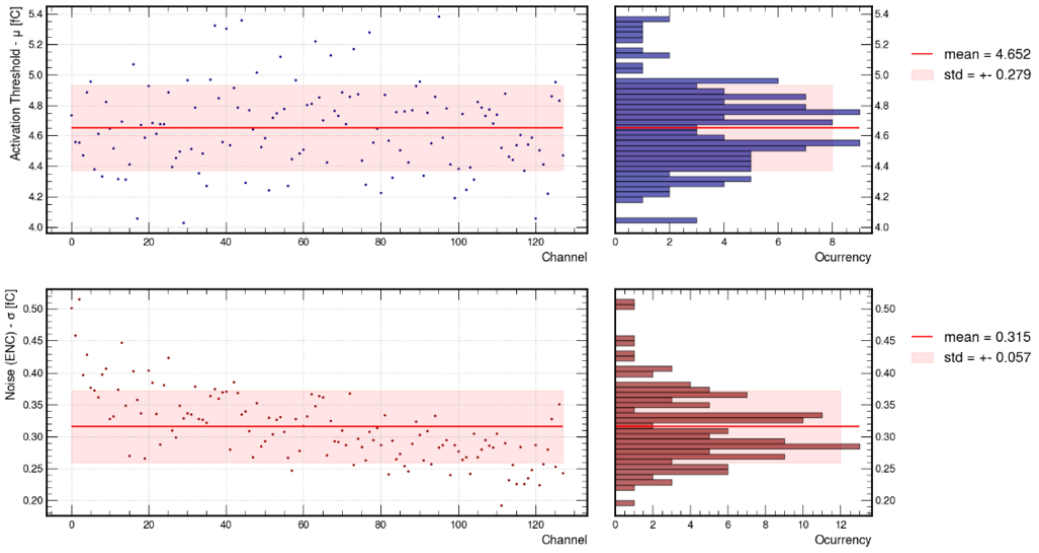

Figure 3.18: Dispersion of s-curve analysis results for fed1468-slot3-oh9-vfat8.

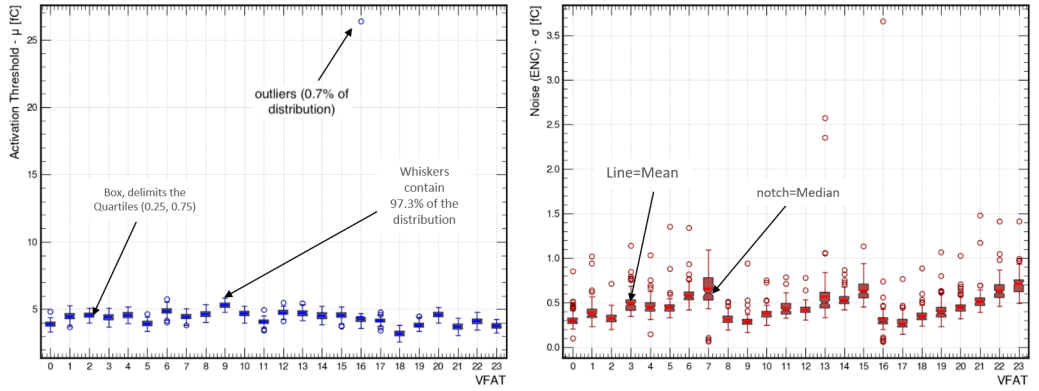

Figure 3.19: Boxplots showing the statistical information of the result for an OH (fed1468-slot3-oh9), grouped by VFAT.

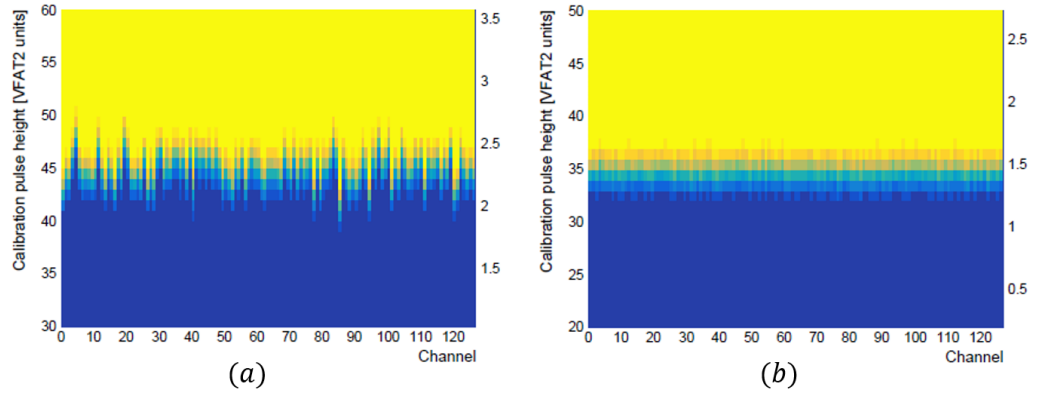

Figure 3.20: Illustration of the change in data after the equalization process mentioned in [41].

Up to this point, previous chapters have offered a comprehensive overview of the GEM detector in CMS, covering its operational principles and integration within the CMS experiment. This provides a deep understanding of the GEM project. Now, to complete the overall picture, it is crucial to delve into some critical aspects of massive assembly procedures and quality control operations, which, as mentioned from the beginning, are vital for the success of the GEM project. The next chapter will also present an opportunity to introduce my role within the collaboration in that context during the three-month internship at the GEM labs in CERN I undertook. It will focus on the assembly and tune-up processes of a GEM detector, highlighting my personal contributions, especially in the 6th stage of the quality control process.

Chapter 4

GE2/1 production

This chapter corresponds to a brief overview of the production operations. It will try to cover the main aspects of massive production and quality control processes (QC) crossing more detailed aspects related to the triple GEM foil stack assembly and quality control processes. This part of the research work aims to provide a better understanding of how the detectors are built and tested. That could give basic capabilities to identify any critical point along the production chain that could affect the desired performance of the detectors.

First of all, let us have in mind that massive production is an operation organized in a centralized way. The CERN site (France) plays as a concentration and intermediary point between the different involved labs around the world (see Figure 4.1), which are from the United States, Italy, German, Belgium, India, Sri Lanka, China, and South Korea. That being said, this chapter will primarily focus on describing the processes carried out at the CERN site, as these were the ones directly observed and where contributions were made during my research internship. The chapter will present the results of these contributions in terms of detector assembly and quality control tasks.

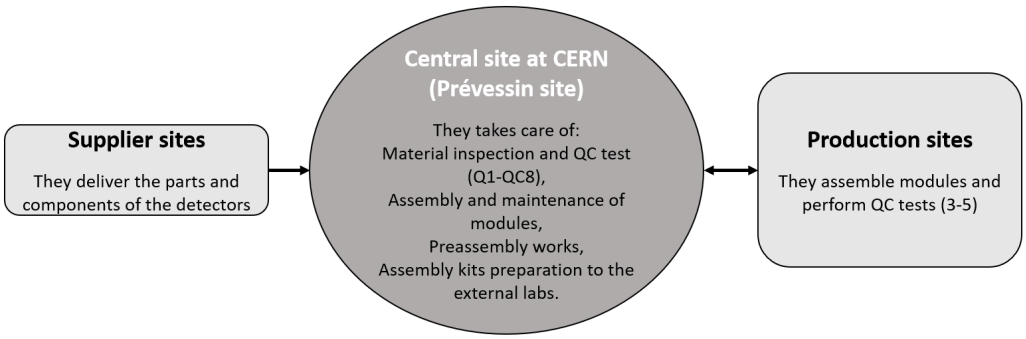

Figure 4.1: Simplified CMS GEM Production Scheme.

4.1 Triple GEM detector assembly

GE2/1 module assembly does not differ too much from the already installed in the first GEM endcap station (GE1/1), for which it already exists a brief descriptive guide in [48]. So, let us start this chapter by covering quickly the steps to get a complete general tripe GEM module trying to mark some improvements or new details with respect to the first GEM generation.

The assembly process is performed in a cleanroom environment (ISO 7/class 10,000 or better), and starts after the second step in the quality control chain QC2 (which will be detailed later in this chapter), where the integrity and good features of the GEM foils was guaranteed. Those foils stay stored in protective hermetic boxes and to assemble a new detector it is necessary just to take the needed amount of foils, in this case, three. To assemble a new detector, only the required number of foils, in this case three, needs to be taken from the storage. Here, the first difference from the GE1/1 assembly process becomes apparent. As mentioned earlier, a GE2/1 detector is not a single chamber but consists of eight modules (M1-M8) due to its larger size. Therefore, it is crucial to carefully verify that the correct foils are selected before starting the assembly process.

The central part of the assembly is the triple GEM arrangement. That is done by putting every foil with a dedicated set of internal frames designed to ensure accurate distances between foils in the configuration 3-1-2-1 millimeters as was mentioned in previous chapters (see Figure 4.2). In this process, the foil type (GEM 1-3) is decided by cutting the appropriate power pad to ensure the correct contact with the powering pin in the drift board (see Figure 4.3). The t-nuts of the stretching system to apply uniform tension along the foil are also placed during the process. Here, another difference with the previous generations of GEM detectors appears. For GE2/1, due to its larger size, extra foil support is added to avoid foil center sagged, a problem detected during efficiency uniformity tests (QC5 - step 2), because the center deformation causes a change in the voltage gaps, therefore, a change in the gain features (see Figure 4.4 left).

Once the foils are attached to the frames, the GEM stack is joined to the Drift board by tightening the screws which connect the drift board pullouts and the already-mentioned t-nuts (see Figure 4.4 right). The foils are stretched until $\sim$ 80 Nm with a pre-configured electronic torque wrench, aiming to remove any possible wave in the foil. Waves in the foil could cause problems in the desired efficiency or could increase the discharge probability. To complete the module assembly process the only missing thing is to add the external frame and the readout board. Fixing these with screws an hermetically enclosed volume is guaranteed and the module is ready to go to the next step, the quality control process. Figure 4.5 shows a final GE2/1 module assembled and a complete summary overview of the mentioned internal structure of it.

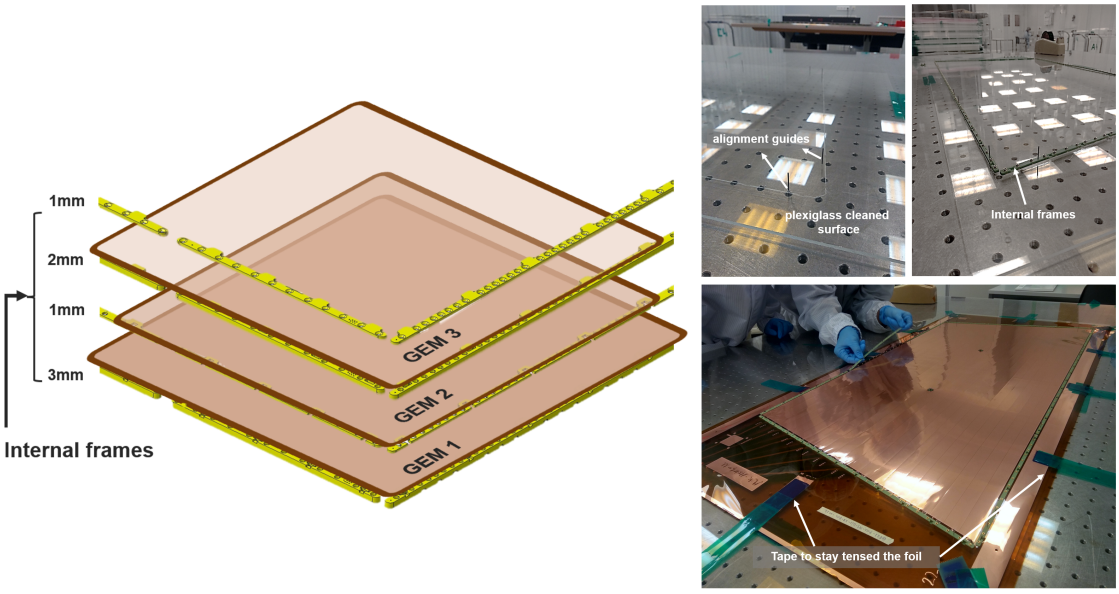

Figure 4.2: Left: Illustration of the GEM foil and internal frame structure. Right: Some pictures of the GEM foils stack assembly process.

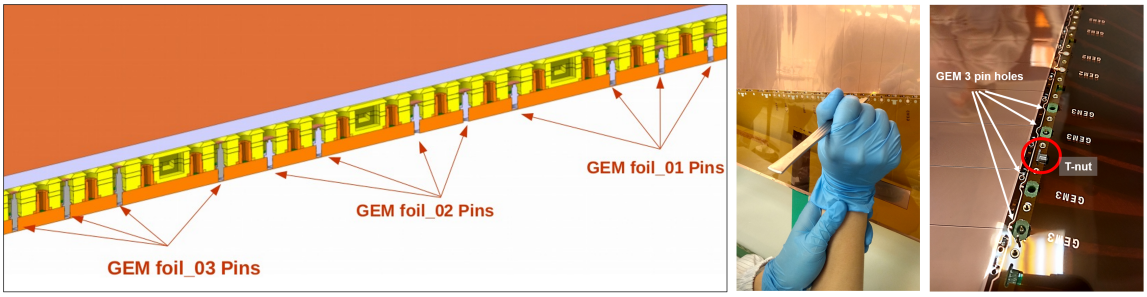

Figure 4.3: Left: Illustration of the distribution of the drift board powering pins, taken from [48]. Right: Pictures of the foil pin holes cutting process and a t-nut placement.

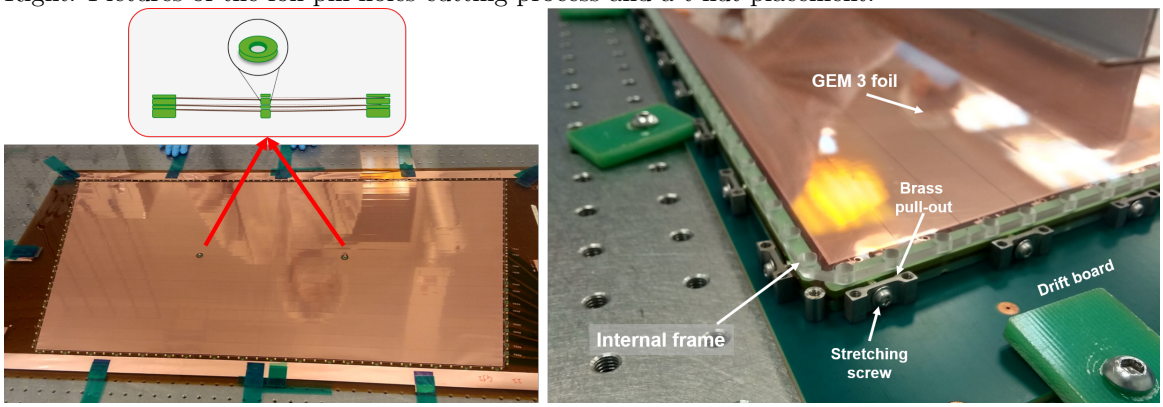

Figure 4.4: Left: Illustration of the central sagged problem and its solution by putting a central support ring. Right: Picture of a completely assembled internal part of a triple GEM detector.

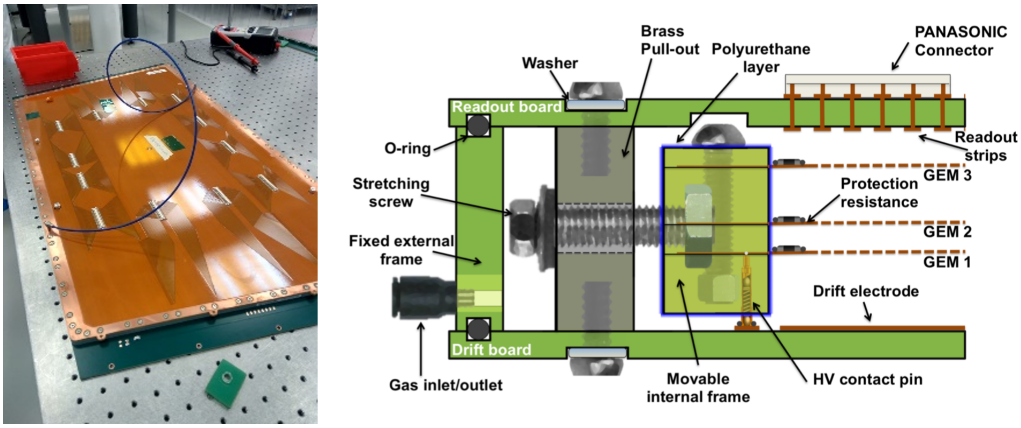

Figure 4.5: Left: Picture of completely assembled GE2/1 module. Right: A summary overview of the mentioned internal structure of GEM module, taken from [48].

4.2 Quality control processes (QC)

As mentioned in previous chapters, the detectors undergo strict quality control consisting of eight steps (QC1-QC8) before installation. These steps involve comprehensive testing of all chamber components to ensure optimal efficiency and address any potential mechanical or electrical issues during CMS RUNs. This section provides detailed insights into these QC steps. Basically, in addition to the assembly process participation, I had the opportunity to actively participate in QC3, QC4, and QC6. Among these, QC6 stands out as the area where I made significant contributions during my time at CERN by implementing improvements in parallelization that enhanced the efficiency of the QC6 process, as will be discussed further.

4.2.1 QC1

This quality control process consists of a number of detailed evaluations of the mechanical parts in order to validate their good quality. This step is crucial to avoid issues during assembly. The mechanical pieces should be almost perfect physically, wrong dimensions, the bad thickness of frames, bad groove depth, wrong Oring diameter, and components showing defects or outside the specifications are discarded from the production materials or returned to the factory for rectification, because that could become, for example, an impossible task for closing the module correctly causing gas leaks, or undesired mechanical stress in other pieces which could break them in the future. [6, 30, 49]

Particular attention is paid to the inspection of the Drift and Readout PCBs, which directly impacts the electric field uniformity, and consequently the overall detector performance. For both, the planarity is measured and boards with deviations from flatness above 3 mm from the center are rejected. In the case of the Readout board, an electrical test is performed to ensure the integrity of all readout paths (ROB test). This test was Arduino microprocessor-based and was designed to measure the continuity of the internal strips and the external connectors, it also identifies any

short circuits between neighboring strips. [49]

During the internship (2022), a new testing system, devised by Felipe Ramírez[a], was in the process of implementation. This system was built on an ESP32 microcontroller. In this scenario, I made a valuable contribution by developing a graphical interface aimed at improving the visualization of the ROB test results. Two iterations of the interface were created: one for web use and another for desktop applications. I specifically took charge of the desktop version, and the outcome is showcased below.

Figure 4.6 shows the implemented interface that allows for loading test files and visualizing the board and connectors. The faulty areas and channels are marked in red. Additionally, the interface provides the functionality to extract the information in PDF format (see Figure 4.7). Although this implementation is currently undergoing evaluation and review, the source codes can be accessed in the GitLab repository gitlab.com/cms43/gem21_monitoring.

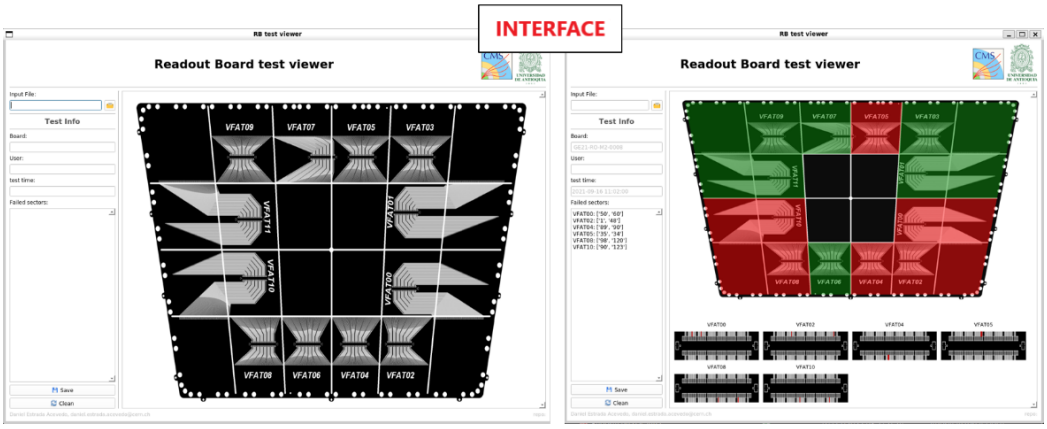

Figure 4.6: Screenshot of the implemented version of the interface to visualize affected sectors from the GE2/1 readout board electrical test results (ROB test).

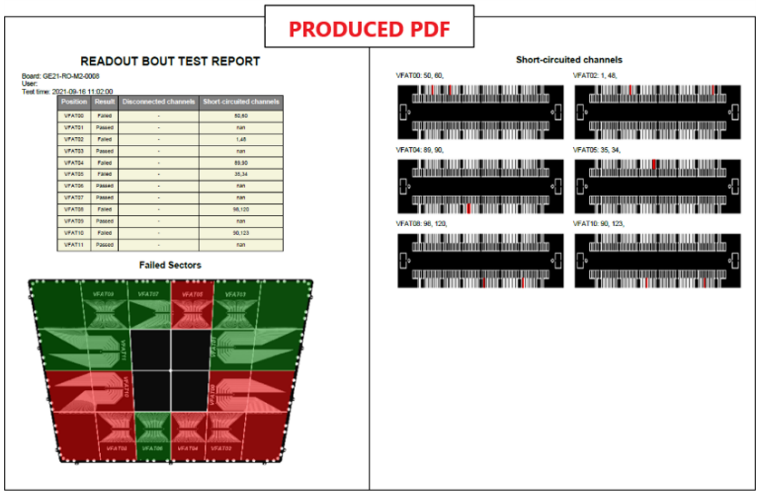

Figure 4.7: Screenshot of pdf summary report produced with the desktop interface.

[a]luis.felipe.ramirez.garcia@cern.ch

4.2.2 QC2

The QC2 step is a more delicate process performed on GEM foils directly and carried out in the cleanroom environment. This test aims to validate the quality of the detector foils by measuring the current leakage across the two sides of them. It can be divided into two steps: [49]

Resistance check and electrical cleaning of the GEM foils

Because of its microscopic nature, the qualification of the GEM foils is not done optically, but electrically by measuring the impedance when 550V is applied (using a handheld Giga-Ohm insulation meter - Megger MIT485 as shown in Figure 4.8 left) between two electrodes of the GEM foil. Low measured values appear when resistance bridges are generated by the presence of dust, chemical contaminants, or mechanical defects, see Figure 4.8 right. For healthy foils, the measurement should be greater than 20 GΩ[b], and, in case a short-circuit between the GEM electrodes takes place, the measured resistance of the foil should be equal to 10 MΩ[c] (or lower in case of multiple short circuits). The test is passed if the foil impedance is above 10 GΩ and the spark rate is lower than 2 Hz after ten minutes.[49]

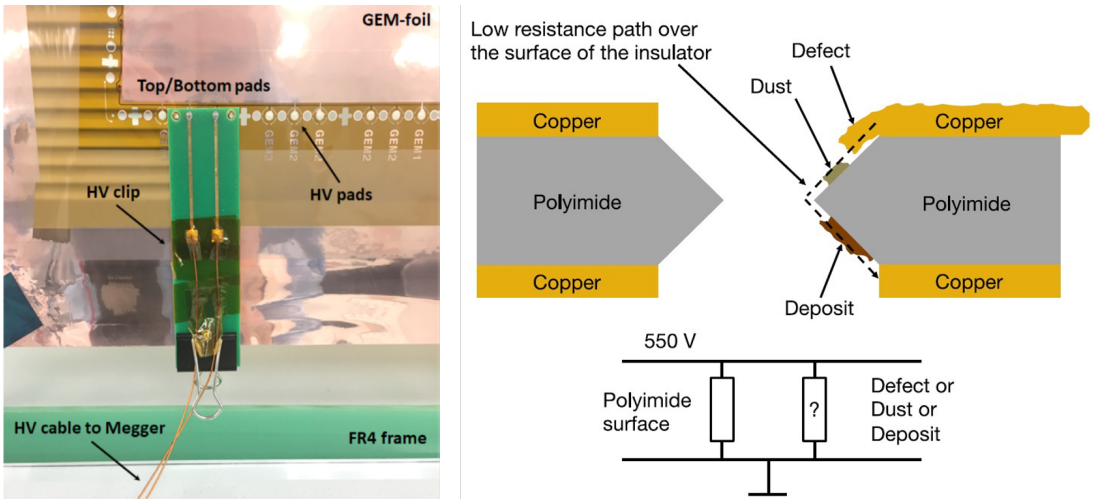

Figure 4.8: Left: Typical setup for the electrical resistance test of GEM foil. Right: Schematic representation of the cross-section of a GEM foil hole with defects in the copper, deposits, and dust that can affect the resistance of the GEM foil, taken from [49].

A general cleaning of the bigger dots is done by using an antistatic adhesive roller. Additionally, a deep cleaning process is done when the current injected into the foils (which flows primarily through contaminated areas with low impedance), cause the evaporation or burning of the impurities or any dust particles within the GEM foil holes. [30, 50]

[b]That is in environments with relative humidity below 50%.

[c]Corresponding to the value of the protection resistors that are soldered directly onto the GEM foils.

Long-term monitoring of the GEM foil leakage current

Aiming to detect and monitor hidden defects that can affect the long-term stability of the chamber and that could not be removed in the previous procedure. The leakage current and discharge rate of all the GEM foils are monitored for several hours during the application of 600 V in a plexiglass box filled with pure nitrogen at a rate of 30-40 L/h, with relative gas humidity below 10%. Those defects could cause GEM foils to experience discharges at high frequency causing serious and permanent damage to the foils. An example of an accepted and rejected foil in this test is shown in Figure 4.9. [49]

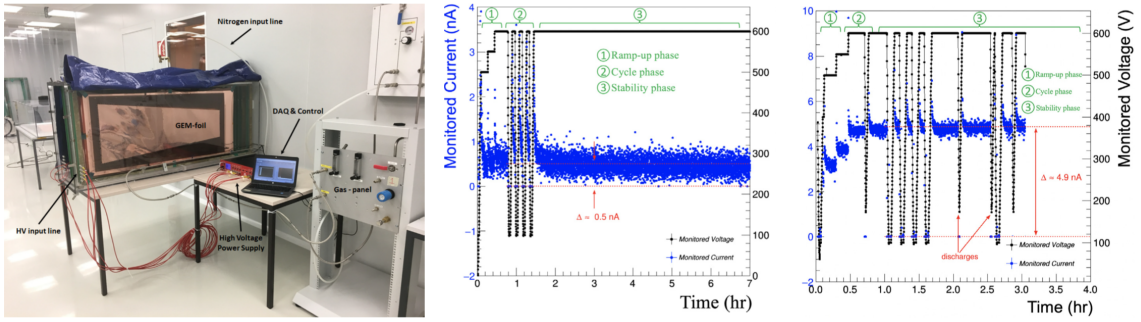

Figure 4.9: From left to right: Picture of test setup for the long-term measurement of leakage currents in GEM foils, and plot of typical leakage current behavior in a validated and rejected GEM foil. Taken from [49].

4.2.3 QC3

This test aims to ensure the gas tightness of the detectors, a critical aspect in maintaining their performance. Ensuring a sealed environment is crucial because potential leaks could permit the entry of undesired gas molecules from the air, potentially compromising the charge amplification and electron transfer processes. Moreover, leaks might introduce dust particles into the gas volume, posing a threat to the integrity of the foil. These issues must be prevented as they could significantly impact HV stability and the chamber's long-term behavior [30]. During my internship, I actively participated in this stage of the process, witnessing firsthand the importance of QC1 and a meticulous assembly process, as numerous cases of gas leaks were identified.

This test assumes a detector with constant volume, so, it is possible to model the evolution of the module's internal pressure by a simple exponential [30]:

$$P_{int} = P_0 e^{-t/\tau}, \tag{4.1}$$

where P_0 is the initial overpressure (which is set in 25 mbar) and τ, is the time constant of the system that depends on the leak point dimensions.

The maximum acceptable leak rate for a single detector must be 1% of the total incoming gas flow rate. So, it is possible to compute from expression 4.1 that to

ensure a 1% or a below leak rate, the time constant should be greater than 3.04 h. In terms of inner pressure, that means a drop of less than 7 mbar/h . Figure 4.10 shows a picture of the QC3 setup, a schematic representation of it, and an example of the pressure line resulting from testing a module. [30, 49]

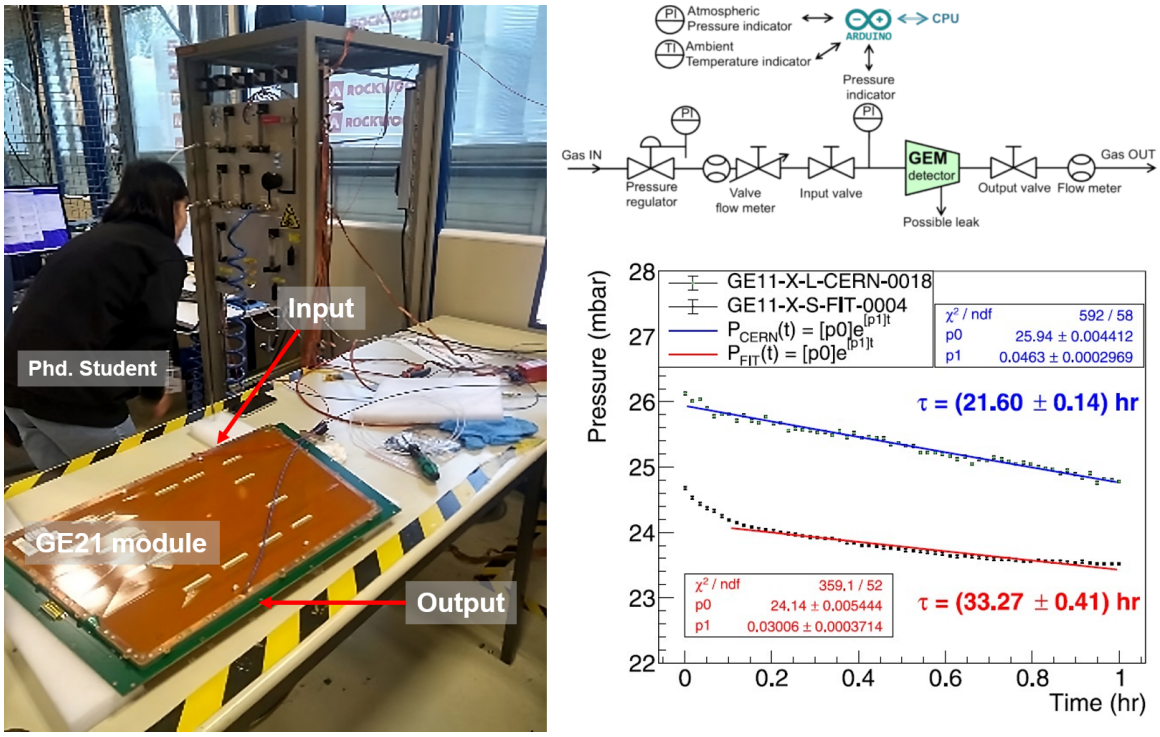

Figure 4.10: Left: A picture of the QC3 setup. Right: A schematic representation of the test stand, and an example of the pressure line resulting from testing a module, taken from [49].

4.2.4 QC4

The objective of this test is to check the on-detector circuitry by analyzing its I-V properties under high voltage in CO_2 with 5 L/h flow rate. For this test, a ceramic divisor resistor is used to distribute the applied voltage in every foil. The idea is to record the current through the powering circuit (R_m) in 100 V step up to reach 5 kV, to compute the circuit resistance and compare it with the nominal or expected value using a simple relative difference (4.2). [30, 49]

Considering that the ceramic resistor has an equivalent resistance of 4.7 MΩ, and that the low-pass protection RC filter and the hardware connection contribute with an extra 0.3 MΩ ($R_n = 5$ MΩ). The criteria for rejecting a module is to have a relative deviation D_R greater than 3%. Figure 4.11 shows how the typical outputs of this test look like. [49]

$$D_R = \frac{|R_m - R_n|}{R_n} \tag{4.2}$$

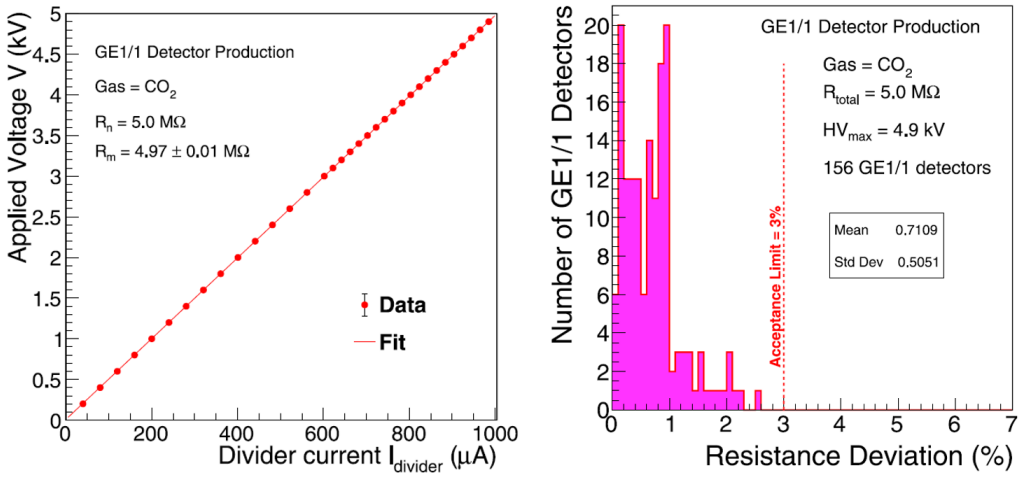

Figure 4.11: Left: High voltage vs. divider current curve for a GE1/1 detector (GE1/1-X-S-CERN-0012), measured in pure CO2. Right: Deviation of the measured resistance, D_R, for the high voltage powering circuit connected to the detector, with respect to its nominal value for all 156 GE1/1 detectors. Taken from [49].

4.2.5 QC5

This QC step is divided into two sub-tests, the effective gas gain, and the response uniformity measurements. Figure 4.12 shows an illustration of the X-ray station and two test result examples.

Effective gas gain

This first part is measured as a function of the current through the HV divider in one central readout sector. In this process, an X-ray generator is used to irradiate the drift board and produce, through fluorescence effects, 8 keV photons which become the primary electrons inside the detector volume. [49]

The effective gas gain is determined experimentally by comparing the primary current induced in the drift gap with the output current provided by the amplification structure of the detector, i.e.: [49]

$$G = \frac{I_{RO}}{R \cdot e \cdot N_p}, \tag{4.3}$$

where, R is the rate of electrons converted from the photoelectric effect from the incident photons, e is the elementary charge, N_p is the number of primary electrons produced by the incident photo-electron in the Ar-CO_2:70-30% gas mixture[d]. [49]

[d] N_p induced by an 8 keV X-ray photon in Ar-CO_2:70-30% gas mixture in the GE1/1 detector was estimated to be 346 ± 3.

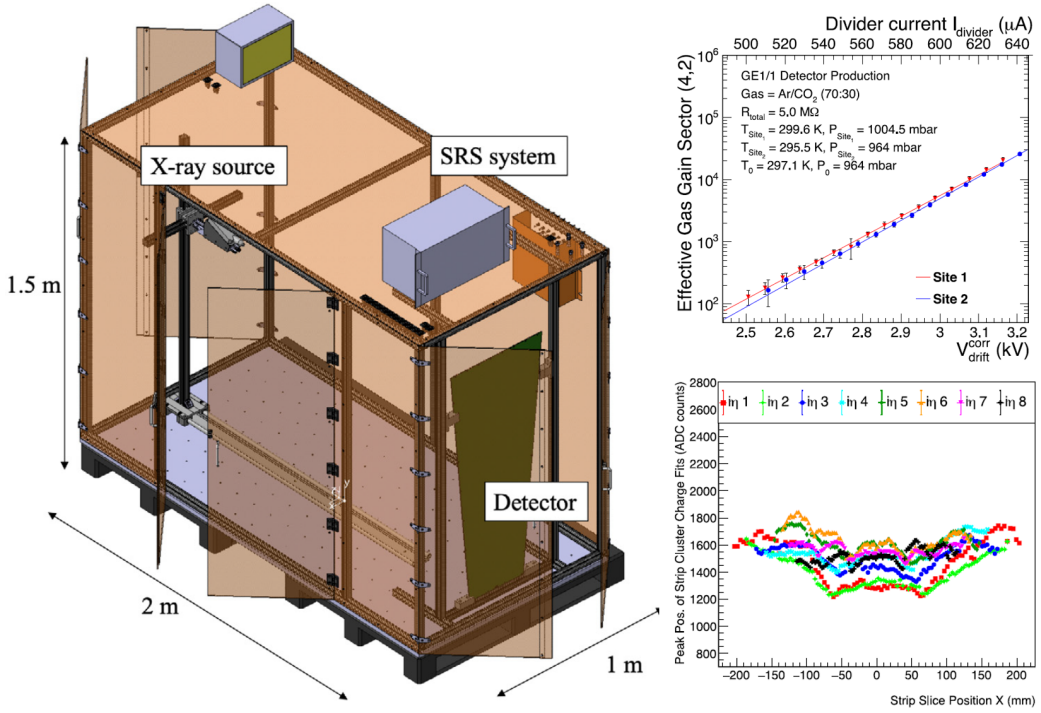

Figure 4.12: Right: Schematic overview of the X-ray station for QC5 tests. Left: (Upper) plot of the effective gas gain of two GE1/1 detectors built and tested at CERN (GE1/1-X-S-CERN-0012, red curve) and in Italy (GE1/1-X-S-BARI-0011, blue curve), (Lower) Plot of Response uniformity of all detectors built during 2017. Taken from [30, 49].

This part of QC does not have a rejection criterion since it is aimed to characterize the gain of each detector, and to use this information in HV line during CMS operation. [30]

Response uniformity measurement

The previous step sets the absolute gain scale of the detector as a function of HV. But it is also important to find the gain across the entire detector (setting the optimal HV working point) and to quantify its variation, so, the relative response is also measured for all readout strips. [49]

The uniformity of the amplification factor is mostly driven by the consistency of the GEM hole geometry across the foil, which is affected by parameters such as the thickness of the polyimide layer and the inner and outer diameters of the biconical holes. So, having into account the uncertainty provided by the foil manufacturers, the criteria to pass this test is to obtain a response uniformity within 15%. [30, 49]

4.2.6 QC6

This stage aims to ensure GEM foil's working stability by putting them under high-voltage conditions. This is done through the same standard Amphenol-connector

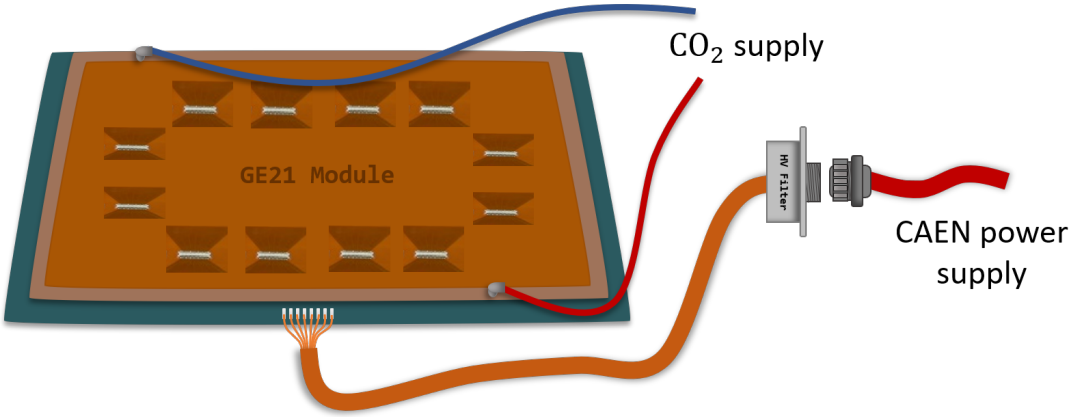

Figure 4.13: Illustration of How GEM detectors are connected to be tested in QC6.

cables installed at CMS, and HV filters to connect the modules to a CAEN power supply board (model A1515). The whole procedure is performed by flushing the chambers with pure CO_2 (see Figure 4.13). The complete test is divided into the following four sub-tests.

Megger test

In order to clean and prepare the foils for the following steps and tests (QC7-8), 550 V is applied on each board path and the impedance is monitored. All through the same type of insulation Tester Megger used on QC2, which is connected with the help of a HV test box in the place of the CAEN power supply wire (see Figure 4.14). The measured values should be in the order of 10 GΩ in the case of a GEX[e] top-bottom measure and 100 GΩ in the case of a gap[f]. At least two hours before this test, the module must be put under CO_2 flush at 5 L/hour.

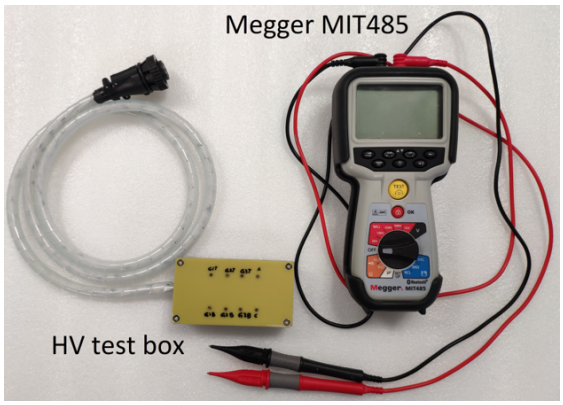

Figure 4.14: HV box and Megger MIT485 for the Megger test.

Stress test

The goal of this test step, as the name suggests, is to take the foil until high voltages searching for the maximum that can be sustained before suffering a trip. The procedure is completely automatized with a Labview interface designed by Felipe Ramirez[g]

[e] X = 1, 2 or 3. Which represents the impedance measured between the pads of, for example, GE1 top and GE1 bottom.

[f] Drift, transfer, or multiplication gap

[g] luis.felipe.ramirez.garcia@cern.ch

during its Doctoral internship. It follows a series of steps that consist of writing commands to the CAEN board to set different test parameters and read monitoring values. Figure 4.15 shows a simplified flow diagramc of the test procedure, and Figure 4.16 shows a snapshot of the mentioned graphical interface (left) with one example of the final plot result from the test (right).

The criteria to pass this sub-test is that the maximum voltage reached for all the foils is greater than 500 V. And that the behavior of this voltage does not show a descending trend along the iteration, because it could mean that there would be growing damage in the foil.

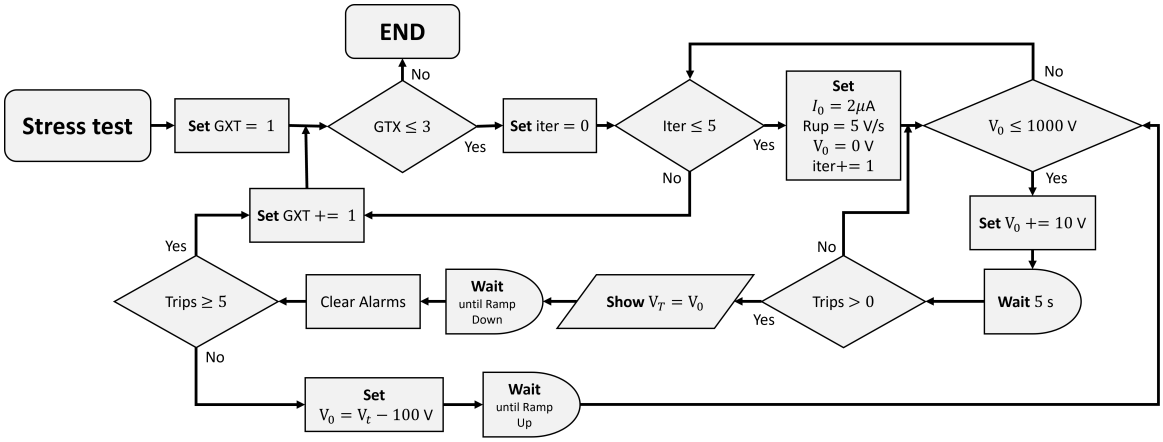

Figure 4.15: Simplified flow diagram of the stress test procedure.

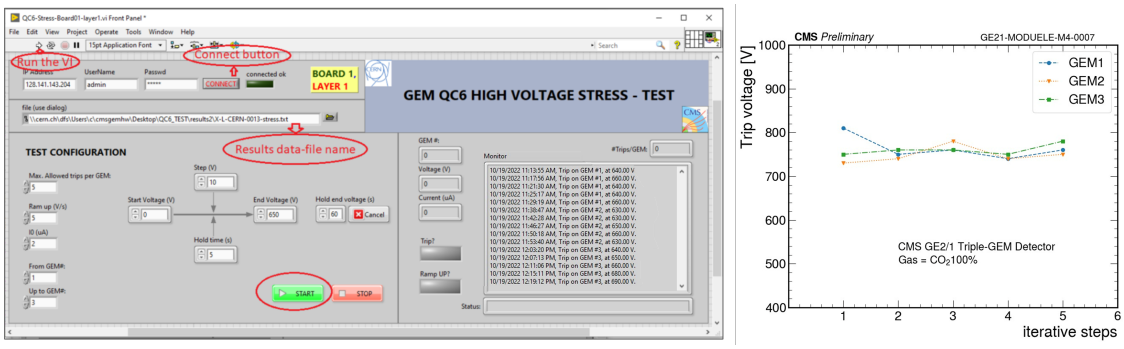

Figure 4.16: Left: a snapshot of the LabView instrument designed to automatize the stress test. Right: An example of a result gotten from this test.

Short stability test - I vs V scan

This test aims to determine the characteristic I vs V curve of each GEM foil and regions of GEM detectors. The scan sweeps the total voltage (sum of foils and gaps voltages) from 200 V to 4600 V, meanwhile, the (Vmon, Imon) pair is monitored and registered. The last voltage is held at least for two hours to check if trips occur.

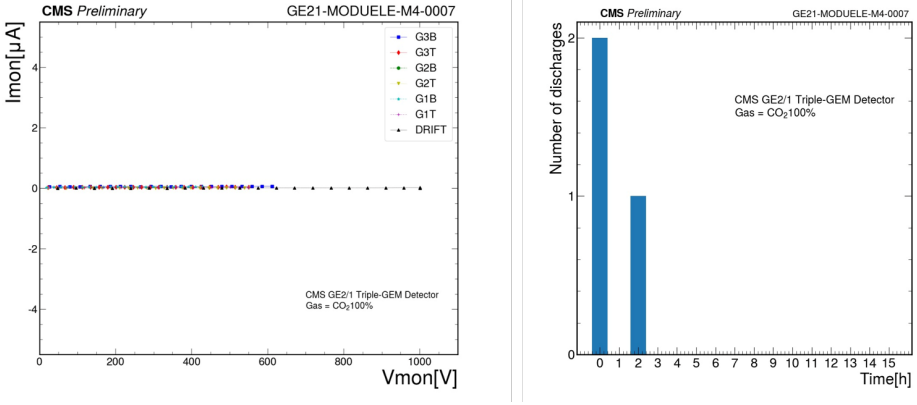

Figure 4.17: Example plots for results of the short (left) and long (right) stability tests.

Such as in the previous test step, the process is automatized with another LabView interface, which follows a similar logic of writing and reading parameters into the CAEN power supply machine. Figure 4.17 shows an example of the resulting plot, the I vs V relation.

The test is passed if all the I vs V plots are linear and the maximum current is lower than 1 μA.

Long stability test

The goal of the Long stability test is to keep all the GEM foils ON at 580 V for at least 15 hours and monitor their stable operation. Another LabView instrument takes care of the operation and register of the number of trips of the power supply. The test is considered passed if the number of trips per hour reduces to 0 ± 1. If after 15 hours there are still trips, the test needs to be extended until this number is reduced. Figure 4.17 (right) shows a timeline register of those trips.

Contribution to process optimization

As can be noticed from the previous description, the QC6 test is a series of steps that could take at least 20 hours per module. That implies a bottleneck in the intended massive production chain. QC6 test stands for the GE1/1 production was prepared in a four-test place arrangement, with the idea of testing four detectors at a time using one dedicated computer for each of them (see Figure 4.18). In the case of GE2/1 and ME0 massive production, that could cause an undesired delay in terms of the QC spent time by a detector, due to their modular composition.

Aiming to contribute to problem mitigation, a new design of the QC6 test stand was prepared during my stay at CERN. Throughout those months, a significant portion of my time was devoted to adapting the QC6 stand to operate more efficiently. Figure 4.19 illustrates a new configuration of the QC6 stand, featuring a layout of six

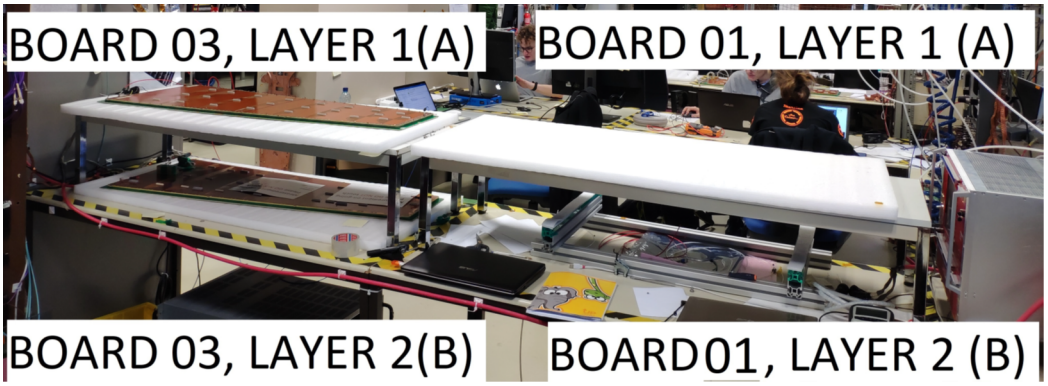

Figure 4.18: QC6 stand picture showing the board and the layer structure used in GE1/1 massive production.

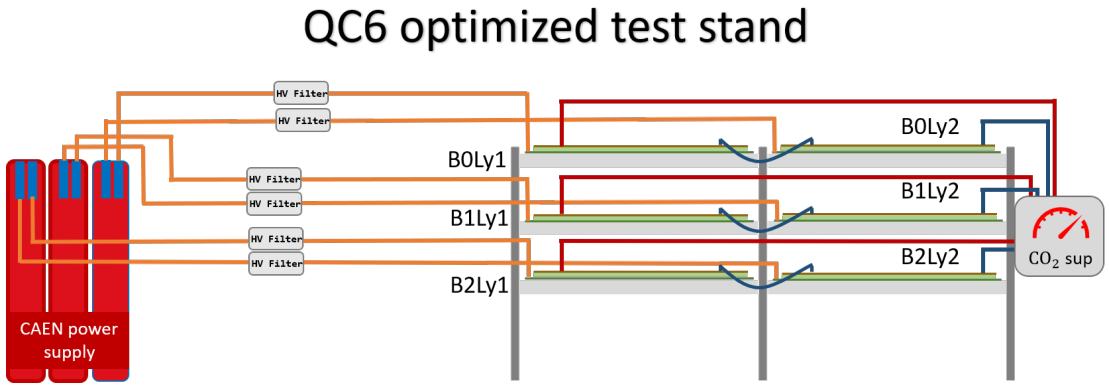

Figure 4.19: Optimized QC6 test stand illustrations.

modules. This design is intended for implementation during massive production.

The improvement, besides an adaptation of the CAEN instrument with new boards, involved upgrading the existing software to accommodate the new multi-module requirement. The goal was to have the new stand to operate with a single dedicated computer capable of executing multiple instances of the modified LabView instruments. This setup enables the control and monitoring of the power supply for each BOARD-LAYER table. See Figure 4.20.

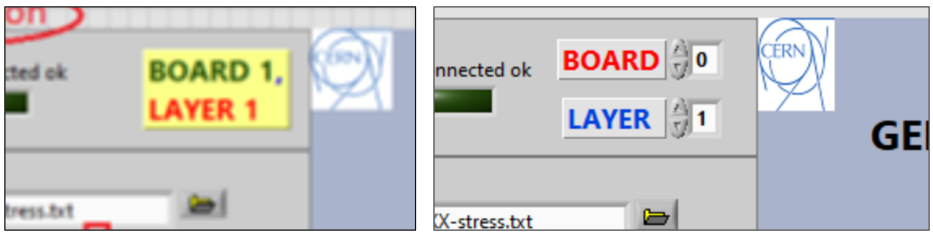

Figure 4.20: Screenshots comparing the old and the upgraded versions of LabView instruments for QC6.

The integration of the software instrument required a significant effort to understand the development steps carried out by Felipe's designs. However, the problem was ultimately resolved in a straightforward manner by defining global variables that indicated the desired BOARD and LAYER for manipulation. With these variables, the code (not the algorithm) was adapted so that each routine would send the appropriate command to the CAEN instrument based on the selected indices. This functionality can be observed in the snapshots displayed on the right side of Figure 4.20, where two "spin boxes" were added to select the corresponding BOARD and LAYER numbers.

Additionally, to prevent potentially unsafe user manipulations and to facilitate interaction, making the system more user-friendly, unique executable instances of each software instrument were made accessible on the dedicated computer's desktop. This is illustrated in Figure 4.21. Furthermore, if needed, all the source codes have been saved in the GitLab project gitlab.cern.ch/cms-gem-qc6.

Figure 4.21: Illustration of the QC6 test software facilities available in the test computer.

It is anticipated that this new design of the QC6 facilities will have a significant impact in a massive production environment. At the time of writing this manuscript, there is no available data on the evaluation or performance of the test stage. However, it is plausible to say that the process has been optimized by approximately 80%.

4.2.7 QC7

In this production step, off-detector electronics integration takes place and a series of connectivity - power, and noise - signal output tests are performed. This test is the first opportunity to have all the electronics connected to the detector. The connectivity and power test helps to ensure that all readout chips, voltage, and signal converters are connected and communicating well. The other one sets up the working point and identifies dead and noisy channels with the same (but local and in low-

scaled) electronic scans mentioned in chapter 3. With that, damaged components can be properly identified. Once those processes are finished, it is possible to keep going with the GEM detector assembly by adding the cooling board, protection cover, and a front patch panel to establish the gas and electronics connections (see Figure 4.22). The same Figure shows the first GE2/1 chamber (M1-M4) that could be assembled in the last months of 2022 at *Prévessin* site - CERN. [6]

Figure 4.22: Set of pictures that illustrate main QC7 steps. Taken from [6]

4.2.8 QC8

This corresponds to the last and major QC step before the installation at CMS. Here, the detector performance is tested and its optimal working parameters are set in a dedicated cosmic ray stand (see Figure 4.23). The test comprises some optimal parameter determination processes to characterize every chamber and others to evaluate quantities such as, for example, the detection efficiency which is required to be at least 97%. [14, 30].

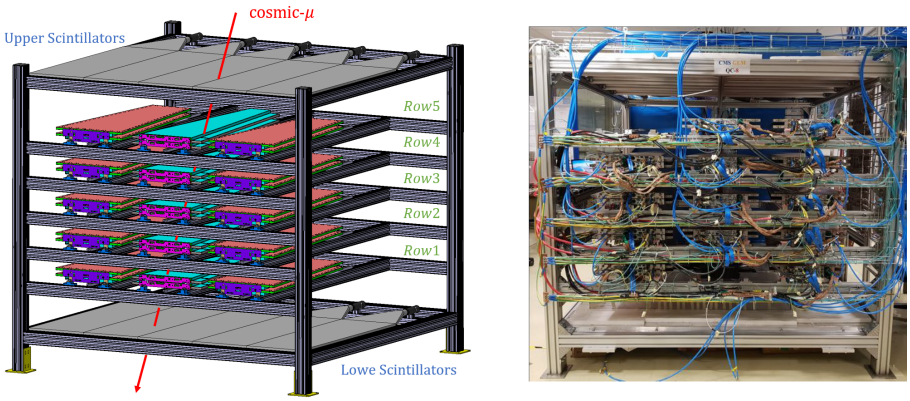

Figure 4.23: General view of the cosmic ray stand for QC8. Taken from [14].

The mentioned cosmic rays stand is a cubic aluminum structure ($200 \times 200 \times 200$ cm^3) designed to maximize the solid acceptance angle for the cosmic muons. The stand is able to sandwich five layers of GEM detectors between two sets of plastic scintillators which play the role of trigger and detection reference system. For GE1/1 superchambers geometries, it was possible to host fifteen of them into the stand, and in the case of GE2/1 superchambers two extra layers will be added to be able to host seven of them. The cosmic stand's service was designed as similar as possible to the ones installed on the CMS experiment. It uses CAEN instruments for HV and LV supply, and individual gas and cooling lines to inject chambers with Ar-CO_2:70-30% at 3 nL/h and cooling them with water at 16° under pressure below than atmosphere. Analogous to CMS operations, the power supply system is controlled and monitored through a scaled unified Detector Control System (DCS). [14]

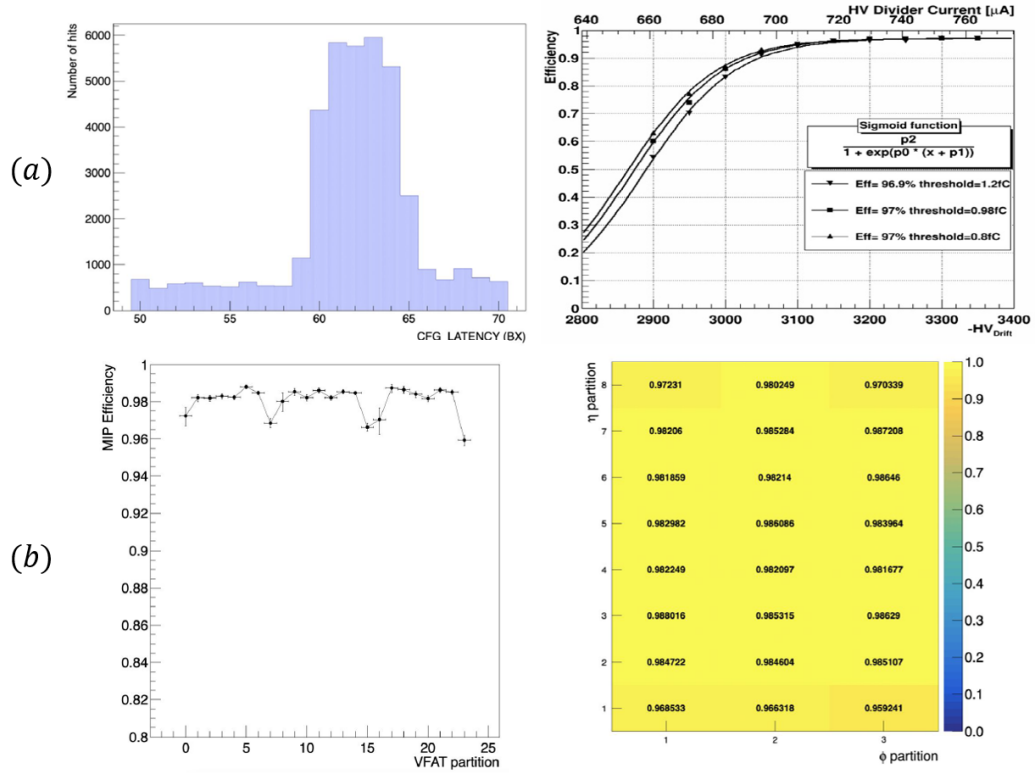

Figure 4.24: Some examples of most important plots resulting from QC8 data analysis. (a) A typical latency scan and average efficiency vs equivalent HV divider current plots. Taken from [14, 6].

Some of the important results that can be gotten from this test are: In the case of detector characterization (see Figure 4.24.a), determination of optimal latency parameter by measuring the response time of the GEM detectors with respect to the trigger signals (scintillators detections). Establishing of the optimal HV working point to get desired detector efficiencies (efficiency vs HV curves); in the case of performance evaluation (see Figure 4.24.b), identification of the noisy and dead strips of the detectors. And computation of muon detection efficiency by different data taken analysis such as track-based analysis or Fast efficiency calculations [14].

4.3 Installation phase

In the production workflow, QC8 marks the completion of the detector's quality control stage. The next step involves conducting final checks and properly storing each detector until it is installed in CMS detector. This stage should not be underestimated, since ensuring the integrity of the GEM foils is a challenging task. Therefore, the GEM chambers are kept flushed with an inner gas to prevent any potential deposition of contaminants on the foils prior to the installation phase.

The installation procedure also entails significant logistical coordination, as the CMS detector schedule strictly defines the interventions of various detector teams. For instance, as was mentioned in chapter 1, GE1/1 station installation required a period of more than one year to be completed. The first endcap of GEM detectors (negative GE1/1 endcap) was successfully completed in October 2019, but it required multiple installation windows between July and October of that year. Similarly occurred for the installation of the second endcap (positive endcap) which was completed in september of 2020[h].

It is evident that the GE2/1 assembly procedures described here pertain to the detectors that will be installed in the upcoming CMS upgrade phase during LS3. The installation is scheduled to take place in 2023 for the first endcap and in 2024 for the second endcap. As for the final GEM stage, ME0, a complete cycle of research, production, and installation is yet to commence. Production for ME0 is planned to begin in 2023 and extend until 2025.

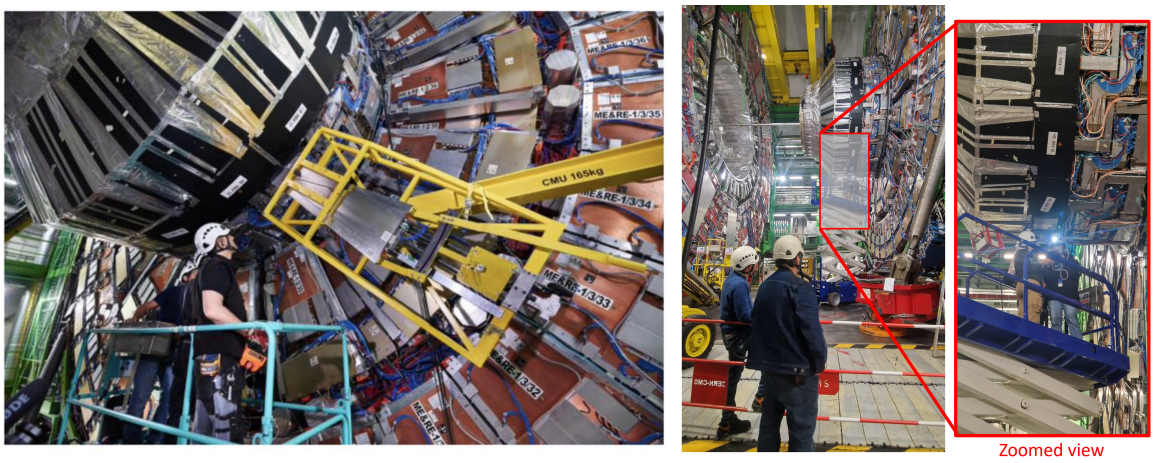

Figure 4.25: Pictures taken by the GEM group during: (Left) the GE1/1 installation, taken from [14]. (Right) Any pre-installation operation for GE2/1 in mid-November (2023), shared between GEM team members.

[h]Also consider that this process was delayed because of the COVID-19 lockdown.

Chapter 5

Conclusions

Along this work, it was possible to establish conceptual bases that highlight the good qualities of the GEM technology as gaseous detectors and how that is being incorporated into the CMS experiment in the CERN-LHC. In that context, most of the relevant details about infrastructure, logistics, operations, and even my personal contributions to the GEM group were presented. The latter meeting the GEM research group's needs.

This research work specifically addressed some of those necessities: First of all, in the frame of the massive production and quality control processes, personpower was required, so my presence in the GEM laboratories contributed to maintaining the detectors' production on schedule. Even more, I could help with the improvement of the performance of the sixth step quality control process, where the test of each detector used to take around 20 hours at least, meaning a bottleneck in the detectors' chain manufacturing. Helping with the implementation of a new parallelized approach, the total process could be speeded up to 6 times. In the sense of the quality control process, I also could make a contribution by implementing a desktop graphical user interface (GUI) to easily visualize the resulting data of one of the tests performed to ensure the good quality of the GEM readout boards.

Additionally, as the GEM group is currently undergoing a redesign of the DAQ software by migrating several of the DAQ data analysis routines to a Python environment, I took part in the DAQ team by implementing two important codes that are being used by the group in its routinary operations. The first implementation that I developed was the threshold scan analysis routine, a script designed to take threshold scan files and then identify problematic channels around the entire detector. The algorithm simply classifies channels as turned off, fully working, or broken. The second contribution consisted of the implementation of the s-curve scan analysis routine, a script designed to take the s-curve scan files and extract some important information used to characterize principally the expected noisy (ENC) levels for each channel and VFAT.

With this manuscript, more than to emphasize my particular work in the GEM group, I am leaving a text as self-contained as I could, which, I wish, serves as an

invaluable reference for students interested in joining the GEM project. I consider that a significant understanding of the physics behind particle detection processes has been exposed opening up doors to this field of interest.

Bibliography

[1] David Griffiths. *Introduction to elementary particles*. Ed. by Inc. John Wiley & Sons. Federal Republic of Germany, 1987. ISBN: 978-0-471-60386-3.

[2] James S. Trefil. *From atoms to quarks : an introduction to the strange world of particle physics*. New York : Scribner, 1980.

[3] Frank. E Close. *The cosmic onion : quarks and the nature of the universe*. New York, NY : American Institute of Physics, 1986. ISBN: 0883184915.

[4] Jose David Ruiz Alvarez. "Search for a vector-like quark T' decaying into top+Higgs in single production mode in full hadronic final state using CMS data collected at 8 TeV". PhD thesis. l'Université Claude Bernard – Lyon 1 École Doctorale de Physique et d'Astrophysique, Oct. 2015. URL: https://cds.cern.ch/record/2158856.

[5] Wikimedia Commons contributors. *File:Standard Model of Elementary Particles.svg - Wikimedia Commons*. URL: https://commons.wikimedia.org/wiki/File:Standard_Model_of_Elementary_Particles.svg.

[6] Jeremie Alexander Merlin. "Introduction to the GEM technology". In: *GEM 101 lectures*. Nov. 2022. URL: https://indico.cern.ch/event/1220990/contributions/5136456/attachments/2554368/4401371/JMERLIN_GEM_Technology_2022.pdf.

[7] Pedro Ladrón de Guevara. *Principios de los detectores de partículas Talk I*. Feb. 2013. URL: https://teorica.fis.ucm.es/ft11/PARTICULAS.DIR/Detectores_1.pdf.

[8] CERN. *LHC experiments join forces to zoom in on the Higgs boson*. Mar. 2015. URL: https://home.cern/news/news/accelerators/lhc-experiments-join-forces-zoom-higgs-boson.

[9] CERN. *Cosmic rays: particles from outer space*. URL: https://home.cern/science/physics/cosmic-rays-particles-outer-space.

[10] Wikipedia. *Cosmotron*. URL: https://en.wikipedia.org/wiki/Cosmotron.

[11] Wikipedia. *CERN*. URL: https://en.wikipedia.org/wiki/CERN.

[12] Wikipedia. *SLAC National Accelerator Laboratory*. URL: https://en.wikipedia.org/wiki/SLAC_National_Accelerator_Laboratory.

[13] C. O. Dib. "Experimental facilities in Latin America". In: *CERN Yellow Rep. School Proc.* 2.2021 (May 2021), pp. 193–219. ISSN: 2519805X. DOI: 10.23730/CYRSP-2021-002.193.

[14] Giovani Mocellin. "Performance of the GE1/1 detectors for the upgrade of the CMS Muon Forward system". PhD thesis. Rheinish-Westfälische Technische Hochschule Aachen University, 2021. URL: https://cds.cern.ch/record/2809098.

[15] Fiorina Davide. "Advanced aging study on Triple GEMs for CMS GE2/1 and ME0". PhD thesis. Università degli Studi di Pavia, Nov. 2018. URL: http://cds.cern.ch/record/2717264.

[16] Xabier Cid Vidal and Ramon Cid Manzano. *Taking a closer look at LHC*. URL: https://lhc-closer.es.

[17] *Home — HL-LHC Industry*. URL: https://project-hl-lhc-industry.web.cern.ch/.

[18] Anonymous. *The High-Luminosity LHC Project. 298th Meeting of Scientific Policy Committee*. Tech. rep. June 2016. URL: https://cds.cern.ch/record/2199189.

[19] *LHC long term schedule*. URL: http://lhc-commissioning.web.cern.ch/schedule/LHC-long-term.htm.

[20] Wikipedia. *Large Hadron Collider*. URL: https://en.wikipedia.org/wiki/Large_Hadron_Collider.

[21] CERN. *First Run 3 physics result by CMS — CERN*. Nov. 2022. URL: https://home.cern/news/news/physics/first-run-3-physics-result-cms.

[22] CMS Collaboration. "The CMS experiment at the CERN LHC". In: *Journal of Instrumentation* 3.08 (Aug. 2008), S08004. ISSN: 1748-0221. DOI: 10.1088/1748-0221/3/08/S08004. URL: https://iopscience.iop.org/article/10.1088/1748-0221/3/08/S08004%20https://iopscience.iop.org/article/10.1088/1748-0221/3/08/S08004/meta.

[23] CMS Collaboration. "Technical Proposal for the Phase-II Upgrade of the CMS Detector". In: *2015* June (June 2015). DOI: 10.17181/CERN.VU8I.D59J. URL: https://cds.cern.ch/record/2020886.

[24] S. Chatrchyan et al. "The performance of the CMS muon detector in proton-proton collisions at \sqrt{s} = 7 TeV at the LHC". In: *Journal of Instrumentation* 8.11 (Nov. 2013), P11002. ISSN: 17480221. DOI: 10.1088/1748-0221/8/11/P11002. URL: https://cds.cern.ch/record/1558674.

[25] CMS Experiment. *Detector*. URL: https://cms.cern/detector.

[26] Konstantinos Damanakis. "Silicon sensors for the Phase-2 upgrade of the CMS Outer Tracker; status and early results from the production phase". In: *Nuclear Instruments and Methods in Physics Research Section A: Accelerators, Spectrometers, Detectors and Associated Equipment* 1040 (Oct. 2022), p. 167034. ISSN: 0168-9002. DOI: 10.1016/J.NIMA.2022.167034.

[27] David Barney. *Presentation for public - Introduction to CMS for CERN guides*. June 2013. URL: https://cds.cern.ch/record/2629323.

[28] CMS Collaboration. *The Phase-2 Upgrade of the CMS Muon Detectors*. Tech. rep. Sept. 2017. URL: https://cds.cern.ch/record/2283189.

[29] Sylvie Braibant, Giorgio Giacomelli, and Maurizio Spurio. "Particles and Fundamental Interactions". In: Undergraduate Lecture Notes in Physics (2012). DOI: 10.1007/978-94-007-2464-8. URL: http://link.springer.com/10.1007/978-94-007-2464-8.

[30] D. Abbaneo et al. "Operational Experience with the GEM Detector Assembly Lines for the CMS Forward Muon Upgrade". In: *IEEE Transactions on Nuclear Science* 65.11 (Nov. 2018), pp. 2808–2816. ISSN: 00189499. DOI: 10.1109/TNS.2018.2871428.

[31] Fabio Sauli. "Principles of operation of multiwire proportional and drift chambers". In: (1977). DOI: 10.5170/CERN-1977-009. URL: https://cds.cern.ch/record/117989.

[32] nuclear-power.com. *Ionization Chamber vs Proportional Counter*. URL: https://www.nuclear-power.com/nuclear-engineering/radiation-detection/gaseous-ionization-detector/ionization-chamber-vs-proportional-counter/.

[33] Fabio Sauli. "Gaseous radiation detectors: Fundamentals and applications". In: *Gaseous Radiation Detectors: Fundamentals and Applications* 9781107043015 (Jan. 2011), pp. 1–497. DOI: 10.1017/CBO9781107337701.

[34] INFN. *Welcome on triple GEM detectors R&D : IMAGEM and GEMINI*. URL: https://web.infn.it/GEMINI/.

[35] Fabio Sauli. "Micro-pattern gaseous detectors principles of operation and applications". In: *Micro-pattern Gaseous Detectors: Principles Of Operation And Applications* (Jan. 2020), pp. 1–349. DOI: 10.1142/11882.

[36] G. Corradi, F. Murtas, and D. Tagnani. "A novel High-Voltage System for a triple GEM detector". In: *Nuclear Instruments and Methods in Physics Research Section A: Accelerators, Spectrometers, Detectors and Associated Equipment* 572.1 (Mar. 2007), pp. 96–97. ISSN: 0168-9002. DOI: 10.1016/J.NIMA.2006.10.166.

[37] S. Bachmann et al. "Discharge studies and prevention in the gas electron multiplier (GEM)". In: *Nuclear Instruments and Methods in Physics Research Section A: Accelerators, Spectrometers, Detectors and Associated Equipment* 479.2-3 (Mar. 2002), pp. 294–308. ISSN: 0168-9002. DOI: 10.1016/S0168-9002(01)00931-7.

[38] DONALD E GROOM, NIKOLAI V MOKHOV, and SERGEI I STRIGANOV. "MUON STOPPING POWER AND RANGE TABLES 10 MeV–100 TeV". In: *Atomic Data and Nuclear Data Tables* 78.2 (2001), pp. 183–356. ISSN: 0092-640X. DOI: https://doi.org/10.1006/adnd.2001.0861. URL: https://www.sciencedirect.com/science/article/pii/S0092640X01908617.

[39] J Werss and W Bernstein. "Energy RecIuired to Produce One Ion Pair for Several Gases*". In: (1955).

[40] Aamir IRSHAD. "The CMS GEM Detector Front-end Electronics Characterization and Implementation". PhD thesis. Universite Libre de Bruxelles, Dec. 2021. URL: https://cds.cern.ch/record/2798969.

[41] Thomas Lenzi. "Development of the DAQ System of Triple-GEM Detectors for the CMS Muon Spectrometer Upgrade at LHC". PhD thesis. Université Libre de Bruxelles, Dec. 2016, pp. 41–123. URL: https://cds.cern.ch/record/2239914?ln=es.

[42] Kevin Black. "GEM Electronics Overview". In: *GEM 101 lectures*. Geneva, 2022. URL: https://indico.cern.ch/event/1220990/contributions/5136457/attachments/2555536/4403586/ElectronicsOverview.pptx.

[43] Jason Rosa. "Characterizing the VFAT3 chip for the DAQ electronics of the CMS detector". PhD thesis. Université Libre de Bruxelles, 2017. URL: https://cds.cern.ch/record/2290728.

[44] P. Aspell et al. "VFAT3: A Trigger and Tracking Front-end ASIC for the Binary Readout of Gaseous and Silicon Sensors". In: *2018 IEEE Nuclear Science Symposium and Medical Imaging Conference, NSS/MIC 2018 - Proceedings* (Nov. 2018). DOI: 10.1109/NSSMIC.2018.8824655.

[45] P. Aspell et al. "VFAT2 :A front-end "system on chip" providing fast trigger information and digitized data storage for the charge sensitive readout of multichannel silicon and gas particle detectors". In: *IEEE Nuclear Science Symposium Conference Record* (2008), pp. 1489–1494. ISSN: 10957863. DOI: 10.1109/NSSMIC.2008.4774696.

[46] Evaldas Juska. "GEM Backend and Central CMS". In: *GEM 101 Lectures*. Texas A & M University. United State, Nov. 2022. URL: https://indico.cern.ch/event/1220990/contributions/5136468/attachments/2555783/4403985/GEM_101.pdf.

[47] Stephen D. Butalla and Marcus Hohlmann. *Frontend Electronics Integration for the GE2/1 GEM Detector for the Phase-2 Muon System Upgrade of the CMS Experiment*. Tech. rep. Whashington, D. C.: Florida Institute of Technology, Apr. 2020. URL: https://research.fit.edu/media/site-specific/researchfitedu/hep/heplaba/documents/conferences-and-workshops/national-amp-international/APS2020_ButallaHohlmann_FINAL.pdf.

[48] Aashaq Shah and CMS-Muon Collaboration. "Layout and Assembly Technique of the GEM Chambers for the Upgrade of the CMS First Muon Endcap Station". In: *Nucl. Instrum. Meth. A* 918 (Dec. 2018), pp. 67–75. DOI: 10.1016/j.nima.2018.11.061. URL: http://arxiv.org/abs/1812.00411%20http://dx.doi.org/10.1016/j.nima.2018.11.061.

[49] M. Abbas et al. "Quality control of mass-produced GEM detectors for the CMS GE1/1 muon upgrade". In: *Nuclear Instruments and Methods in Physics Research Section A: Accelerators, Spectrometers, Detectors and Associated Equipment* 1034 (July 2022), p. 166716. ISSN: 0168-9002. DOI: 10.1016/J.NIMA.2022.166716.

[50] D. Abbaneo et al. “Layout and assembly technique of the GEM chambers for the upgrade of the CMS first muon endcap station”. In: *Nuclear Instruments and Methods in Physics Research Section A: Accelerators, Spectrometers, Detectors and Associated Equipment* 918 (Feb. 2019), pp. 67–75. ISSN: 0168-9002. DOI: 10.1016/J.NIMA.2018.11.061. URL: https://doi.org/10.1016/j.nima.2018.11.061.